TECHNISCHE UNIVERSITÄT MÜNCHEN
Lehrstuhl für Physik funktionaler Schichtsysteme, E10

Spin Waves in 2D and 3D Magnonic Crystals: From Nanostructured Ferromagnetic Materials to Chiral Helimagnets

Thomas Schwarze

Vollständiger Abdruck der von der Fakultät für Physik der Technischen Universität München zur Erlangung des akademischen Grades eines

Doktors der Naturwissenschaften

genehmigten Dissertation.

Vorsitzender: Univ.-Prof. Dr. Martin Zacharias
Prüfer der Dissertation:
1. Univ.-Prof. Dr. Dirk Grundler
2. Univ.-Prof. Christian Pfleiderer, Ph.D.

Die Dissertation wurde am 26.09.2013 bei der Technischen Universität München eingereicht und durch die Fakultät für Physik am 16.12.2013 angenommen.

go mosadi wame
(to my wife)

Abstract

Spin wave (SW) excitations in two-dimensional (2D) and three-dimensional (3D) periodic nanostructures and chiral helimagnets have been studied experimentally and compared to theoretical predictions. SW spectroscopy has been performed with microstructured coplanar wave guides, to measure SW excitations as well as SW propagation. 2D samples were structured with periodic arrays of holes, so-called antidot lattices (ADLs) with periods ranging from 800 nm down to 240 nm, using focused ion beam lithography. Artificially introduced defects were found to support fast SW propagation with the additional freedom to guide SWs around corners. Complete band gaps were predicted in ADLs with periods below 600 nm. Bio-engineered 3D magnetoferritin crystals have been studied experimentally and SW propagation over a few micrometers was found. In collaboration with a theory group, GHz excitations in these systems were modeled using an effective anisotropy of individual nanoparticles. Different systems of chiral helimagnets, i.e. metallic MnSi, insulating Cu_2OSeO_3, and semiconducting $Fe_{1-x}Co_xSi$, have been studied throughout their magnetic phase diagram. The GHz excitations were found to differ in absolute values between different materials, but when being normalized to their specific T-dependent critical fields and accounting for the geometry of the sample, the data fall onto universal curves being characteristic for the different magnetic phases. We find excellent agreement between experiment and theory developed by a theoretical group.

Es wurden Spinwellen (SW) Anregungen in zweidimensionalen (2D) und dreidimensionalen (3D) periodischen Nanostrukturen und chirale Helimagnete experimentell untersucht und mit theoretischen Vorhersagen verglichen. Spinwellen-Spektroskopie mit mikrostrukturierten koplanaren Wellenleitern wurde durchgeführt, um die Anregung sowie Ausbreitung von Spinwellen zu messen. 2D Proben wurden mit Hilfe von fokussierter Ionenstrahllithographie mit periodischen Löchern, so genannten Antidot-Gittern (ADLs) mit Gitterperioden von 800 nm bis 180 nm, strukturiert. In kün-

stlich erzeugten Defekten wurden aussergewöhnlich schnelle SW gemessen, die dazu noch um Ecken gelenkt werden konnten. Komplette Bandlücken wurden für ADLs mit Gitterperioden unter 600 nm vorausgesagt. Biologisch hergestellte 3D Magnetoferritin Kristalle wurden experimentell untersucht und propagierende SWs über wenige Mikrometer konnten nachgewiesen werden. In Zusammenarbeit mit einer Theoriegruppe konnten die GHz-Anregungen mit Hilfe einer effektiven Anisotropie der einzelnen Nanopartikel erklärt werden. Verschieden Systeme von chiralen Helimagneten, d.h. metallisches MnSi, isolierendes Cu_2OSeO_3 und halbleitendes $Fe_{1-x}Co_xSi$, wurden über ihr magnetisches Phasendiagram untersucht. Die Absolutwerte der GHz-Anregungen unterscheiden sich zwischen den verschiedenen Materialsystemen. Durch Normierung auf die spezifischen temperaturabhängigen kritischen Felder und unter Berücksichtigung der Geometrie der Probe konnten die Anregungen in den verschiedenen Phasen auf eine universelle Theorie zurückgeführt werden. Exzellente Übereinstimmung zwischen den Experimenten und der Theorie, entwickelt von einer Theoriegruppe, wurde gefunden.

Contents

Scientific Collaboration

Parts of this thesis have been conducted as a scientific collaboration. The author would like to state the content of this collaboration:

- Magnetoferritin crystals have been fabricated by Dr. Mitsuhiro Okuda in the group of Prof. Walther Schwarzacher at the University of Bristol, UK. In addition to as-prepared crystals they provided FIB processed samples.

- Perpendicular magnetic anisotropy samples have been provided by Prof. Johan Åkerman at the University of Gothenburg.

- MnSi and $Fe_{0.8}Co_{0.2}Si$ samples have been provided by Prof. Christian Pfleiderer and Andreas Bauer at E21, TUM. Cu_2OSeO_3 samples were prepared by Helmut Berger at École Polytechnique Fédérale de Lausanne, Switzerland.

- The theory on chiral helimagnets has been developed by Prof. Achim Rosch, Dr. Markus Garst, and Johannes Waizner at the University of Cologne. They provided field dispersion plots for different magnetic phases and visualization of such.

- Theoretical interpretation on GHz excitations in magnetoferritin crystals has been obtained by Dr. Maciej Krawczyk at Adam Mickiewicz University in Poznan, Poland.

In addition to providing samples and theoretical interpretation the author is thankful for the fruitful and inspiring discussions accompanied with these collaborations. The author expresses his gratitude to all collaborators and their institutes.

1. Introduction

The research field of magnonics has attracted a lot of interest in recent years promoted by the need for miniaturization and low-power consumption in modern information technology (IT)[ITR09]. Magnonic crystals (MCs), i.e., periodically patterned ferromagnets, are the analogues of photonic, plasmonic, and phononic crystals that are exploited for the manipulation of wave-like excitations [Joa08, Gao10, Yu10]. In the field of magnonics, one explores the creation, manipulation, and detection of spin waves [Blo30], i.e. wave-like spin excitations [Kru06, Neu09b, Kru10, Len11]. In general, spin-wave based MCs can be realized in a smaller size compared to photonic crystals and they hold great promise for downscaling microwave devices operated in the GHz frequency regime [Neu09b, Kru10]. The downscaling argument is similar to surface acoustic wave based GHz filters and delay lines which are an integral part of the telecommunication market [Cam98]. Due to anisotropic dispersion and long range dipolar interaction, the underlaying physics and tunability of magnonic crystals can differ from their optical and acoustic counterparts due to the formation of minibands [Neu10, Neu11d]. The discovery of the spin-transfer torque [Bai88, Tso00, Kis03] has further stimulated the research for nanoscale devices in the microwave regime. It has been demonstrated that a DC current is able to excite magnetization precession in a giant magnetoresistance nanopillar, so-called spin-transfer nano-oscillators (STNOs). The combination of spin waves and STNOs was proposed to create nanoscale microwave devices [Ber96, Dem10]. Here, the research on spin waves is essential to pave way for future integrated STNO-SW devices [Nal13]. Other nanoscale logic devices have been proposed over the years [Khi08b, Khi10, Khi08a, Khi07, Khi02, Cho06, Lee08], where spin wave interference effects are used to create logical output. All-electrical spin-wave spectroscopy has been shown to be an efficient technique for the excitation and detection of spin waves over distances of more than 10 μm [Cov02, Bai01, Liu07, Vla08, Vla10, Neu11d, Neu10, Due12].

Two-dimensional and three-dimensional magnonic crystals

The study of one-dimensional magnonic devices has already lead to numerous publications showing unique properties of nanostructured MCs as it has been demonstrated that MCs can be reprogrammed via the magnetic history [Top10]. Recently, two-dimensional MCs consisting of a periodic lattice of nanoholes, i.e., so-called magnetic antidot lattices (ADLs), have generated in particular great interest [Gul03]. Such devices are the magnetic analog of photonic crystals making use of air holes in a dielectric layer [Joa08]. So far, the magnetic devices have been investigated in magnetic fields $\mathbf{H}$ applied in the plane of the ferromagnetic thin film being mostly $\mathrm{Ni}_{80}\mathrm{Fe}_{20}$ (Py) [Gue00, Yu03, Yu04, McP05, Pec05, Yu07, Mar07, Kos08a, Neu08, Tse09, Neu10, Tac10a, Tac10b, Ulr10, Hu11]. Allowed minibands and partial band gaps have been observed but only for specific directions of the wave vector k [Neu11d, Ziv12]. The dispersion relations have been found to depend crucially on $\mathbf{H}$, because inhomogeneous demagnetization fields created by the holes varied significantly the refractive index of the spin waves in the permalloy thin films [Neu08, Hu11]. This provoked spin-wave localization counteracting miniband formation. A different approach is presented in this thesis as we turn the external magnetic field into the out-of-plane direction, which increases the homogeneity of the internal field. Thereby magnetostatic forward volume waves (MSFVWs) are provoked that are particularly interesting for coherent mode formation in MCs as they exhibit a isotropic dispersion relation and at the same time the lowest propagation loss per unit time [Ari99, Sta09]. In this thesis, we predict complete band gaps in our two-dimensional MCs and we report on efficient spin wave guiding in complex geometries based on MCs making use of MSFVWs.

Extending the field of MCs into the third dimension has been proposed by theoretical calculations with predictions of large band gaps [Kra08a, Kra08b]. In spite of these encouraging predictions, there is a lack of experimental work on 3D MCs as the preparation of such is a great challange. Recently, Kostylev et al. have presented very interesting results on 3D inverse opal structures [Kos12] as a possible candidate for a 3D MC. In the meantime, the field of bioengineering has been growing over the past years with remarkable results, e.g. to create arrays of nanoparticles by self-assembly of monodisperse colloidal nanocrystals [Bla00, Pil06]. Furthermore, a true order in all three dimensions has been achieved by protein crystallization technique of magnetic nanoparticles [Kas08]. The combination of bio-assisted methods to create 3D structures on the length scale of the magnetic exchange interaction opens completely new possibilities for the field of magnonics. Within this work, we present first results on magnetoferritin crystals arranging magnetic nanoparticles on a fcc lattice with a few nm spacing. We find proof of dynamic coupling between individual nanoparticles, supporting fast spin-wave propagation.

Chiral helimagnets

One year after the discovery of ferromagnetic resonance [Gri46] in 1946, C. Kittel explained the uniform spin-precession mode in homogeneously magnetized ferromagnets when irradiated by electromagnetic waves in the GHz frequency range [Kit48]. The so-called Kittel formula is powerful for both metallic and insulating ferromagnets. Later, it was realized that inhomogeneous magnetic states such as bubble domains [Bar77] support a distinct set of eigenexcitations consisting of acoustic, optical and flexible domain wall modes. A renewed interest in such excitations has stimulated research in recent years [Gub12]. During the time, much more complex magnetic states were identified where the Skyrmion lattice is one example among others such as canted ferromagnets and helimagnets. Chiral helimagnets found in non-centrosymmetric crystals have further stimulated research in recent years due to the very unique phase diagram [MÖ9, Neu09a, Yu11, Ono12]. In metallic MnSi, a topologically stable spin texture, i.e, the Skyrmion lattice, has been demonstrated in the A-phase at low temperature and finite magnetic field. Strikingly, the Skyrmion lattice is moved by a current of relatively small density due to the spin transfer torque. This holds great promise for future applications in spintronics [Jon10, Sch12a]. At the same time, the Skyrmions are of enormous interest in the emerging field of magnonics [Kru10] as they form a lattice which periodically modulates the magnetic properties in a self-organized manner. In MnSi, the period is strikingly small and on the 10 nm scale that it is in particular not routinely feasible via state-of-the-art nanolithography. Intriguing magnonic crystal behavior might result from the Skyrmion lattice going beyond nanostructured ferromagnetic materials. Within the framework of this thesis we study three different chiral helimagnetic materials, i.e. metallic MnSi, semiconducting $Fe_{1-x}Co_xSi$, and insulating Cu_2OSeO_3.

We report on their GHz excitations and find excellent agreement with a universal theoretical description for all chiral helimagnetic materials investigated. This universal theory of excitations can be applied in a universal manner to chiral helimagnets like the Kittel formula for ferromagnets. Furthermore, we explore the measured linewidth, i.e. the damping of the system. We find unique dependencies of the linewdith, which differ for different regions of the phase diagram.

Overview of the thesis

This work is organized as follows: In chapter 2, we present the theory on ferromagnetism, dynamics, spin-waves, nanoparticles, and chiral helimagnets together with numerical methods. In chapter 3, we describe our experimental setup used within this thesis, i.e. all-electrical spin-wave spectroscopy. In chapter 4, we explain sample preparation using optical lithography as well as focused ion beam lithography. In chapter 5, we make material considerations especially for the excitation of MSFVW. In chapter 6, we study 2D magnonic crystals, i.e. antidots in a regular square lattice. In chapter 7, we evaluate excitations in 3D magnonic crystals, i.e. regular arrays of nanoparticles so-called magnetoferritin crystals. In chapter 8, we report on GHz excitations in chiral helimagnets together with a universal theory for such. We finish this thesis with a summary and outlook in chapter 9.

2. Theory

In this chapter, we give a brief description of the theory of ferromagnetism. From this we explain the ferromagnetic resonance basics before introducing spin waves. After an excursion into GHz excitations in nanoparticles with bulk and surface anisotropy, we give a short introduction to chiral magnets and their complex dynamic bahvior. The model of nanoparticles has been developed by M. Krawczyk from the Adam Mickiewicz University in Poznan. The theory on chiral helimagnets has been provided by Prof. A. Rosch's group at the University of Cologne in order to interpret experimental data obtained within the course of this work (see chapter 8). Furthermore, we introduce numerical methods used throughout this work, i.e. micromagnetic- and electromagnetic simulations. In the following the brief description is based on the textbooks as Refs. [Kit66, Gur96, Blu01, Hil02, Spa03, Sko08, Sta09]

2.1. Ferromagnetism

The magnetic susceptibility $\hat{\chi}$ classifies magnetic materials through their response of the magnetization **M** to an external field **H**:

$$\mathbf{M} = \hat{\chi}\mathbf{H}, \tag{2.1}$$

where **M** is defined as microscopic magnetic moments **m** per volume [Sko08]:

$$\mathbf{M} = \frac{\mathrm{d}\mathbf{m}}{\mathrm{d}V}. \tag{2.2}$$

In general, $\hat{\chi}$ is a tensor so that **H** and **M** do not need to be collinear to each other. Simplified to a scalar χ can take one of the following values in order to classify magnetic materials:

- $\chi < 0$: Diamagnetic materials. These materials create a magnetic field that counteracts the external magnetic field **H** due to orbital magnetic moments of electrons, which means that these materials are repelled from magnetic fields. Diamagnetic effects are very small and are usually not observed in everday life.

- $\chi > 0$: Paramagnetic materials. Uncompensated spins of electrons align parallel to **H** and therefore give rise to an increased flux density. Paramagnets are attracted by an external magnetic field but unlike ferromagnets, they do not retain their magnetization when the field is removed.
- $\chi \gg 0$: Ferro- and ferrimagnetic materials. These two types of magnetic materials have in common that they both retain a finite magnetization even if the external field **H** is removed, i.e. they exhibit spontaneous magnetization. The main difference is that ferrimagnetic materials consist of differently oriented ferromagnetic sublattices, where the magnetic moments are not canceled out. This mostly happens if the sublattices are made up of two different atoms or ions. Above the Curie temperature these materials become paramagnetic.
- $\chi > 0$: Antiferromagnetic materials. Can be described by two interpenetrating and identical sublattices of magnetic moments. One set of magnetic moments is spontaneously magnetized below some critical temperature (Néel temperature), the second set is spontaneously magnetized by the same amount in the opposite direction. Therefore, aniferromagnetic moments cancel out and there is no macroscopic magnetization left. Above the Néel temeprature antiferromagnets undergo a phase transition and become paramagnetic.

In this work, we are working with ferromagnetic materials, i.e. $\chi \gg 0$. Next we want to take a closer look at the energy contributions leading to spontaneous magnetization in ferromagnets. Exchange interaction gives rise to the first energy contribution we want to look at. Exchange originates from Coulomb interaction considering the quantum mechanical Pauli exclusion principle, which says that two fermions cannot be in the same state. The Hamiltonian for this exchange interaction is the sum of interactions between the spins **S** of localized individual magnetic moments, here given in the Heisenberg notation:

$$\mathscr{H} = -\sum_{i,j} J_{ij} \hat{\mathbf{S}}_i \cdot \hat{\mathbf{S}}_j, \tag{2.3}$$

where J_{ij} is the exchange integral that quantifies the strength of interaction. A ferromagnetic order is achived when J_{ij} has a positive sign, leading to a lower energy for parallel alignment of the spins. Using Eq. 2.3 with spin vectors instead of quantum mechanical operators we can write the exchange energy $\mathscr{E}_{\text{ex}}$ as

$$\mathscr{E}_{\text{ex}} = -J \sum_{i,j} \mathbf{S}_i \cdot \mathbf{S}_j = -2J \sum_{i<j} \mathbf{S}_i \cdot \mathbf{S}_j . \tag{2.4}$$

As the exchange interaction falls off very rapidly as a function of distance between spins, this interaction is nearly a next-neighbor interaction [Kit66]. Nevertheless, exchange interaction is the cause for long range ordering in ferromagnets because of its strength. It leads to the splitting between the spin-up and spin-down bands in itinerant ferromagnets considered in this thesis on the order of 1 eV [Sto06]. Using a Taylor approximation for Eq. 2.4 one derives:

$$\mathscr{E}_{ex} = \int \mathrm{d}\mathbf{r} \frac{A}{M^2} \left(\nabla \cdot \mathbf{M} \right)^2 , \tag{2.5}$$

where A is the exchange constant. In general, where A and $\mathbf{M}$ are position dependent, the exchange field is given by:

$$\mathbf{H}_{\text{ex}} = \left(\nabla \lambda_{ex}^2 \nabla \right) \mathbf{M}, \tag{2.6}$$

where λ_{ex} is the exchange length given by:

$$\lambda_{\text{ex}} = \sqrt{\frac{2A}{\mu_0 M_s^2}}, \tag{2.7}$$

where M_{s} is the saturation magnetization.

Another contribution to the total energy is the Zeeman energy $\mathscr{E}_{\text{Z}}$, which describes the interaction of the magnetization $\mathbf{M}$ with an external field $\mathbf{H}$:

$$\mathscr{E}_{\text{Z}} = -\frac{\mu_0}{V} \int \mathrm{d}V \mathbf{M}(\mathbf{r}) \cdot \mathbf{H}. \tag{2.8}$$

The energy is thus minimized if the magnetization is aligned in the direction of the external field.

A further contribution is the so-called demagnetization energy $\mathscr{E}_{\text{d}}$ and the corresponding demagnetization field $\mathbf{H}_\text{d}$ leads to shape anisotropy. It has its origin in long range dipole-dipole interaction between spins. The energy term is written as:

$$\mathscr{E}_\text{d} = -\frac{\mu_0}{2V}\int_\text{sample} \mathrm{d}V\mathbf{M(r)}\cdot\mathbf{H}_\text{d}(r), \tag{2.9}$$

where $\mathbf{H}_\text{d}(r)$ is the position dependent demangetization field. This quantity $\mathbf{H}_\text{d}$ can be derived by using magnetostatic Maxwell equations:

$$\mu_0\nabla\cdot(\mathbf{M}+\mathbf{H}_\text{d}) = 0 \tag{2.10}$$

$$\nabla\times\mathbf{H}_\text{d} = 0. \tag{2.11}$$

Even though the calculation of $\mathbf{H}_\text{d}$ can be very complicated it is simple for the case of a uniformly magnetized ellipsoid, where the demagnetization field is homogeneous inside the ferromagnet and a linear function of the magnetization [Aha06]:

$$\mathbf{H}_\text{d} = \hat{N}\mathbf{M}. \tag{2.12}$$

Here we have introduced the demagnetization field tensor $\hat{N}$ given in the appropriate coordinate system:

$$\hat{N} = \begin{pmatrix} N_x & 0 & 0 \\ 0 & N_y & 0 \\ 0 & 0 & N_z \end{pmatrix}, \tag{2.13}$$

where the trace of this dimensionless demagnetization field tensor fulfills N_x+N_y+N_z = 1. For the case of a sphere the diagonal elements are N_x=N_y=N_z = 1/3. This tensor has been calculated for different geometries, e.g. for thin magnetic films [Kal86] and for ferromagnetic wires [Gus02]. Whereas for complex two-dimensional structures an analytical solution does not exist. In the course of this work we study various sample geometries and we will use N_x, N_y, and N_z in order to account for the specific geometry.

Finally, we consider an anisotropy energy term, which means that the energy of a sample is dependent on the direction of the magnetization. As discussed above, one reason for an anisotropic behavior of the magnetization can be shape anisotropy due to dipolar energy. But even without this effect, an infinitely extended homogenous single crystal can exhibit an anisotropic energy landscape if one considers spin-orbit interaction. Through this, the energy of the spins is coupled to the symmetry of the crystal lattice. The energy term for a cubic crystal reads:

$$\mathscr{E}_{\text{cub}} = K_1 \left(m_x^2 m_y^2 + m_y^2 m_z^2 + m_z^2 m_x^2 \right) + K_2 m_x^2 m_y^2 m_z^2, \tag{2.14}$$

where m_i are the components of the normalized magnetization $\mathbf{m}$ projected to the cubic axis of the lattice. One can also write this formula using the direction cosines of the normalized magnetization α_i, which is $\alpha_i = \mathbf{e}_i \cdot \mathbf{m}_i$. The respective anisotropy field can be calculated using:

$$\mu_0 H_1 = \frac{2K_1}{M_{\text{s}}}. \tag{2.15}$$

Another volume anisotropy is the uniaxial anisotropy:

$$\mathscr{E}_{\text{uni}} = -K_{\text{u}} m_x^2. \tag{2.16}$$

For K_{u} being positive the x-axis becomes a magnetically easy-axis, whereas for negative values of K_{u} the x-axis is considered a hard-axis. Besides those volume anisotropies, one has to consider surface anisotropies, e.g. in thin films [Bil07] and nanoparticles [Kac06, Yan07]. In thin films this anisotropy term is described using a phenomenological uniaxial perpendicular anisotropy parameter $K_{\perp}$ as:

$$\mathscr{E}_{\perp} = -\frac{K_{\perp}}{d} m_z^2, \tag{2.17}$$

where d is the thickness of the film. For very thin films, this anisotropy can even dominate the demagnetization energy leading to a stable perpendicular magnetization. The anisotropy field can be written as:

$$H_{\perp} = -\frac{2K_{\perp}}{\mu_0 M_{\text{s}} d} m_z^2. \tag{2.18}$$

This relation is used to determine the surface anisotropy in thin films using ferromagnetic measurements as shown later on.

In systems with broken inversion symmetry, i.e. if there is no inversion center between magnetic sites, the Dzyaloshinskii-Moriya interaction

(DMI), which has a preferred chirality, has to be considered. Its strength is linearly proportional to the spin-orbit coupling. Here, the coupling between two spins $\mathbf{S}_\mathrm{A}$ and $\mathbf{S}_\mathrm{B}$ on sites A and B respectively can be described by the Hamiltonian

$$\mathscr{H}_\mathrm{DM} = \mathbf{D}_\mathrm{AB} \cdot \left(\mathbf{S}_\mathrm{A} \times \mathbf{S}_\mathrm{B}\right), \tag{2.19}$$

where the coupling constant $\mathbf{D}_\mathrm{AB} \propto (\mathbf{x} \times \mathbf{r}_\mathrm{AB})$ depends on the vector $\mathbf{r}_\mathrm{AB}$ connecting the two sites, and on the displacement $\mathbf{x}$ of a ligand ion. It is important to note that DMI is antisymmetric in terms of permutation of spins. The free energy term can be written as

$$\mathscr{E}_\mathrm{DM} = \int \mathrm{d}\mathbf{r} 2D\mathbf{M(r)} \cdot (\nabla \times \mathbf{M(r)}), \tag{2.20}$$

with the coupling strength D. DMI becomes important in chapter 2.5 for chiral helimagnets, where the competition between the exchange interaction and DMI is responsible for the chirality of the spin structure in such materials.

In order to calculate the total energy density we have to sum up all energy contributions, which determines the alignment of the magnetic moments:

$$\mathscr{E}_\mathrm{tot} = \mathscr{E}_\mathrm{ex} + \mathscr{E}_\mathrm{DM} + \mathscr{E}_\mathrm{Z} + \mathscr{E}_\mathrm{d} + \mathscr{E}_\mathrm{cub} + \mathscr{E}_\mathrm{uni} + \mathscr{E}_\perp. \tag{2.21}$$

From this, we have to find the energy minimum in order to find the equilibrium configuration of the magnetization. The competition between the different contributions can lead to magnetic moments pointing in different directions locally. This can lead to complicated domain formation when the total energy is minimized. Using the total energy density we can formulate the total effective magnetic field:

$$H_\mathrm{eff} = -\frac{1}{\mu_0} \nabla_\mathbf{M} \mathscr{E}_\mathrm{tot}. \tag{2.22}$$

2.2. Magnetization Dynamics

So far we have discussed the contributions to static magnetism. Now we consider magnetization dynamics. We use a macrospin model where all magnetic moments are summed up to a single macro spin represented by the magnetization vector **M**. For simplicity, we assume that the governing energy term is the Zeeman energy, which means that the external field H_{ext} is strong enough to align all moments in the direction of the external field. The basic formula for magnetization dynamics was first proposed by Landau and Lifshitz [Lan35]:

$$\frac{\mathrm{d}\mathbf{M}}{\mathrm{d}t} = -\gamma\mu_0\mathbf{M} \times \mathbf{H}_{\text{eff}}, \tag{2.23}$$

where γ is the gyromagnetic ratio defined as $g\,|e|/(2m_{\text{e}})$. Here g is the g-factor, e the electron charge, and m_{e} is the mass of an electron. Using this model, we introduce the torque τ acting on the magnetization, which leads to a precessional motion around the effective field as depicted in Fig. 2.1:

$$\tau = \mu_0\mathbf{M} \times \mathbf{H}_{\text{eff}}. \tag{2.24}$$

Using the above stated model would lead to a infinite long precessional motion of the magnetization around the equilibrium state. As this is not anticipated and observed in experiments, a phenomenological damping term is included[Lan35]:

$$\frac{\mathrm{d}\mathbf{M}}{\mathrm{d}t} = -\gamma\mu_0\mathbf{M} \times \mathbf{H}_{\text{eff}} - \frac{\lambda}{M_{\text{s}}^2}\mathbf{M} \times \left(\mathbf{M} \times \mathbf{H}_{\text{eff}}\right), \tag{2.25}$$

considering the damping parameter λ. Although this equation could account for the observed experimental data, it fails for large values of λ. Therefore, a different damping term was proposed by Gilbert [Gil55], where the damping depends on the time derivative of the magnetization:

$$\frac{\mathrm{d}\mathbf{M}}{\mathrm{d}t} = -\gamma\mu_0\mathbf{M} \times \mathbf{H}_{\text{eff}} - \frac{\alpha}{M_{\text{s}}}\left(\mathbf{M} \times \frac{\mathrm{d}\mathbf{M}}{\mathrm{d}t}\right), \tag{2.26}$$

where α is the phenomenological Gilbert damping term. Equation 2.26 is called the Landau-Lifshitz-Gilbert equation and is mostly employed in magnetization dynamics. It can be shown that for small values of α, both equations are equivalent [Mal03]. We stress that the damping term is a phenomenological approach as to describe the process of energy dissipation. In general, the contributions to the damping term are numerous and complicated. Under specific conditions, it is possible to extract α from experiments. To find an analytical solution for the Landau-Lifshitz-Gilbert

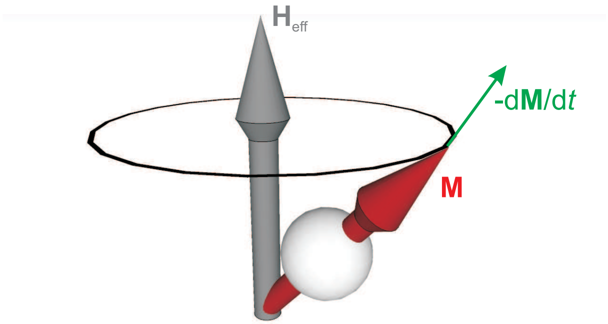

Figure 2.1.: Precessional motion of the magnetization **M**, represented by a makro spin, around the effective internal field H_{eff}. $\frac{\mathrm{d}\mathbf{M}}{\mathrm{d}t}$ is pointing perpendicular to the field and the magnetization describing the precession. If the motion is damped the cone angle of the precessional motion is continuously decreased, leading to a spiral motion, until **M** and **H** are aligned again.

equation in a general form is not feasible. However, under certain assumptions one can solve the problem for the case of a thin film [Kit48]. For this, we have to make the assumption that the film is extended infinitely in the xy-plane so that we can set the demagnetization factors to N_z=N_y = 0 and N_x = 1. We take a uniaxial anisotropy with an easy-axis in the x-direction into account. Furthermore, we assume that the magnetization is parallel to the effective field pointing along the x-direction, whereas the excitation field $\mathbf{h}_{\mathrm{ex}}(t) = \mathbf{h}_{\mathrm{ex}}\exp(\mathrm{i}\omega t)\hat{\mathbf{y}}$ is small and pointing along the y-direction. Also, we use a uniform excitation, i.e. a wave vector k = 0. We also take perpendicular anisotropy induced by the surface into account but we restrict this to small values so it does not exceed the demagnetization field. Following Ref. [Gie05] we obtain the real and imaginary part of the susceptibility:

$$\mathscr{R}\left(\chi_{yy}\right) = \chi_{yy}^{'} = \frac{\omega_{\mathrm{M}}\left(\omega_{\mathrm{H}}+\omega_{\mathrm{eff}}\right)\left(\omega_{\mathrm{res}}^2-\omega^2\right)}{\left(\omega_{\mathrm{res}}^2-\omega^2\right)^2+\alpha^2\omega^2\left(2\omega_{\mathrm{H}}+\omega_{\mathrm{eff}}\right)^2}, \tag{2.27}$$

$$\mathscr{I}\left(\chi_{yy}\right) = \chi_{yy}^{''} = \frac{\alpha\omega\omega_{\mathrm{M}}\left[\omega^2+\left(\omega_{\mathrm{H}}+\omega_{\mathrm{eff}}\right)^2\right]}{\left(\omega_{\mathrm{res}}^2-\omega^2\right)^2+\alpha^2\omega^2\left(2\omega_{\mathrm{H}}+\omega_{\mathrm{eff}}\right)^2}. \tag{2.28}$$

Here, we have introduced the following terms:

$$\omega_M = \gamma\mu_0 M_\text{s};\ \omega_\text{H} = \gamma\mu_0\left(H_\text{ext} + H_\text{uni}\right);\ \omega_\text{eff} = \gamma\mu_0 M_\text{eff}, \tag{2.29}$$

where $H_\text{uni}=\frac{2K_\text{u}}{\mu_0 M_\text{s}}$ contains the uniaxial anisotropy and M_eff includes the contribution of perpendicular surface anisotropy:

$$M_\text{eff} = M_\text{s} - \frac{2K_\perp}{d\mu_0 M_\text{s}}. \tag{2.30}$$

The imaginary part of the susceptibility, i.e. Eq. 2.28, can be approximated using a Lorentzian function, which has its maximum at the resonance frequency:

$$\omega_\text{res}^2 = \omega_\text{H}\left(\omega_\text{eff} + \omega_\text{H}\right). \tag{2.31}$$

This is a special case of the well known Kittel formula [Kit48], which contains the demagnetization factors:

$$\omega_\text{res}^2 = \left(\omega_\text{H} + \left(N_x - N_z\right)\omega_\text{M}\right)\left(\omega_\text{H} + \left(N_y - N_z\right)\omega_\text{M}\right). \tag{2.32}$$

If we set N_z=N_y = 0 and N_x = 1, Eq. 2.32 gets the form of Eq. 2.31, where $\omega_\text{M} \rightarrow \omega_\text{eff}$. The uniform excitation is called ferromagnetic resonance (FMR). As mentioned above, Eq. 2.31 is the field dependent resonance frequency for a thin film in an external magnetic field in the x-direction. For the case of an external magnetic field perpendicular to the thin film plane, i.e. the out-of-plane direction, we can rewrite the demagnetization tensor in that we set N_x=N_y = 0 and N_z = 1. From this, we obtain the field dependent resonance frequencies for a magnetic field ($H_\text{ext} > H_\text{d}$) pointing perpendicular to the film plane [Sta09]:

$$\omega_\text{res} = \omega_\text{H} - \omega_\text{eff}. \tag{2.33}$$

where again $\omega_\text{M} \rightarrow \omega_\text{eff}$. From Eq. 2.33 we see that the resonance frequency increases linearly with the external field and the slope is given by $\gamma/2\pi$.

Considering a Lorentzian shape of the imaginary part of the susceptibility and therefore ω. The full width at half maximum (FWHM) of ω is defined as the frequency linewidth of the imaginary part of the susceptibility [Bil07]:

$$\Delta\omega = \alpha(2\omega_\text{H} + \omega_\text{eff}). \tag{2.34}$$

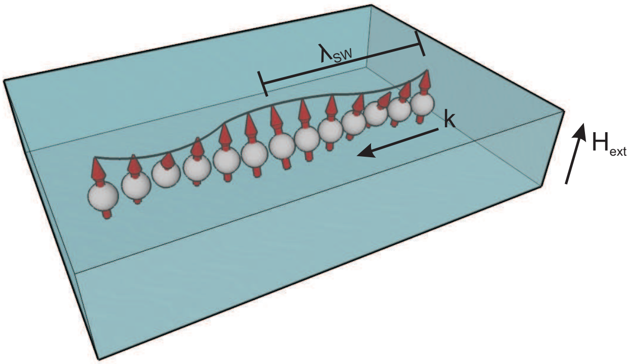

Figure 2.2.: Spin wave with wavelength λ_{SW} propagating in a ferromagnetic thin film. The external field is applied along the out-of-plane direction, i.e. normal to the film plane, leading to a magnetostatic forward volume wave. The direction of phase evolution is indicated by k.

As the imaginary part of the susceptibility is not completely symmetric around the resonance frequency the Lorentzian shape is a small approximation and should be kept in mind.

2.3. Spin Waves

So far we have restricted our discussion to uniform excitation in a thin film, i.e. wave vector $k = 0$. Here, the magnetic moments precess at the same phase. Next, we want to look at excitations of non-zero wave vector. As this corresponds to a collective excitation of magnetic moments exhibiting a finite wavelength λ_{SW}, we call this a spin wave or magnon if the quantized nature would be relevant. Spin waves of short wavelengths are exchange dominated, whereas spin waves with a long wavelength are dominated by magnetic dipole interaction. The corresponding waves are called magnetostatic waves, which we will address here. In Fig. 2.2, we show a sketch of such a spin wave traveling in a material with a finite wavelength in a certain direction indicated by k.

We start with the basic Maxwell equations in the abscence of currents in the magnetostatic limit:

$$\nabla \times \mathbf{H} = 0;\ \nabla \cdot \mathbf{B} = 0;\ \nabla \times \mathbf{E} = -\dot{\mathbf{B}}. \tag{2.35}$$

We use the magnetic induction given by:

$$\mathbf{B} = \mu_0 \left(1 + \bar{\bar{\chi}}\right) \mathbf{H}. \tag{2.36}$$

Here, we have introduced $\bar{\bar{\chi}}$ as the high-frequency susceptibility derived from the Landau-Lifshitz equation without loss. Using the magnetostatic potential ψ in $\mathbf{H} = -\nabla\psi$ allows us to write down Walker's equation [Sta09]:

$$(1 + \bar{\bar{\chi}}) \left[\frac{\partial^2 \psi}{\partial x^2} + \frac{\partial^2 \psi}{\partial y^2}\right] + \frac{\partial^2 \psi}{\partial z^2} = 0. \tag{2.37}$$

Assuming that the spatially modulated potential is proportional to a uniform plane wave, i.e. $\psi \propto \exp(\imath \mathrm{k} \cdot \mathrm{r})$, we are able to find the dispersion relation:

$$(1 + \bar{\bar{\chi}}) \left(k_x^2 + k_y^2\right) + k_z^2 = 0. \tag{2.38}$$

We define the group- and phase velocity as

$$v_{\mathrm{g}} = \frac{\partial \omega}{\partial k} \quad ; \quad v_{\mathrm{p}} = \frac{\omega}{k}, \quad \text{respectively}. \tag{2.39}$$

From this, the different magnetostatic modes are obtained by choice of appropriate boundary conditions and relations for the different components of k [Wal57]. In the following, we distinguish between three different magnetostatic modes found in thin films, where we neglect anisotropy and exchange interaction. The different modes are characterized by the angle between the magnetization and the in-plane wave vector $k_{||}$.

- ◇ **Magnetostatic surface wave (MSSW):**
  The name of this wave stems from the fact that the amplitude decays exponentially from the surface. It is often called Damon-Eshbach (DE) mode as they were first described by Damon and Eshbach [Dam61]. This wave is observed when $k_{||}$ is perpendicular to the magnetization and **M** lies in the sample plane. Their dispersion re-

lation is given by [Sta09]:

$$\omega_{\text{MSSW}}^2 = \omega_{\text{H}}\left(\omega_{\text{H}} + \omega_{\text{eff}}\right) + \frac{\omega_{\text{eff}}^2}{4}\left(1 - \mathrm{e}^{-2k_{||}d}\right). \tag{2.40}$$

This wave has a positive group velocity v_{g} as can be seen from the positive slope depicted in Fig. 2.3 (a). In the limiting case for $k \to 0$ we get Eq. 2.31. Note that for $d << \lambda_{\text{SW}}$ the exponential decay across the film thickness is not significant.

- **Magnetostatic backward volume wave (MSBVW):**
  This mode is called a backward mode cause it exhibits a negative group velocity (see Fig. 2.3 (a)). In contrast to MSSW this mode's amplitude is distributed uniformly throughout the film's volume, which is why it is called a volume mode. The configuration of $k_{||}$ and **M** is collinear to each other while being in the sample plane. The dispersion relation is given by [Kal86]:

$$\omega_{\text{MSBVW}}^2 = \omega_{\text{H}}\left[\omega_{\text{H}} + \omega_{\text{eff}}\left(\frac{1 - \mathrm{e}^{-k_{||}d}}{k_{||}d}\right)\right]. \tag{2.41}$$

- **Magnetostatic forward volume wave (MSFVW):**
  As the name suggests this mode has a positive group velocity and the amplitude is uniformly distributed throughout the film's volume. Here, the magnetization points in the out-of-plane direction, i.e. perpendicular to the film plane. It is worth mentioning that this mode does not depend on the direction of the in-plane wave vector $k_{||}$. The dispersion relation is isotropic and given by [Sta09]:

$$\omega_{\text{MSFVW}}^2 = \omega_{\text{H}}\left[\omega_{\text{H}} + \omega_{\text{eff}}\left(1 - \frac{1 - \mathrm{e}^{-k_{||}d}}{k_{||}d}\right)\right]. \tag{2.42}$$

In general this mode exhibits a smaller group velocity v_{g} at small wave vectors (see Fig. 2.3 (a-b)), but the MSFVW are of particular interest for coherent mode formation in MCs as they exhibit the lowest propagation loss per unit time [Sta09]. We will study this kind of mode extensively throughout this work. Because readers are expected to be more familiar with the MSSW and MSBVW, we give some extra information on the group velocity in Fig. 2.3 (c-d). In

Fig. 2.3 (c), we display the variation of the group velocity on the wave vector in the dipolar regime and in Fig. 2.3 (d), we show the dependency of the group velocity on the film thickness d. In the inset of Fig. 2.3 (c) we also show the dependency of the group velocity on the external field. To generate the plots in Fig. 2.3 we used the following parameter: 41 nm thick CoFeB with M_s = 1430 kA/m and an out-of-plane anisotropy of $K_\perp$ = 2.9 mJ/m^2. For the k-dependent plots we set the external field to 100 mT (1.8 T) for DE and MSBVW (MSFVW). The field dependency and the thickness dependency of the group velocity was evaluated around k = 0.6 $\times$ 10^4 rad/cm.

As mentioned above, we restrict this chapter to dipole-dipole dominated modes but we mention that exchange-dominated spin waves exist for small wavelength, where the exchange interaction dominates. Also, one should keep in mind that perpendicular standing spin waves can occur, where the wave vector is in the perpendicular direction and the surface of the thin film sets the boundary conditions. As these modes are not the subject of this work we will leave it up to the interested reader to follow the work of e.g. Bilzer [Bil07].

2.4. Ferromagnetic Resonance of Nanoparticles

In chapter 7, we study dynamic excitations in ordered nanoparticle (NP) systems. Here, we derive an analytical formula to fit the experimental data and to get a deeper understanding of the physics involved in dynamics in NPs. The calculations are done by Dr. Maciej Krawczyk from the Adam Mickiewicz University in Poznan. Before we start with the derivation, we briefly discuss the already existing studies on dynamic excitations in NPs, which have been addressed in several papers using different assumptions. By excluding exchange interaction, Walker et. al [Wal57] found rich spectra of magnetostatic excitations. Uniform spin wave modes with volume magnetocrystalline anisotropy of uniaxial and cubic character where considered in Refs. [Sur92, Bia03] and Ref. [Art57], respectively. Higher standing modes in spherical NP, i.e. with nonzero azimuthal and radial nodalpoints, where the exchange contribution dominates were considered by Aharoni in Refs. [Aha91, Aha97]. The influence of both exchange and dipolar interactions were considered in Ref. [Ari05]. The fundamental

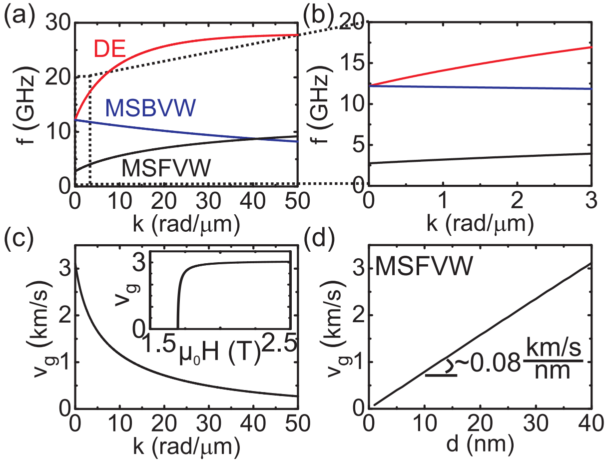

Figure 2.3.: Spin wave dispersion relation in the dipolar regime (a) and at very small wave vectors (b) at which all-electrical spin-wave spectroscopy experiments take place. The group velocity for MSFVW in (c) is calculated from the slope of the dispersion relation and the dependency on the film thickness is shown in (d). Parameters for the calculations are given in the text.

mode in NPs with surface anisotropy of uniaxial character or unidirectional character (always parallel to the magnetization vector) were investigated in Refs. [Shi99a, Mer00] and [Shi99b] respectively. The surface anisotropy modifies the boundary conditions for magnetization dynamics, i.e. it changes the magnetization pinning and the frequency of spin waves. Besides uniaxial and unidirectional surface anisotropy, Neel type surface anisotropy was also considered in NPs [Kac06, Yan07]. The magnetic configuration and types of anisotropies present in magnetoferritin NPs is still unresolved [Bic50].

In our model, we assume that the kernel of the magnetic NP is characterized by the magnetization vector $\mathbf{M}$ of constant length ($|\mathbf{M}| \equiv M_\mathrm{s}$), exchange constant A, and volume magnetic anisotropy with constant K_u. Furthermore, we include a single surface anisotropy constant $K_\perp$ [Aha91]. For the derivation of spin wave resonance, we follow the standard procedure by minimization of the total magnetic energy:

$$\mathscr{E}_{\text{tot}} = \int \mathscr{E}_{\text{V}} dV + \oint \mathscr{E}_{\perp} dS, \tag{2.43}$$

where $\mathscr{E}_{\text{V}}$ is composed of four elements:

$$\mathscr{E}_{\text{V}} = \mathscr{E}_{\text{ex}} + \mathscr{E}_{\text{uni}} + \mathscr{E}_{\text{d}} + \mathscr{E}_{\text{Z}}. \tag{2.44}$$

The integration in Eq. (2.43) is performed over the NP's kernel volume V and over its surface area S, in the first and second integral, respectively. We took the uniaxial volume anisotropy instead of a cubic anisotropy for convenience. For magnetization along [001] direction a volume anisotropy of cubic crystals in first approximation reduces to the uniaxial form [Chi97]. Moreover it was shown in Ref. [Gaz98] that magnetoferritin NPs behave like a magnet with uniaxial volume anisotropy. In fact low temperature magnetic anisotropy in bulk magnetite is still under discussion [Bic50, Mux00]. The calculations can be straightforwardly extended to cubic anisotropy [Cha11]. We will also limit us to the unidirectional type of surface anisotropy. An extensive discussion of the influence of various forms of the surface anisotropy on magnetization dynamics can be found in Ref. [Fio05].

The calculation of spin wave spectra in dependence on the intensity of the magnetic field requires a two step procedure for arbitrary direction of the magnetic field with respect to the magnetic anisotropy axis. In the first step, the equilibrium direction of the magnetization is calculated, then the normal modes of the spin wave oscillations are calculated in a linear approximation. The equilibrium direction of the magnetization vector can be derived by minimization of the energy functional Eq. (2.43) under the condition of a fixed value of $|M|$ [Bro63]. It is equivalent to finding the minimum of the functional (2.43) with respect to spherical coordinates φ and θ of the magnetization vector defined in Fig. 2.4, where we chose the magnetocrystalline anisotropy axis to be parallel to the z-axis. The conditions for extremum of the function:

$$\frac{\partial \mathscr{E}_{\text{V}}}{\partial \varphi} = 0 \quad \text{and} \quad \frac{\partial \mathscr{E}_{\text{V}}}{\partial \theta} = 0 \tag{2.45}$$

provide us with the trigonometrical equation:

$$K_\mathrm{u} \sin 2\theta = -M_\mathrm{s} H_\mathrm{ext} \sin(\theta_H - \theta), \tag{2.46}$$

with $\varphi_\mathrm{H} = \varphi$ for uniaxial anisotropy. θ_H and φ_H are angles of the external magnetic field with respect to the z-axis (Fig. 2.4). Taking into account only solutions with second derivatives of $\mathscr{E}$ with respect to angles larger than 0. Thus the equilibrium orientation of the magnetization vector $\mathbf{M} \equiv \mathbf{M}_0$ (with unit vector $\mathbf{e}_0$ with spherical coordinates φ_0 and θ_0) for a given $\mathbf{H}_\mathrm{ext}$ is found.

The equilibrium orientation of the magnetization allows us to look for

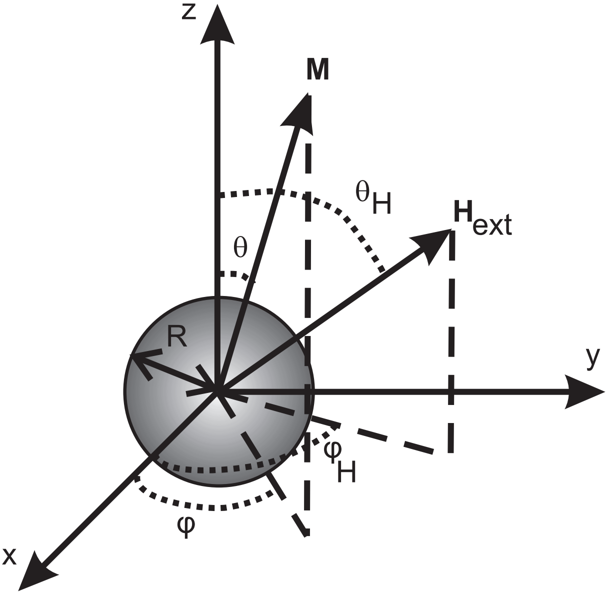

Figure 2.4.: The coordinate system used in the calculations. Parameters and angles used in the text are defined. The uniaxial magnetocrystalline anisotropy axis is along the z-axis.

solutions of the Landau-Lifshitz equation (Eq. 2.23) in linear approximation, i.e., under the assumption that dynamical components of the magnetization vector $\mathbf{m}$ are perpendicular to $\mathbf{M}_0$ and that $|\mathbf{m}| \ll M_\mathrm{s}$. The effective magnetic field $\mathbf{H}_{\text{eff}}$ is calculated as the variational derivative of $\mathscr{E}_{\text{tot}}$ with respect to the magnetization vector (c.f. Eq. 2.22):

$$\mathbf{H}_{\text{eff}} = \frac{1}{\mu_0}\nabla_{\mathbf{M}}\mathscr{E}_{\text{tot}} = \mathbf{H}_{\text{ext}} + \frac{2A}{\mu_0 M_{\text{s}}}\nabla^2\mathbf{m} + H_{\text{uni}}\left(\mathbf{e}\cdot\mathbf{n}\right)\mathbf{n} - \mathbf{H}_{\text{d}}, \quad (2.47)$$

where the volume anisotropy field is $H_{\text{uni}} = 2K_{\text{u}}/M_{\text{s}}$ [Chi97].

To find the frequencies of spin waves ω_{res}, i.e., harmonic oscillations around the equilibrium orientation, one can solve Eq. (2.23) in linear approximation with assumed harmonic time dependence of $\mathbf{m} \propto \mathrm{e}^{i\omega t}$ and complemented with boundary conditions. Boundary conditions are derived from the energy functional Eq. (2.43). Finally we obtain an equation for the frequency of the fundamental mode in a NP with uniaxial volume anisotropy (assumed to be along the z-axis), unidirectional surface anisotropy, which introduces pinning of the magnetization on the NP's surface, in an external magnetic field H_{ext} applied under the angle θ_{H} with respect to the uniaxial axis. It reads [Shi99b, Cha11]:

$$\begin{aligned}\left(\frac{\omega_{\text{res}}}{\gamma\mu_0}\right)^2 &= \left(H_\perp + H_{\text{ext}}\cos(\theta_{\text{H}}-\theta_0) + H_{\text{uni}}\cos 2\theta_0\right) \\ &\quad \left(H_\perp + H_{\text{ext}}\cos(\theta_{\text{H}}-\theta_0) + H_{\text{uni}}\cos^2\theta_0\right).\end{aligned} \quad (2.48)$$

This formula is used in chapter 7 to fit the experimental data of magnetoferritin NPs.

2.5. Theory of Magnetic Excitations in Chiral Magnets

Motivated by the experiments carried out during this work, which we present in chapter 8.1, Prof. Achim Rosch and his group at the University of Cologne developed a theoretical approach to describe the excitations found in chiral magnets using Ginzburg-Landau theory [Wai13]. This chapter is dedicated to briefly outline this theoretical analysis. Illustrations of spin configurations and excitational modes shown within this chapter are obtained by A. Rosch and his group in Cologne [Gar13]. A comparison with experiments is then presented in chapter 8.3.

2.5.1. Introduction

So called helimagnetic B20 compounds such as MnSi, FeGe, $\mathrm{Fe}_{1-x}\mathrm{Co}_x\mathrm{Si}$ and $\mathrm{Cu_2OSeO_3}$ undergo transitions between such different states as a function of magnetic field H_ext and temperature T (Fig. 2.5). At zero magnetic field and below the transition temperature T_c helimagnetic order appears. The spin configuration in the helical state is shown in Fig. 2.6 (a). While increasing the magnetic field ($\mu_0 H_\mathrm{ext} > \mu_0 H_\mathrm{c1}$), the helimagnetic state undergoes a spin-flop transition to a conical phase depicted in Fig. 2.6 (b). Here, the spins are canted towards the field direction. Further increase of the magnetic field leads to another transition to a spin-polarized state, i.e. ferromagnetic (FM) phase. Within a small pocket close to T_c lies the Skyrmion phase. Here, the spins form a vortex-like structure (Fig. 2.7) in a 2D hexagonal lattice. The magnetic phases arise from the competition between exchange interaction, Dzyaloshinskii-Moriya spin-orbit coupling and higher order spin-orbit coupling.

2.5.2. Magnetic Excitations at k = 0

In the case of chiral magnets the solution of the Landau-Lifshitz-Gilbert equation (Eq. 2.26) is complicated, because it cannot be linearized. Therefore, the total free energy in the Ginzburg-Landau model for chiral magnets is definded in analogy to the total free energy (Eq. 2.21). Its free energy functional is given by

$$\mathcal{F} = \mathcal{F}_0 + \mathcal{F}_\mathrm{dipolar} + \mathcal{F}_\mathrm{cub}, \tag{2.49}$$

where the first term $\mathcal{F}_0$ containes the Dzyaloshinskii-Moriya interaction and a Zeemann-term. [Bak80, Nak80]. $\mathcal{F}_\mathrm{dipolar}$ is the dipolar interaction and the last term $\mathcal{F}_\mathrm{cub} = \int d\boldsymbol{r}\, f_\mathrm{cub}$ contains cubic anisotropies.

The magnetic resonances are determined with the help of the equation of motion for the magnetization (c.f. Eq. 2.23). Linearizing equation 2.23 around the equilibrium configuration allows to determine the eigenmodes and eigenfrequencies. A magnetic time dependent excitation leads to a deviation from the equilibrium configuration $\mathbf{M}(\mathbf{r}, t)$ and thus to a finite effective field. The calculation of the resonance frequencies finally reduces to an eigenvalue problem of a characteristic matrix, where the amplitudes and the pitch orientation are determined by minimizing the corresponding potentials [Wai13]. In general, the magnetic eigenfrequencies

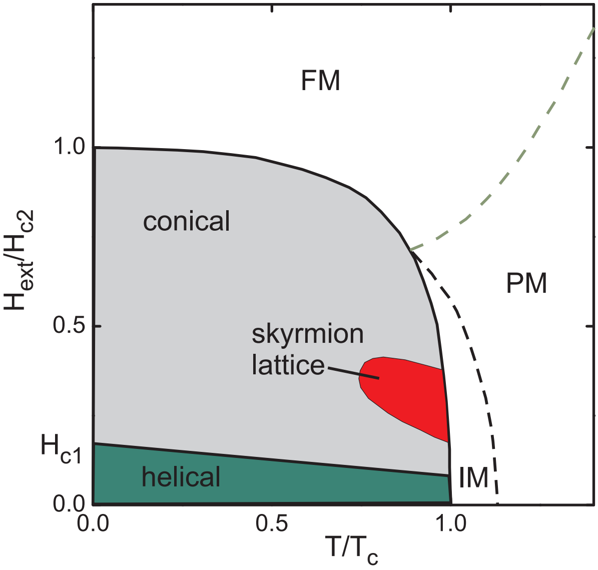

Figure 2.5.: Sketch of the phase diagram of a B20 helimagnet studied in this thesis. Below the transition temperature T_c and at zero field the helical phase is established. With increasing magnetic field one enters the conical phase before at a critical field H_{c2} the field polarized or ferromagnetic (FM) phase is reached. In a small pocket just before the critical temperature T_c the Skyrmion phase is located. Above T_c we enter the paramagnetic (PM) phase. The intermediate (IM) phase is not adressed in this work.

and its spectral weights are obtained by diagonalizing numerically the matrix. Analytical expressions for the eigenfrequencies at zero momentum[1] in the field-polarized and the conical phase can also be derived by this ansatz.

I. *Field-polarized phase* $H_{\text{ext}} > H_{\text{c2}}$

---

[1] As the distribution of the exciting magnetic field in our setup is almost homogeneous, we will discuss the magnetic excitation frequency at zero momentum $\omega^\alpha \equiv \omega^\alpha(0)$ as well as in the limit of small momenta $\lim_{|\boldsymbol{k}|\to 0} \lim_{L\to\infty} \omega^\alpha(\boldsymbol{k})$. The latter limit depends in particular on the orientation $\boldsymbol{k}$.

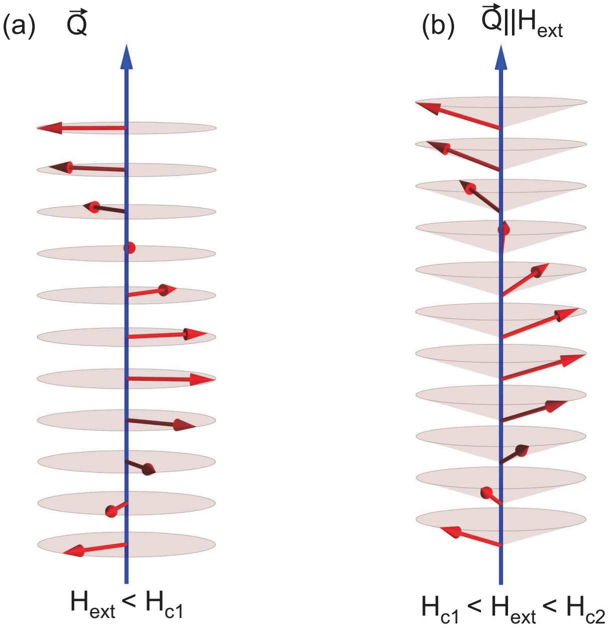

Figure 2.6.: (a) Sketch of the spin configuration in the helical phase with the helix pitch vector $\boldsymbol{Q}$. (b) Spin configuration in the conical phase where the external field is higher than H_{c1} and the spins are canted towards the field direction [Gar13].

In the field-polarized phase we obtain a single excitation mode that couples to the magnetic field. This is the standard ferromagnetic resonance with a frequency given by the Kittel formula:

$$\omega_{\text{res}} = |\gamma|\mu_0\sqrt{[H_{\text{ext}} + (N_x - N_z)M]\,[H_{\text{ext}} + (N_y - N_z)M]}, \quad (2.50)$$

with N_i $(i = x, y, z)$ being the diagonal elements of the demagnetization matrix (Eq. 2.13). In the case of $H_{\text{ext}} > H_{c2}$ the magnetization is almost saturated and we can approximate $M \approx \chi_{\text{con}} H_{c2}$ so that the resonance frequency reads

$$\frac{\hbar\omega_{\text{res}}}{|g|\mu_0\mu_B H_{c2}} \approx \sqrt{[h + (N_x - N_z)\chi_{\text{con}}]\,[h + (N_y - N_z)\chi_{\text{con}}]}. \quad (2.51)$$

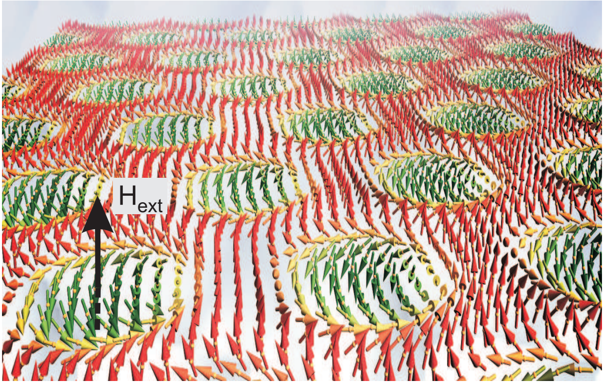

Figure 2.7.: Illustration of the Skyrmion lattice, i.e. a periodic arrangement of vortex-like structures in an fcc lattice. The spins parallel and anti-parallel to the external field H_ext are shown in red and green color respectively [Gar13].

With the reduced field $h = H/H_{\mathrm{c2}} > 1$ and the susceptibility χ_{con} defined as:

$$\chi_{\mathrm{con}} = \frac{\mu_0 \mu^2}{J_{\mathrm{eff}} Q^2 + \mu_0 \mu^2 N_z}, \tag{2.52}$$

with $\mu = \mu_\mathrm{B}/\mathrm{f.u.}$, i.e., a single Bohr magneton ($\mu_B > 0$) per formula unit and a stiffness J_eff that depends on the magnetic field orientation and the helix pitch vector $\boldsymbol{Q}$.

II. *Conical phase* $H_{\mathrm{c1}} < H_{\mathrm{ext}} < H_{\mathrm{c2}}$

In the conical phase we find two excitation modes. These eigenmodes are illustrated in Fig. 2.8. The corresponding frequencies are given by the analytical expression

$$\begin{aligned}\frac{\hbar\omega^{\pm}_{\text{res}}}{|g|\mu_0\mu_B H_{\text{c2}}} = \Big\{&\Big(1+\frac{1}{4}(N_x+N_y-4N_z)\chi_{\text{con}}\Big)\Big(2+(1\\ &-2N_z)\chi_{\text{con}}\Big)-h^2\Big(1+\chi_{\text{con}}(1+\frac{1}{4}(N_x+N_y\\ &-2N_xN_y)\chi_{\text{con}}-N_z(2+(1-N_z)\chi_{\text{con}}))\Big)\\ &\pm\frac{1}{4}\chi_{\text{con}}\Big[N_x^2\Big(2+(1-2N_z-h^2(1-2N_y))\chi_{\text{con}}\Big)^2\\ &+N_y^2\Big(2+(1-2N_z-h^2)\chi_{\text{con}}\Big)^2-2N_xN_y\Big((2\\ &+(1-2N_z)\chi_{\text{con}})^2+2h^2(4+(1+N_y-4N_z)\chi_{\text{con}})(-2\\ &-\chi_{\text{con}}+2N_z\chi_{\text{con}})+h^4(8+\chi_{\text{con}}(8+(1+2N_y)\chi_{\text{con}}\\ &+8N_z(-2+(-1+N_z)\chi_{\text{con}})))\Big)\Big]^{1/2}\Big\}^{1/2}.\end{aligned} \tag{2.53}$$

The right hand side is a function of the reduced magnetic field $h = H_{\text{ext}}/H_{\text{c2}} < 1$ and depends on the value of the susceptibility χ_{con} from Eq. (2.52), that is constant within the conical phase.

One can check that the mode ω^{+}_{res} smoothly connects to the Kittel result in the limit $H_{\text{ext}} \to H_{\text{c2}}$. In the same limit, one finds that the spectral weight of the other mode ω^{-}_{res} with the magnetic field vanishes. The susceptibility χ_{con} is a measure for the strength of the dipolar interaction energy. For a spherical sample $N_i = 1/3$, Eq. 2.53 reduces to:

$$\begin{aligned}\frac{\hbar\omega^{\pm}_{\text{res}}}{|g|\mu_0\mu_B H_{c2}}\bigg|_{N_i=1/3} &= \Big\{2-\frac{\chi_{\text{con}}}{18}-h^2\Big(1+\frac{\chi_{\text{con}}}{3}-\frac{\chi^2_{\text{con}}}{9}\Big)\\ &\pm h\frac{\chi_{\text{con}}}{18}\Big[\Big(6-\chi_{\text{con}}\Big)\Big(2(6+\chi_{\text{con}})\\ &-3h^2(2+\chi_{\text{con}})\Big)\Big]^{1/2}\Big\}^{1/2}.\end{aligned} \tag{2.54}$$

III. *Helical phase* $H_{\text{ext}} < H_{\text{c1}}$

The helical phase is the most complex phase. In zero field, $H_{\text{ext}} = 0$, the mean magnetization vanishes and the anisotropic part of the poten-

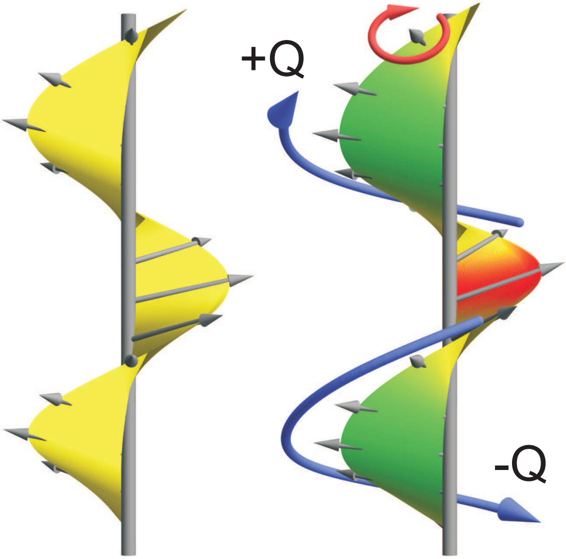

Figure 2.8.: The equilibrium spin configuration of the conical phase is shown on the left. On the right hand side the two excitation modes $\pm Q$ predicted by the theory, where the individual spin precessional motion is indicated by the red arrow [Gar13].

tial fixes the pitch vector either along a crystallographic $\langle 111 \rangle$ direction or along $\langle 100 \rangle$. A finite field in general competes with the cubic anisotropy and instead wants to align the pitch along the field. For fields along high symmetry directions, i.e., $\langle 100 \rangle$, $\langle 110 \rangle$, $\langle 111 \rangle$, that differ from the equilibrium orientation of the pitch at zero field, one expects a second-order phase transition from the helical phase to the conical phase at a critical field H_{c1} with $H_{c1} < H_{c2}$. For other directions, there is only a smooth crossover between the helical and conical phase as the pitch reorients itself.

For the helical phase the magnetic excitation spectrum was evaluated numerically. Similarly as in the conical phase, one obtains two modes within general different magnetic excitation frequencies.

IV. *Skyrmion lattice phase*

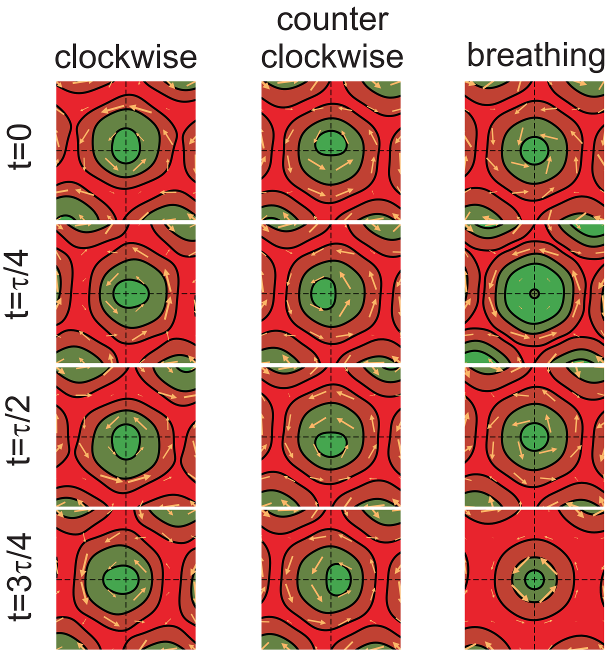

Figure 2.9.: Monte-Carlo simulation of the three excitation modes in the Skyrmion phase. We show snapshots of the different modes at different times (left side) to illustrate their evolution over time. The yellow arrows indicate the in-plane component of the magnetization [Gar13].

Within the Skyrmion lattice phase we find three magnetic resonances previously identified by Mochizuki [Moc12] as two gyration, i.e. a clockwise and counter-clockwise mode, and a single breathing mode (see Fig. 2.9).

In Fig. 2.10 we summarize all predicted excitations within the model considering a spherical sample, i.e. $N_i = 1/3$. The color in this plot indicates the field range wherein the different phases exist. The dots and their different size illustrate the theoretical expected weight of the resonances for an AC excitation field transverse to the static external field. Only the breathing mode in the Skyrmion phase is shown for a longitudinal AC field configuration because otherwise its weight vanishes.

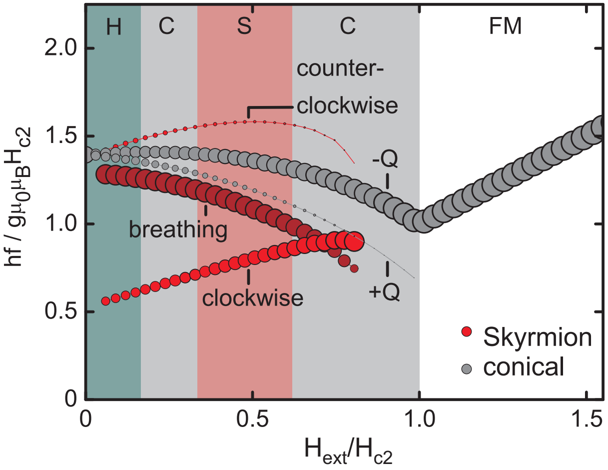

Figure 2.10.: Summary of the magnetic field dependency of the excitations predicted by the model for a spherical sample geometry, i.e. N_i = 1/3. The color code serves as a guide to where the different excitations are present. The size of the circles illustrate the excitation strength predicted by the model taken into account the excitation field of the CPW [Wai13].

2.6. Numerical Methods

2.6.1. Micromagnetic Simulations

In order to further substantiate the findings by experiments we have employed micromagnetic simulations within this thesis. We have used the MicroMagus software package [Ber08]. The software tool calculates the static magnetic configuration numerically by minimizing the total energy $\mathscr{E}_{\mathrm{tot}}$. The software takes all magnetic field contributions (besides DMI) as discussed above into account. Furthermore, by solving the equation of motion Eq. 2.26 numerically the response of the magnetic system to dynamic perturbations was obtained from the software package.

MicroMagus is a finite difference simulation software, i.e. the sample is divided into layers of nonzero volume and each layer is discretized into N pixel of volume Ω_i and magnetization $\mathbf{M}_i$ for i = 1...N. The energy contributions of each pixel is summed up to the total energy of the system. The internal field $\mathbf{H}_{\text{int},i}$ is calculated for each pixel i from $\mathbf{H}_{\text{int},i} = -\frac{\partial \mathscr{E}_{\text{tot}}}{\partial \mathbf{M}_i}$. It is then tested for every iteration if a minimum remaining torque is reached, i.e. if $\mathbf{M}_i$ aligns with $\mathbf{H}_{\text{int},i}$. If this is not the case a new magnetization configuration is calculated. The resulting ground state is used as an input for dynamic simulations.

We have employed two different simulation geometries for $k = 0$ and $k \neq 0$ as illustrated in Fig. 2.11 (a) and (b) respectively. For simulations at $k = 0$ we construct a unit cell of certain size, which is then subdivided into a number of pixel cells so that we end up with a finite simulation volume Ω. We apply 2D boundary conditions in the xy-plane. In a first step we obtain the static equilibrium state magnetization $\mathbf{M}(\mathbf{r})$ and $\mathbf{H}_\text{d}(\mathbf{r})$. A spatially uniform field pulse is then applied over the whole simulation geometry to get the response at $k = 0$. The field pulse is usually applied at the beginning of a 10 ns long time-domain dynamic simulation and $\mathbf{M}(\mathbf{r}, t)$ data is obtained. Using fast Fourier transformation (FFT) we get a spatially resolved spectral response $P(f, \mathbf{r})$. From this we obtain the spatial power plots $P(f^{'}, \mathbf{r})$ for a given frequency $f^{'}$ showing the localized spin precession for a mode at $f^{'}$ [Neu06].

For simulations of the dispersion relation we need to extend the simulation geometry in y-direction (see Fig. 2.11 (b)) so that we can apply a localized field pulse. The field pulse needs to be extended over more than one unit cell and should not end at the border of a unit cell as this causes zero signal at the Brillouin zones in k-space. Again one obtaines $\mathbf{M}(\mathbf{r}, t)$. We use spatio-temporal 2D FFT to obtain $P(f, k)$ and therefore the dispersion relation $f(k)$ [Kru06]. In Fig. 2.12 (a) we show the simulated dispersion relation for a plain film of Py with 22 nm thickness in the MSFVW geometry ($\mu_0 H$ = 1.2 T). The dashed line is the calculated dispersion using Eq. 2.42. One can see that the calculation agrees well with the simulated one. Only at large k the calculated dispersion obtained by Eq. 2.42 deviates from the more accurate curve obtained by micromagnetic simulation. Note that the experiments in this thesis are performed at much smaller wave vectors, i.e. k < 5 rad/μm. From $P(t, x)$ we also get the time dependent spin precession amplitudes. This allows us to plot snapshots of the spin precessional amplitude at different times t to illustrate propagation of spin waves. In Fig. 2.12 (b) we show those snapshots again obtained from the Py plain film simulation in MSFVW geometry. The exciting field pulse is located in the center of the simulation geometry (point-like excitation) and one can see spin waves traveling isotropically

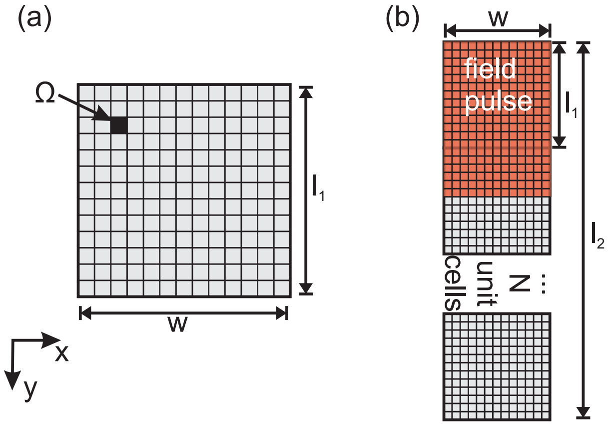

Figure 2.11.: Schematic illustration of micromagnetic simulation layouts. (a) Layout used for $k = 0$ simulations. One unit cell is used with two-dimensional periodic boundary conditions in the xy plane. The unit cell is subdivided into quadratic pixels, where one has the specific size Ω. The unit cell is excited with a homogeneous field pulse. (b) Layout used for $k \neq 0$ simulations. The unit cell is repeated N times in the y-direction. Again 2D periodic boundary conditions are applied. The field pulse is applied over the indicated area, therefore exciting spin waves with $k \neq 0$.

away from the center, which is different from in-plane field configuration [Neu11b].

2.6.2. Electromagnetic Simulations

We use the software tool $MicrowaveStudio$[1] in this work to obtain the magnetic field $\mathbf{h}(\mathbf{r})$ produced by a coplanar waveguide. Results are presented in chapter 3.3. The waveguide is discretized into simulation cells and Maxwell's equation are calculated obeying the continuity conditions of the simulation cell boundary using finite-integral-method. The software is used to obtain the current density in the inner- and outer conductor of the coplanar waveguide. The excitation ports are 50 Ω discrete ports in our simulations. From a FFT we get the corresponding excitation spec-

---

[1] CST Corp., Darmstadt, Germany

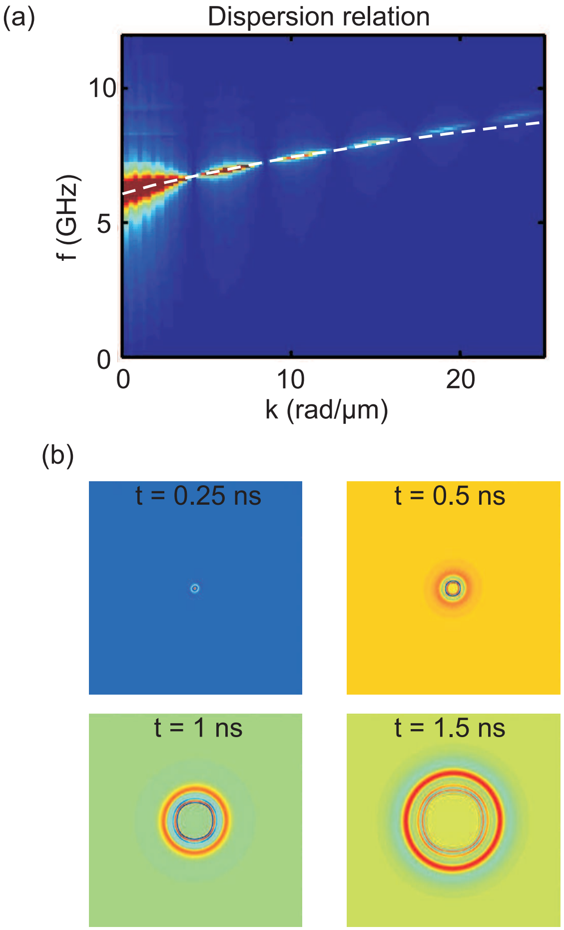

Figure 2.12.: (a) Dispersion relation as simulated by micromagnetic simulations for a 22 nm thick Py plain film with an external magnetic field of 1.2 Tesla applied in the out-of-plane direction. The white dashed line is the calculated dispersion relation using Eq. 2.42. The calculated curve only differs from the simulated curve at very high k-vectors. In (b) we show snapshots of the local spin precessional amplitude obtained by micromagnetic simulations, after a local excitation in the center of the simulation cell, illustrating the isotropic nature of the MSFVW.

trum of the coplanar waveguide, which we show in chapter 3.3. For more information on the sotware we refer to [Wei08]. In Fig. 2.13 we show a typical simulation geometry of a coplanar waveguide and the simulated field profile.

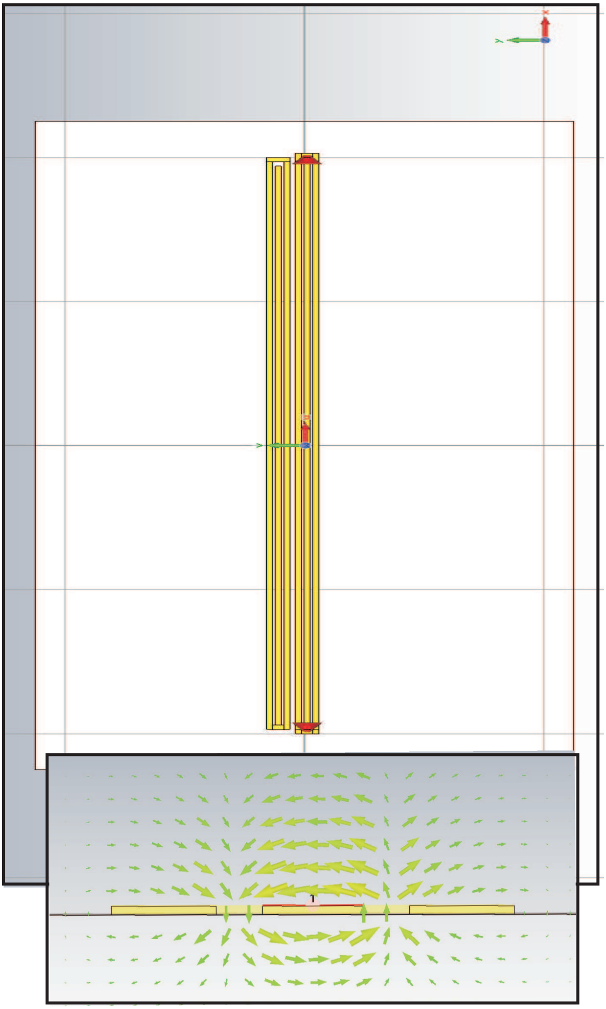

Figure 2.13.: The simulation geometry of a transmission CPW, i.e. two CPW's collinear to each other. One CPW consists of a signal line and two ground lines on either side. A cut through the CPW and the substrate shows the simulated field distribution.

3. All-Electrical Spin-Wave Spectroscopy

In the course of this work we have employed all-electrical spin-wave spectroscopy (AESWS). This technique is related to common VNA-FMR (Vector-Network-Analyzer-FMR) in that it relies on the excitation of spin-waves using CPWs in combination with a VNA. The main difference is that in AESWS one excites spin waves with a nonzero wave vector k, traveling over a certain distance d. Therefore, this technique is also known as propagating spin-wave spectroscopy [Mel01, Bai01, Bai03, Bao08]. In this chapter we present the general components of this broadband measurement technique, i.e. Lakeshore Cryogenic Probe Station CPX-VF, Vector Network Analyzer (VNA), and coplanar waveguides (CPWs). In the end of this chapter we give a detailed description of the data analysis of a ferromagnetic plain film.

3.1. Measurement Setup

In Fig. 3.1 we show an overview picture of the experimental setup and a close-up of the sample station. The main part of the experimental setup is a commercially available open flow cryogenic refrigerator (Lakeshore Cryogenic Probe Station CPX-VF), which consists of six thermally anchored microwave probe arms. However, throughout this study only two arms are used. These two arms are connected via 50 Ω microwave cables to the VNA, which is used as a microwave source and detector and is described in the next section in detail. The cryogenic microwave tips (250 μm pitch) are further connected via semirigid microwave cables. The probe tips accomplish the transition from a female K-connector to three individually spring loaded tips in a Ground-Signal-Ground geometry, which are used to connect to the corresponding pads of a coplanar waveguide. In order to enable exact positioning of the probe tips a micropositioning system is integrated in the probe arms. The inner chamber is evacuated ($p \leq 10^{-4}$ bar) and cooled using liquid helium. This enables cooling of the superconducting magnet, which gives rise to a perpendicular magnetic field of up to 2.5 T. At the same time the cooling can be used for measurements at helium temperature (4.2 K). In addition, the sample stage is connected to an automated heater system, which is used to control the temperature of the sample in the range of 4.2 K to 400 K. To avoid any environmental noise the setup is mounted on a shock absorbing table. Automated data acquisation and control software allows to run predefined measurement schemes and controls the magnetic field and the VNA.

3.2. Vector Network Analyzer and Scattering Parameter

The VNA in combination with a coplanar waveguide is used for the generation of electromagnetic waves. Here the VNA is used as a hf-source at frequencies ranging from 10 Hz to 26 GHz. The VNA supports sinusoidal voltage signals of the form:

$$V(r,t) = \tilde{V}(r)\text{exp}(iwt), \tag{3.1}$$

which are traveling through the microwave cables and the CPW. Considering that the electromagnetic propagation in a microwave circuit is mainly characterized by the series resistance R, the series inductance L as well as the shunt conductance G and the shunt capacitance C, one can derive the so-called Telegrapher's equations [Sar43]:

$$\frac{\partial^2 \tilde{V}}{\partial r^2} = \gamma^2 \tilde{V} \quad ; \quad \frac{\partial^2 \tilde{I}}{\partial r^2} = \gamma^2 \tilde{I}, \tag{3.2}$$

where γ is the propagation constant defined as:

$$\gamma = \sqrt{(R + jwL)(G + jwC)}. \tag{3.3}$$

The solutions of Eqs. 3.2 have the form:

$$\tilde{V}(r) = \tilde{V}^{+}\text{exp}(-\gamma r) + \tilde{V}^{-}\text{exp}(\gamma r) \tag{3.4}$$

$$\tilde{I}(r) = \tilde{I}^{+}\text{exp}(-\gamma r) + \tilde{I}^{-}\text{exp}(\gamma r). \tag{3.5}$$

Here $\tilde{V}^{+}$, $\tilde{I}^{+}$, $\tilde{V}^{-}$, $\tilde{I}^{-}$ are integration constants and their solutions are linear combinations of waves traveling backward and forward. The ratio

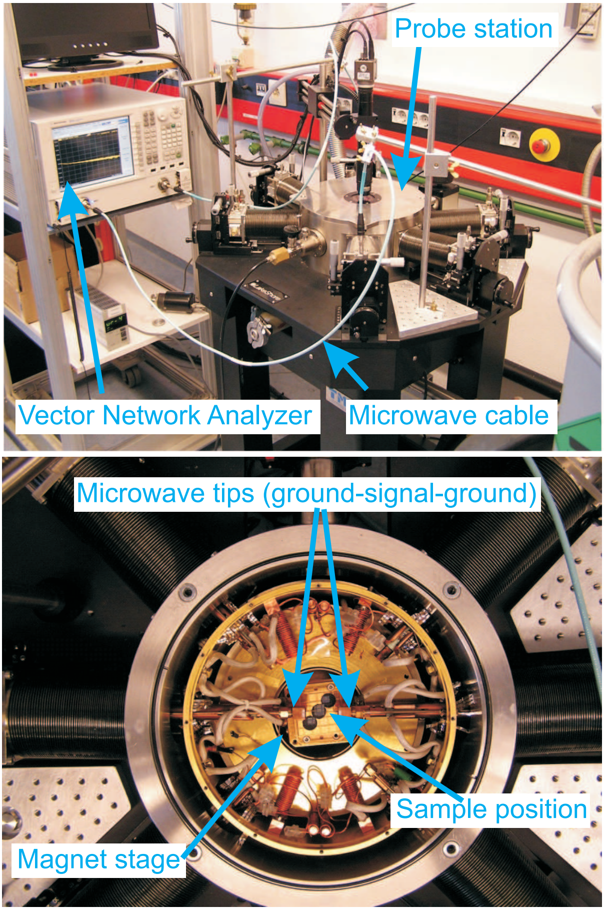

Figure 3.1.: Pictures of the Lakeshore Cryogenic Probe Station CPX-VF used within this work. The upper picture shows an overview of the setup consisting of a Vector Network Analyzer, microwave equipment like 50 Ω matched cables, and the probe stage itself with all features explained in the text. In the lower picture we show the sample stage. Two microwave probe tips are used to contact the sample. The superconducting magnet is located beneath the sample stage and supplies an external field of up to 2.5 T. The chamber is cooled with liquid helium and the sample stage can be heated to reach any temperature between 4.2 K and 400 K.

of these integration constants is called the characteristic impedance:

$$Z_\mathrm{c} = \frac{\tilde{V}^+}{\tilde{I}^+} = -\frac{\tilde{V}^-}{\tilde{I}^-} = \sqrt{\frac{(R + jwL)}{(G + jwC)}}. \tag{3.6}$$

For a more detailed dereviation we refer the interested reader to the work of Bilzer [Bil07].

For the situation of non-Transversal Electric and Magnetic fields (TEM) wave propagation the measurement of total voltage and current is not applicable. Therefore, the VNA measures S-parameters instead. We can define a scattering matrix for a microwave network with n-ports using complex normalized waves a_n and b_n as follows:

$$a_n = \frac{V_n + Z_{\mathrm{c}n} I_n}{2\sqrt{Z_{\mathrm{c}n}}} \quad ; \quad b_n = \frac{V_n - Z_{\mathrm{c}n} I_n}{2\sqrt{Z_{\mathrm{c}n}}}. \tag{3.7}$$

Now we can calculate the voltage V_n and the current I_n at port n using:

$$V_n = \sqrt{Z_{\mathrm{c}n}}(a_n + b_n) \quad ; \quad I_n = \frac{a_n - b_n}{\sqrt{Z_{\mathrm{c}n}}}. \tag{3.8}$$

Inserting Eqs. 3.4 and 3.5 into Eq. 3.7, one can see that a_n describes the incoming wave, whereas b_n is the outgoing wave:

$$a_n = \frac{V_n^+}{Z_{\mathrm{c}n}} \mathrm{exp}(-\gamma r) \quad ; \quad b_n = \frac{V_n^-}{Z_{\mathrm{c}n}} \mathrm{exp}(\gamma r). \tag{3.9}$$

In Fig. 3.2 the relation between $a_{1,2}$, $b_{1,2}$, and the S-paramters is sketched. For our case of a 2-port, i.e. $n = 2$, device we need n^2, i.e. four S-parameters, which completely describe our network:

$$\begin{pmatrix} b_1 \\ b_2 \end{pmatrix} = \begin{pmatrix} S_{11} & S_{21} \\ S_{12} & S_{22} \end{pmatrix} \begin{pmatrix} a_1 \\ a_2 \end{pmatrix} \tag{3.10}$$

This is called the scattering matrix and each S_{nm} is the ratio of the outgoing wave b_n at port n to the incoming wave a_m at port m. At this point we want to emphasise that the S-parameters are complex values and the measured quantities are therefore phase sensitive. We will see later that this enables us to evaluate the group velocity of propagating spin-waves.

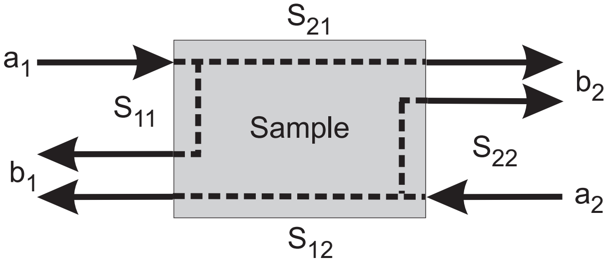

Figure 3.2.: Illustration of the microwave network and the relation between the ports ($a_{1,2}$, $b_{1,2}$) and the scattering parameters S_{ij}.

In order to cancel out any errors introduced by the cables, probe tips, connections, and inaccuracies in the hardware of the VNA we use a calibration routine. This shifts the reference plane to the end of the probe tips and the measured signal only depends on the circuit in between. We are using the calibration substrate CS-5 of $GGB\ industries$ and the routine OSLT (Open, Short, Load, Through), which is designed for ground-signal-ground probe tips with a pitch of up to 250 μm. The calibration substrate has well defined standards, which are an open-circuit, short section, a precise 50 Ω impedance and a coplanar waveguide of defined length. Each standard has to be connected with the probe tips and measured in both directions in order to get a full error correction.

3.3. Coplanar Waveguides

Coplanar waveguides (Fig. 2.13) are key to our measurement technique as they provoke defined spin precession in the material under test. It is of utmost importance to understand and model the excitation characteristics of the CPWs. We have used two different CPW designs within this work, which can be seen in Fig. 3.3 (a) and (b). The rf-current from the VNA creates an oscillating field h_{rf} (Fig. 3.3 (c)) according to Biot-Savart's law. This field causes spin precession in the magnetic material close to the CPW. The reverse effect is then used to detect any spin precessional motion. In Fig. 3.3 (a) we show a so-called flip-chip design, where the sample is placed on top of the CPW. In Fig. 3.3 (b) we show two CPWs, which are prepared collinear to each other, in order to excite spin waves with one

CPW (CPW1) and receive the propagated signal using the second CPW (CPW2). The k-vector distribution depends on the geometrical parameters of the CPW. The first CPW design (Fig. 3.3 (a)) has an inner conductor width (w_{ic}) and an outer conductor width (w_{oc}) of 20 μm as well as a gap between inner and outer conductor (w_{gap}) of 11 μm. The second CPW geometry (Fig. 3.3 (b)) has w_{ic} = 2.4 μm, w_{oc} = 2.4 μm, and w_{gap} = 1.1 μm. The distance d between the inner conductors of CPW1 and CPW2 is 12 μm. Using electromagnetic simulations ($MicrowaveStudio$) we obtain the component of the dynamic magnetic field h_x as depicted in Fig. 3.4 (a) and (c). In Fig. 3.4 (a) one can clearly observe the skin effect, i.e. the tendency of an alternating electric current to become distributed inhomogeneously within a conductor, such that the current density is largest near the edge of the conductor. In Fig. 3.4 (c) we have also plotted the z-component of the dynamic field h_z. We find that the values differ by an order of magnitude, which is why we neglect h_z for the further analysis. Next we use Fast-Fourier-Transformation of h_x to get the excitation spectra of the CPWs. The result can be seen in Fig. 3.4 (b) and (d). We have labeled the first and second most prominent k excitation as well as Δk (full width at half maximum) for k_1. The parameter Δk, i.e. the distribution of excitation vectors k, leads to inhomogeneous line broadening in the measured resonance signal [Bil07]. In addition we want to point out that people have used approximations of the spatial field, where they have used rectangular field profiles [Cou04, Ken07, Neu11b]. Although this might be a good approximation for CPWs having a small inner conductor width, e.g. w_{ic} = 2.4 μm, for CPWs having an inner conductor width of 20 μm the skin effect causes a large deviation from the approximated rectangular profile and is therefore not able to reproduce the excitation profile in a good manner. If we compare the k_1-vector obtained by FFT using a rectangular function with the value obtained by the exact function from simulations we get an absolute error of 12$\%$ (42$\%$) for w_{ic} = 2.4 μm (w_{ic} = 20 μm). This emphasizes the importance of our analysis, especially for the case of wide CPWs. In general, spin precession is excited by the current through the CPW and a voltage can be induced in the CPW vice versa. Following an approach by [Gie05, Sil99] the flux in a CPW Φ_{CPW} caused by a magnetic sample of magnetization **M** is

$$\Phi_{\text{CPW}} = \mu_0 \int_V \frac{\mathbf{h}_{\text{CPW}}}{I} \cdot \mathbf{M} \mathrm{d}V, \tag{3.11}$$

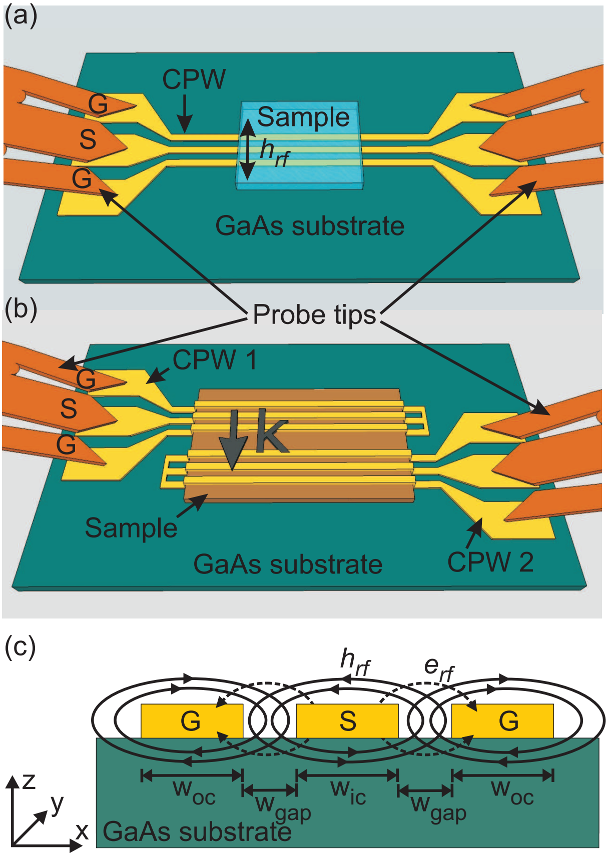

Figure 3.3.: (a) Sketch of the experimental setup in a flip-chip configuration, where the sample is placed on top of the CPW. The microwave tips are in contact with the contact pads of the CPW to feed the rf-current through. The h_{rf}-field is generated in the CPW and excites spin waves in the sample under test. (b) Sketch of integrated CPWs lithographicaly prepared on top of the sample for propagation measurements. The spin wave is excitated at one CPW and the propagated signal is then detected using the other CPW being collinear to the first one. (c) Cut through the substrate and the CPW on top. The h_{rf}-field (solid lines) is shown as well as the e_{rf} field (dashed lines).

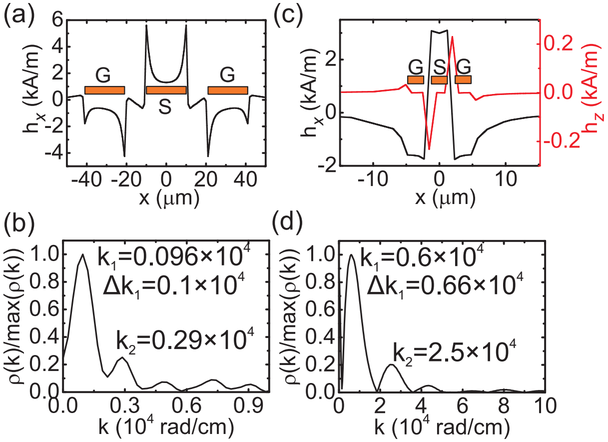

Figure 3.4.: CST MicrowaveStudio is used to simulate the dynamic magnetic field h_x for a CPW with a 20 μm wide signal line (a) and a 2.4 μm wide signal line (c). In addition we show the out-of-plane component (red curve in (c)), i.e. h_z, for the smaller CPW which is much smaller if compared to the in-plane component. Through a fast Fourier transformation of h_x we obtain the k-vector distribution for the 20 μm wide signal line CPW (b) and the 2.4 μm wide signal line CPW (d).

where V is the volume of the sample, $\mathbf{h}_{\text{CPW}}$ is the field created by the CPW, and I is the current through the CPW. In a transmission experiment with two CPWs, one CPW (CPW1) is used as the excitation port and a second CPW (CPW2) as the receiving port, but note that excitation and detection can also be done using just one CPW (reflection configuration). Again neglecting out-of-plane contributions we define the magnetic flux at CPW2 as:

$$\Phi_2 = \mu_0 \int_V \frac{\mathbf{h}_2}{I_2} \cdot \mathbf{M} \mathrm{d}V, \tag{3.12}$$

where $\mathbf{h}_2$ is the magnetic field along the x-direction of CPW 2 defined by the current I_2 and the width of the inner conductor line w_{ic}:

$$\mathbf{h}_2 = \frac{I_2}{w_{\text{ic}}} f(x) \mathrm{e}_x. \tag{3.13}$$

Here $f(x)$ is a normalized spatial distribution function of $\mathbf{h}_{2,x}$. It follows that

$$\Phi_2 = \frac{\mu_0 tl \sin\delta}{w_{\mathrm{ic}}} \int \mathrm{d}x (f(x) M_x(x,t)), \tag{3.14}$$

where δ is the angle between the magnetization and the x-axis, l is the length of the inner conductor and t is the thickness of the magnetic material. From this one can calculate the induced voltage V_2 at the receiver CPW by

$$V_2 = \frac{\mathrm{d}\Phi_2}{\mathrm{d}t} = -\frac{\chi(\omega)\mu_0 tl \sin\delta}{w_{\mathrm{ic}}} \int \mathrm{d}x f(x) \frac{dh_{2,x}(x,t)}{\mathrm{d}t}. \tag{3.15}$$

We want to point out that here $\chi(\omega)$ is the susceptibility of all contributing spin waves [Vla10] and reads:

$$\chi(\omega) = \int \mathrm{d}k \chi'(\omega,k)\rho(k)\mathrm{exp}(-ikd). \tag{3.16}$$

$\rho(k)$ is the efficiency of excitation for a given k, the exponential decay takes the attenuation of spin waves over the distance d into account.

We also want to mention that spin waves excited by CPW1 are not only excited directly underneath the conductor lines but also in their close vicinity and to a small amount underneath the receiving CPW2. This effect leads to direct crosstalk and it should be evaluated for different CPW geometries as the influence of this effect on the measured data depends on the distance d between the CPWs and the geometrical parameters of the conductor lines. The CPWs used in this work have been studied extensively in Ref. [Neu11b] and electromagnetic crosstalk was found to be small.

3.4. Full 2-port Data Analysis

Here we demonstrate typical data analysis as used within this work. We use a sputtered CoFeB plain film in order to describe all aspects of data evaluation. The thickness of the film is 41 nm. The preparation of such a film is described in the next chapter. We are using the propagating CPW design with w_{ic} = 2.4 μm in order to make full use of AESWS. As described before we are extracting S-parameters ($S(f,H)_{ij}$) from the VNA, where i and j denote the ports. Here i is always the receiving port and j is

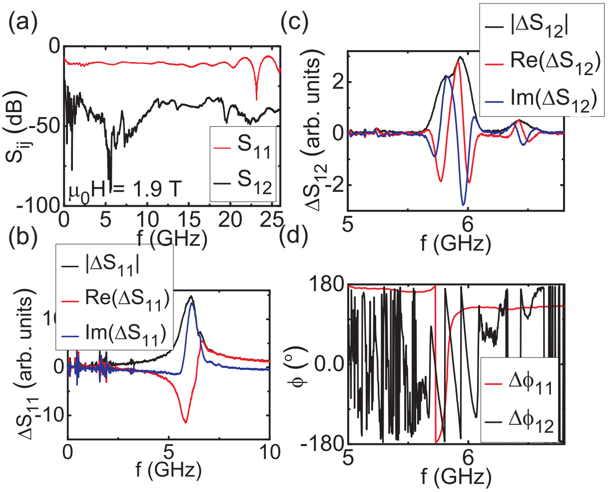

Figure 3.5.: Raw measurment signals of S_{ij} at an external field of $\mu_0 H$ = 1.9 T as obtained by the VNA (a). In order to observe the ferromagnetic resonance we employ a difference technique as explained in the text. From this we obtain the magnitude, the real and the imaginary part of the scattering parameters (b). The oscillatory signal in a propagation measurement, i.e. using two seperate CPWs to excite and detect, is shown in (c). In addition, we show the transmission and reflection signal of the phase (d).

the exciting port. If just one port is used we write $i = j$. During the measurement we sweep the frequency, while the external field is held constant. Usually this is repeated for several values of external field in order to get the field dependency of the resonance frequency. In Fig. 3.5 (a) we show the measured signal at an external field of 1.9 T. The signal is shown in dB and is defined as:

$$S_{ij} = 20\log(S_{ij}) = 20\log\left(\frac{b_i}{a_j}\right). \tag{3.17}$$

The curves in Fig. 3.5 (a) thus reflect the electromagnetic response of the CPW. From the small values of S_{12} we see that CPW1 is well isolated from CPW2. In order to observe the resonance frequency, i.e. the response of the magnetic material, we need to enhance the signal-to-noise ratio. This is done by a difference method. By taking a reference measurement at a different field (reference field) S_{Ref} than the actual measurement S_{Meas} we obtain a difference signal as:

$$\Delta S = S_{\mathrm{Meas}} - S_{\mathrm{Ref}}. \tag{3.18}$$

Preferably we take a reference signal at a high external field, where the resonance is above the 26 GHz measured by the VNA, so that the signal does not interfere with our actual measurement signal. Sometimes this is not possible because the field strength available at the setup is not enough to push the frequency out of the range of the VNA (depends on the material under test). In this case we take the reference measurement at a field where the resonance is as far away as possible from the measured signal, always assuring that no overlap of the two resonances occurs. The obtained data set can be seen in Fig. 3.5 (b), where we show the magnitude signal as well as the real- and imaginary part. The main resonance is clearly visible at 6.1 GHz as well as a second maximum on the right shoulder of the main peak at around 6.6 GHz. The second peak can be assigned to the second excitation maxima k_2 of the CPW (c.f. Fig. 3.4 (d)).

In Fig. 3.5 (c) we plot the transmission signal ΔS_{12}, i.e. spin waves are excited at CPW2 and the signal of propagated spin waves are picked up using CPW1 at a distance d. We observe two signals, which stem from the already mentioned excitations at k_1 and k_2. The mere fact that the excitation spectra of a CPW has a finite width Δk produces the oscillatory signal in the real- and imaginary part of ΔS_{12} [Bai01, Bai03, Bao08]. This is due to the fact that the phase of the spin wave depends on the wave vector k:

$$\phi = kd. \tag{3.19}$$

The VNA measures the change of phase $\Delta\phi$ for changing frequency Δf, i.e. a variation in f and thus in k as mentioned above. From this it is possible to extract a group velocity, which is given by:

$$v_{\mathrm{g}} = \frac{\partial \omega}{\partial k} = 2\pi d \left(\frac{\Delta f}{\Delta \phi} \right). \tag{3.20}$$

For the evaluation of v_{g} we extract the frequency difference from two maxima of the oscillations, which are $\Delta\phi = 2\pi$ apart. This means Eq. 3.20

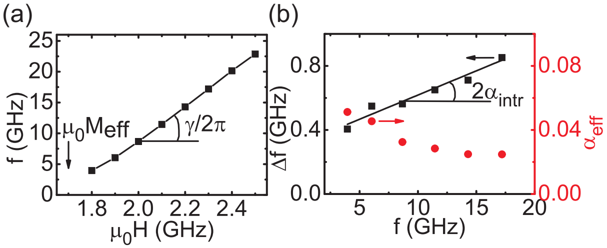

Figure 3.6.: Resonance frequencies as a function of external field applied in the out-of-plane direction (a). Linewidth Δf and effective damping parameter α_{eff} plotted over frequency (b). In a MSFVW thin film experiment we are able to extract the intrinsic damping parameter α_{intr} from the slope.

becomes:

$$v_{\text{g}} = \Delta f d. \tag{3.21}$$

Identical to this method one can also evaluate the above mentioned phase shift by looking directly at the phase data ϕ (Fig. 3.5 (d)). Using Eq. 3.20 it is also possible to read out the group velocity from the data of $\Delta\phi_{12}$. Although this method is not used within this work we are showing it as this is a more traditional way of evaluating the group velocity. If we analyze the group velocity from ΔS_{12} and from $\Delta\phi_{12}$ we obtain v_{g} = 2.9 km/s in both cases, showing the equivalence of the two methods. In addition, we have plotted $\Delta\phi_{11}$, where we see a change by 180° at the resonance frequency, as expected from a harmonic oscillator.

Finally, we show the field dependency of the resonance frequency in Fig. 3.6 (a). As expected from Eq. 2.33 the frequency is a linear function of the external field for fields higher than $\mu_0 M_{\text{eff}}$, i.e. the magnetization is pointing in the out-of-plane direction (MSFVW configuration). In this case we determine $\mu_0 M_{\text{eff}}$ to be 1.7 Tesla. From Eq. 2.33 we see that the slope is given by $\gamma/2\pi$ = 28.7 GHz/T, which is equivalent to a g-factor of g = 2.0.

To complete the data analysis we evaluate the linewidth Δf of the imaginary part of ΔS_{11} at different fields (Fig. 3.6 (b)). This can be seen as an effective linewidth where extrinsic and intrinsic contributions add up. Assuming uniform precession in an infinite medium the linewidth connects to the damping parameter α as:

$$\Delta\omega_{\text{eff}} = 2\alpha_{\text{eff}}\omega, \tag{3.22}$$

where we have used the subscript ”eff” to relate to the measured effective linewidth. The effective damping parameter α_{eff} is plotted in Fig. 3.6 (b). For an AESWS experiment Vlaminck et al. [Vla10] have proposed that the effective linewidth consists of mainly two parts. One being the intrinsic contribution $\Delta\omega_{\text{intr}} = 2\alpha_{\text{intr}}\omega$ and the other one being the extrinsic contribution mainly caused by the non-monochromatic excitation of the CPW, i.e. $\Delta\omega_{\text{extr}} = v_{\text{g}}\Delta k$. If one can add these two contributions to one another one obtains:

$$\Delta\omega_{\text{eff}} = 2\alpha_{\text{intr}}\omega + v_{\text{g}}\Delta k. \tag{3.23}$$

From this we can extract the intrinsic damping parameter α_{intr} by plotting Δf_{eff} over the resonance frequency (Fig. 3.6 (b)). From the slope we obtain α_{intr} = 0.015[1]. Finally, we want to give an expression for the attenuation length L_{att} over which the precession angle decays as $1/e$. Following Vlaminck et al. [Vla10] the attenuation length is given by:

$$L_{\text{att}} = v_{\text{g}} \cdot \tau, \tag{3.24}$$

where $\tau = 1/(\alpha_{\text{intr}}\omega)$ is the exponential time decay. The attenuation length is helpful to determine how far a spin wave travels before the precessional cone angle decays as $1/e$.

Another way of evaluating the attenuation length is the use of the measured S-paramters in a transmission measurement. The S-paramters are connected to the attenuation length through [Hub13]:

$$\Delta S_{21} = \beta\Delta S_{11}\text{exp}\left(-d/L_{\text{att}}\right), \tag{3.25}$$

$$\Delta S_{12} = \left(1-\beta\right)\Delta S_{22}\text{exp}\left(-d/L_{\text{att}}\right), \tag{3.26}$$

---

[1] Note that this film was prepared before optimization of the sputtering process using Argon plasma. In chapter 5.1 we investigate the damping of a CoFeB thin film after process optimization by using Xenon plasma and we find α_{intr} = 0.008.

where β is a non-reciprocity parameter defined as:

$$\beta = \frac{\frac{\Delta S_{21}}{\Delta S_{11}}}{\frac{\Delta S_{21}}{\Delta S_{11}} + \frac{\Delta S_{12}}{\Delta S_{22}}}. \tag{3.27}$$

For reciprocal characteristics β takes a value of 0.5.

4. Sample Preparation

In this chapter we describe sample preparation of CPWs by optical lithography as well as the preparation of Antidots (ADs) using focused ion beam (FIB) technique. Semi-insulating GaAs [001] of 350 μm thickness is used as a substrate[1]. Other material systems investigated in this work have not been prepared by the author; therefore, only a brief description will be given at the beginning of the respective chapters with references to more detailed work on the fabrication processes from the groups responsible for the synthesis.

4.1. Samples with Integrated Coplanar Waveguides

Here we want to give an overview of the process steps involved in the preparation of plain films and Antidot lattices (ADL) with integrated CPWs. For this we use optical lithography and focused ion beam (FIB) technique. After cleaning the substrate with propan-2-ol, 2-propanone and drying with dry Nitrogen the samples are processed as follows:

(I) Using commercial spin coaters a first layer of resist (LOR-3A[2]) is spun onto the sample at 4500 rpm for 60 s. Followed by a baking step at 180°C for another 60 s. A second resist (S1813 G2[3]) is spun on top of the first one at 6000 rpm for 40 s. A baking step at 115°C for 60 s follows. The two-step process is used to achieve an undercut, which makes the lift-off process in the end easier.

(II) Next we use optical lithography to define a mesa of 200 x 75 μm in size. We use a mask aligner MJB-3[4] with a 350 W Hg lamp in combination with a chrome mask, which contains the desired mesa. The mask was produced by the Walther-Schottky-Institut of TUM

---

[1] Freiberger Compound Materials GmbH, Freiberg, Germany

[2] MicroChem Corp., Newton, MA, USA

[3] Rohm and Haas Company, Philadelphia, PA, USA

[4] Süss MicroTec AG, Garching b. München, Germany

using a laser writer. The sample is put in physical contact with the mask so the UV-light can expose the resist within the mesa defined by the mask. The time of exposure was set to 3.6 s.

(III) The structure is now developed using MF-26A developer[1] for 30 s, where the resist of the exposed area is solved.

(IV) Deposition of the desired material. For Py we use physical vapor deposition (PVD) by electron beam heating. The deposition is performed in a high vacuum chamber under 10^{-7} mbar. For CoFeB we use RF magnetron sputtering technique in Argon or Xenon gas plasma[2]. The material is ejected from a $Co_{20}Fe_{60}B_{20}$ target and deposited onto the sample. Again the process is perfomed in high vaccuum at a base pressure of 10^{-7}, whereas during the sputter process the pressure is 10^{-3}.

(V) Lift-off processing in order to remove material on top of the resist is done using remover 1165[3]. The sample is left in the remover for at least one hour at a temperature of 55°C. Afterwards we are left with a mesa of magnetic material, i.e. a plain film.

(VI) For the preparation of ADs we are using FIB to create periodic holes in the plain film. In our case we use a cross beam system combining a scanning electron microscope (SEM) and a FIB NVision-40[4]. In order to align the samples we use an automated manual mark scan method using ElphyQuantum software[5]. The same software is then used to create periodic holes by a dot exposure of the FIB. For holes with a 190 nm (120 nm) diameter in CoFeB (Py) we use a current of 80 pA and an exposure time of 21 ms.

(VII) Before the preparation of integrated CPWs we use atomic layer deposition (ALD) of Al_2O_3 in order to isolate the structure from the CPWs. The isolation layer is optimized and set to a thickness of 5

---

[1] Rohm and Haas Company, Philadelphia, PA, USA

[2] We have used Argon gas plasma in the beginning, but we found that Xenon leads to a better film quality and smaller ferromagnetic linewidth.

[3] Rohm and Haas Company, Philadelphia, PA, USA

[4] Carl Zeiss NTS Corp., Oberkochen, Germany

[5] Raith Corp., Dortmund, Germany

nm. The temperature in the ALD chamber is set to 100°C during the deposition.

(VIII) In order to prepare CPWs directly on top of the as-prepared structure we employ again optical lithography processing to define the CPW structure in the same manner as described in steps I-III. Followed by material deposition using electron beam heating. First we deposit 4.5 nm of chromium in order to establish adhesion. Secondly we deposit 120 nm of Au. The pressure during evaporation is again around 10^{-7} mbar.

(IX) Finally, we perform one more lift-off process step (see V) to be left with the CPW structure.

In Fig. 4.1 we show an SEM image of an AD sample with integrated CPW prepared as described above. In this case the CPW is a transmission type CPW, i.e. two CPW stuctures collinear to each other, with inner conductor width of 2.4 μm and a seperation of 12 μm (c.f. chapter 3.3).

4.2. Preparation of Flip-Chip Waveguides

In some of our studies we have employed so-called flip-chip measurements, where we put the material under test on top of the CPW. The CPWs are prepared as described above using optical lithography and lift-off processing. The CPWs can be of different geometries as mentioned in chapter 3.3. This way we have control over the excited wave vector distribution. As we are working with samples of different sizes the length of the conductor line is varied according to the sample size, i.e. some are of 9 mm length and some are prepared to be 400 μm in length.

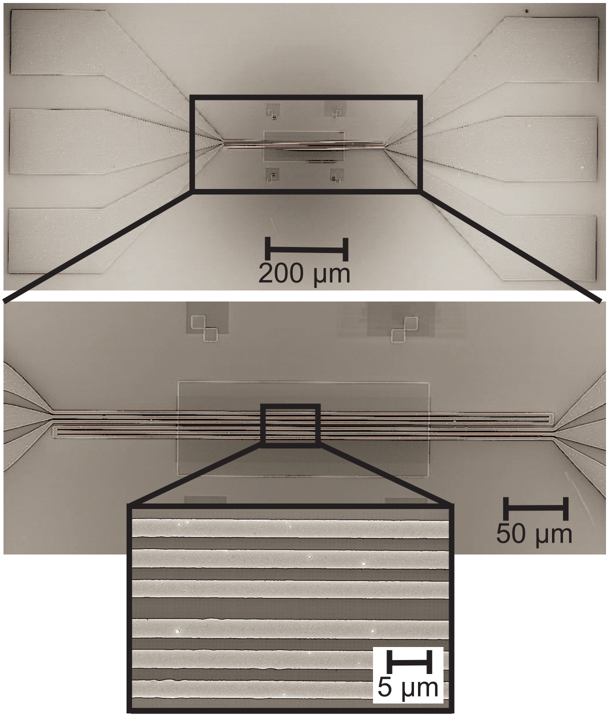

Figure 4.1.: SEM image of an integrated transmission CPW, i.e. two CPW's collinear to each other lithographically prepared on top of a thin film mesa. The signal and ground lines are 2.4 μm wide and the gap between the signal and ground lines is 1.1 μm. The separation between the inner signal line of them is 12 μm, which is the distance a spin wave travels in an AESWS experiment.

5. Materials for MSFVW-based Devices

In this chapter we study different materials for their suitability for experiments with out-of-plane magnetic fields, i.e. MSFVW configuration. As the out-of-plane geometry has not been the subject of many studies in thin-film materials, there is also a lack of material considerations for this particular configuration. We start from evaporated Py, as this is a widely used material in magnetoelectronics and magnonics research. Next, we investigate sputtered CoFeB (the exact composition of the target is: $\mathrm{Co_{20}Fe_{60}B_{20}}$) because low damping and large group velocities on this composition have been reported recently [Yu12]. Both materials are deposited onto semi-insulating Gallium Arsenide substrates by optical lithography and lift-off processing. CPW's with an inner conductor width ω_{ic} = 2.4 μm and a signal-to-ground separation ω_{io} = 1.1 μm (c.f. chapter 3.3) have been prepared on both samples. In order to compare their dynamic properties, both films have been prepared with the same thickness of t = 20 nm. Large out-of-plane fields are used to magnetize these films accordingly. Finally, we consider so called perpendicular magnetic anisotropy (PMA) samples, i.e. ultra thin Co/Ni-multilayers. These materials are interesting as they exhibit a perpendicular magnetization even at zero external field. Furthermore, PMA has been used in spin-torque oscillators [Mad11] to excite coherent spin waves. Therefore, the dynamic properties of PMA are of utmost interest for future integrated spin-torque oscillator spin-wave devices [Nal13]. The PMA samples have been prepared at the University of Stockholm by the group of Prof. Johan Åkerman.

5.1. Permalloy and CoFeB thin films

We start our measurements with the Py plain film. In Fig. 5.1 (a) we show a gray scale plot of ΔS_{11} of the 20 nm thick Py film with field steps of 100 mT. The dark contrast reflects absorption of the microwave signal due to resonant precessing spins. We divide the gray scale plot into two characteristic regions (indicated by a white dashed line in Fig. 5.1 (a)). In region I the external magnetic field is not strong enough to align all spins against the shape anisotropy into the out-of-plane direction. This is the so-called ”not-aligned” mode of spin precession. At the local minima at around $\mu_0 H$ = 1.0 T, the external magnetic field is just as high as the anisotropy field that stems from the shape anisotropy of the sample. From there on, the spins are aligned with the external field and the curve follows a linear dependency. In theory, the local minima should be at zero frequency, but due to a small in-plane component of the external magnetic field at the position of the sample or unintentional film roughness, this resonance is shifted to a finite frequency. The blue dashed line is a fit to the measured data in order to obtain the saturation magnetization using Eq. 2.42, assuming that anisotropies are not relevant, i.e. $M_{\text{eff}} = M_{\text{s}}$. From this we extract a saturation magnetization M_{s} = 820 kA/m, which is in good agreement with values reported in literature[Mar10, Neu11b].

A typical line plot of the imaginary part of ΔS_{11} at $\mu_0 H$ = 1.3 T is shown in Fig. 5.1 (b). Fitting a Lorentzian curve, we extract a linewidth of Δf = 0.23 GHz and a resonance frequency of f_{res} = 7.5 GHz. From the oscillations in ΔS_{21} (Fig. 5.1 (c)) we get a group velocity of v_{g} = 1.0 ± 0.3 km/s. This is consistent with the group velocity of v_{g} = 0.9 km/s calculated from the slope of the dispersion using Eq. 2.42 at the main CPW excitation peak k = 0.6 $\times$ 10^4 rad/cm. Using $v_{\text{g}} \cdot \Delta k$ = 0.66 $\times$ 10^9 rad/s (Δk = 0.66 $\times$ 10^4 rad/cm from simulations in chapter 3.3) together with Eq. 3.23 we calculate the intrinsic Gilbert damping to be α_{intr} = 0.008 (f_{res} = 7.5 GHz).

It is now instructive to compare these values with sputtered CoFeB. In Fig. 5.1 (d) we show a gray scale plot together with a fit (blue dashed line) for 20 nm thick CoFeB using equation 2.42. Note that the sample was not aligned perfectly in the center of the sample stage and a non-zero in-plane component of the external field caused a large frequency at the field position where the magnetization turns out-of-plane. By fitting a straight line to the high field data we obtain M_{eff} = 1083 kA/m. From the lineplot of the imaginary part of ΔS_{11} at $\mu_0 H$ = 1.6 T (Fig. 5.1 (e)) we extract a linewidth Δf = 0.3 GHz and a resonance frequency of f_{res} = 8.6 GHz. In Fig. 5.1 (f) we show the oscillatory signal ΔS_{21} and extract a group velocity of v_{g} = 1.6 ± 0.2 km/s. This is in good agreement with the calculated value from the slope of the dispersion relation (Eq. 2.42), where we get v_{g} = 1.4 km/s. Considering an extrinsic contribution as before for Py we calculate an intrinsic Gilbert damping of α_{intr} = 0.008 for CoFeB, which is in very good agreement with values reported in Ref. [Bil07].

Another way of extracting the intrinsic Gilbert damping is to plot the linewidth over the frequency (Fig. 5.2 (a)) [Vla10]. Using equation 3.23 we extract α_{intr} from the slope of the curve. From this we get α_{intr} = 0.0084, which is in perfect agreement with the value obtained above using $v_{\text{g}}\Delta k$ as the extrinsic contribution. Please note that this value of α_{intr} is even smaller than the value obtained in chapter 3.4. The film investigated here was prepared after optimization of the sputtering process and changing from Argon to Xenon plasma, which led to an improved film quality and a smaller linewidth in the experiment. Considering that the Xenon ions have a shorter mean free path, we assume that the reason for the improvement on the linewidth is connected to less impurities in the Xenon sputtered films. In order to extract the saturation magnetization for CoFeB we have to consider an out-of-plane anisotropy (c.f. chapter 2.2). Therefore CoFeB films with different thickness, 62.5 nm, 36 nm, and 20 nm have been prepared. From the field dependent FMR and fitting the effective magnetization we get M_{eff} = 1329 kA/m, M_{eff} = 1256 kA/m, and M_{eff} = 1083 kA/m respectively. Using Eq. 2.30 and plotting M_{eff} over $1/d$ (Fig. 5.2 (b)) we extract the saturation magnetization (M_s = 1440 ± 20 kA/m) from the intersect with the y-axis. This value is close to the saturation magentization of bulk $\text{Co}_{72}\text{Fe}_{18}\text{B}_{10}$, which is $M_{\text{s}}^{\text{bulk}}$ = 1430 kA/m [Bil07]. From the slope A, we calculate the out-of-plane anisotropy constant to $K_{\perp} = -A/2 \cdot \mu_0 M_{\text{s}}$ = 6.23 ± 0.25 mJ/m^2. Considering the thickness t = 20 nm we obtain K_1 = $K_{\perp}/t$ = 3.12 $\cdot 10^5$ J/m^3.

Another important quantity to know is the attenuation length L_{att} (c.f. Eq. 3.24). For Py we obtain L_{att} = 2.7 μm at f_{res} = 7.5 GHz. For CoFeB we obtain L_{att} = 3.6 μm at f_{res} = 8.6 GHz for MSFVW. In Ref. [Vla10] L_{att} of around 2.8 μm has been reported for 20 nm thick Py in a MSFVW experiment. In comparison, the propagation length in a 20 nm thick Py film with in-plane magnetization, i.e. Damon-Eshbach modes, is L_{att} = 7.4 μm at f_{res} = 7.5 GHz due to faster spin-wave propagation.

5.2. Films with Perpendicular Magnetic Anisotropy

The first observation of PMA in [Co/Ni] multilayers was presented by Daalderop et al. [Daa92] in 1992. Through interface effects these multilayer structures favor a perpendicular anisotropy and have been extensively studied over the past years [Blo92, Bea09, Miz11, Mac12, Hae13].

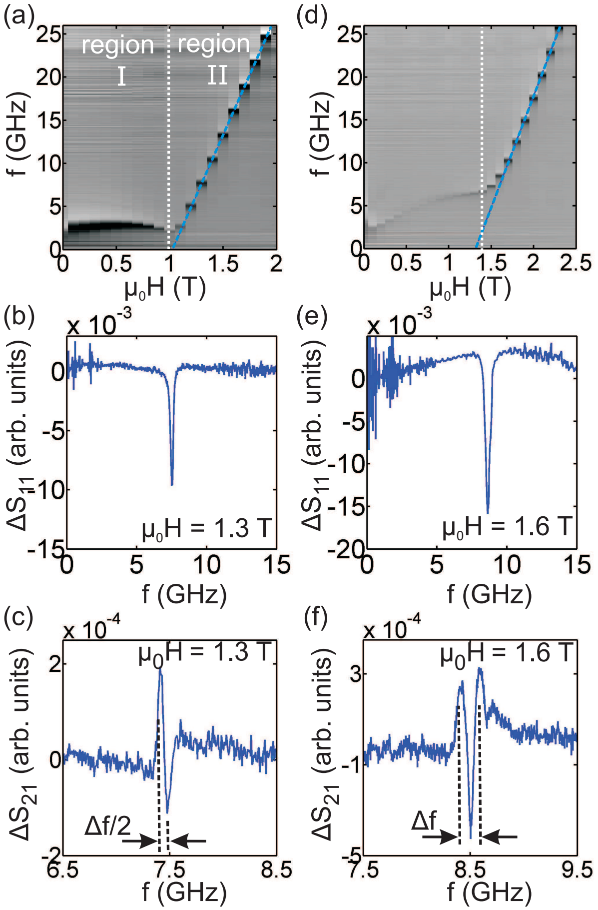

Figure 5.1.: Comparison of Py (a-c) and CoFeB (d-f) plain film measurements. Gray scale plots for Py and CoFeB are shown in (a) and (d) respectively, where dark color indicates absorption of the microwave signals. Lineplots at a fixed external field of 1.3 T (b) and 1.6 T (e) of the reflected signal ΔS_{11}. Propagation signals ΔS_{21} in order to extract the group velocity are shown for Py (c) and CoFeB (f).

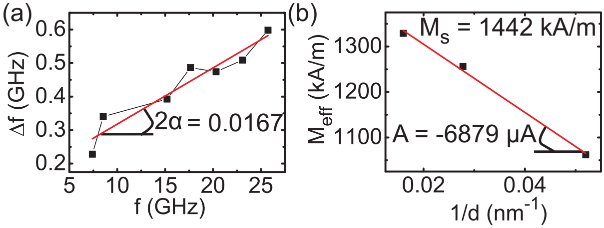

Figure 5.2.: (a) Linewidth Δf plotted over the resonance frequency in order to extract the intrinsic Gilbert damping α. (b) Determination of the saturation magnetization of CoFeB by evaluating the effective magnetization M_{eff} for different film thicknesses.

The driving force for these studies is to use PMA multilayers in spin-valve devices and spin-torque oscillators [Mad11, Moh12]. Here, we present measurements and evaluate the feasibility to use PMA for magnonic devices with out-of-plane magnetization at $\mu_0 H$ = 0 T. The exact composition of the PMA sample under investigation is:

Ta5/Cu15/Ta2/Cu10/Co0.35/[Ni0.9-Co0.35]×15/Ta5,

where the numbers behind materials indicate the thickness t of the respective layer in nm. The saturation magnetization for such multilayers can be approximated by [Blo92]:

$$\mu_0 M_{\mathrm{s}} D = \mu_0 M_{\mathrm{s}}^{\mathrm{Co}} t_{\mathrm{Co}} + \mu_0 M_{\mathrm{s}}^{\mathrm{Ni}} t_{\mathrm{Ni}}, \tag{5.1}$$

where D is the overall thickness of the multilayer stack, $\mu_0 M_{\mathrm{s}}^{\mathrm{Co}}$ = 1.79 T (t_{Co}) and $\mu_0 M_{\mathrm{s}}^{\mathrm{Ni}}$ = 0.61 T (t_{Ni}) is the saturation magnetization (thickness) for Co and Ni respectively. In our case the saturation magnetization is therefore M_{s} = 760 kA/m (Ta and Cu are not considered for M_{s}).

In Fig. 5.3 (a) we show spectra measured in a flip chip geometry as a function of external magnetic field in steps of 20 mT. The resonance at zero field lies at 11.5 GHz and increases linearly with increasing positive field, i.e. $\mathrm{d}f/\mathrm{d}H$ = const. Going to negative fields we observe a resonance of the identical slope $\mathrm{d}f/\mathrm{d}H$ for $\mu_0 H \geq$ -0.02 T. For -0.12 T < $\mu_0 H$ < -0.02 T, we do not observe a clear resonance, suggesting a multi-domain state of the thin film. For $\mu_0 H \leq$ -0.12 T, a sharp resonance feature is regained.

Here, the behavior is mirrored compared to $\mu_0 H$ > +0.12 T. The CPW has an inner conductor width of ω_{ic} = 20 μm, which provides a most prominent excitation at k_{I} = 0.096 $\times$ 10^4 rad/cm. From the slope of the resonance frequency we obtain a g-factor of 2.0. The value for M_{eff} is determined using Eq. 2.33 to be 426 kA/m. Using Eq. 2.30 together with Eq. 5.1 we obtain the first order anisotropy constant K_1 = 5.23 $\cdot 10^5$ J/m^3. The linewidth is found to decrease for increasing frequency (Fig. 5.3 (c)). This observation is opposite to the dependencies obtained for Py and CoFeB. This finding suggests different contributions to the linewidth than in the other ferromagnetic materials. We evaluate the effective damping parameter α_{eff}, which is between 0.01 and 0.04 depending on the frequency, as shown in Fig. 5.3 (d). The values are in good agreement with the ones reported in [Mac12]. A decreasing linewidth with increasing frequency/field is not consistent with Gilbert damping. Considering this, the intrinsic damping paramter α_{intr} could not be extracted.

In addition, we have conducted measurements using a different CPW with an inner conductor width of ω_{ic} = 4 μm, which provides a most prominent excitation at k_{II} = 0.31 $\times$ 10^4 rad/cm [Fig. 5.3 (b)]. In order to extract a group velocity we make use of the fact that we have measured the same sample with two different CPW's, i.e. two diffferent k-vector excitations. Normalized spectra at an external field of 0.44 T are shown in Fig. 5.3 (e). The frequency difference is used to calculate the group velocity via $v_{\text{g}} = \Delta\omega/\Delta k = 2\pi\Delta f/(k_{\text{II}} - k_{\text{I}})$. The group velocities obtained at different external fields are shown in Fig. 5.3 (f). The mean value for the group velocity amounts to 5.6$\pm$1.6 km/s. From this we obtain an attenuation length of L_{att} = 2.0 μm at 25.7 GHz.

5.3. Summary and Conclusion

In summary, we have studied three different systems, i.e. Py, CoFeB, and CoNi multilayer. The most important values are summerized in Table 5.1. The most common material in magnonics research is currently Py, offering low damping and isotropic magnetic properties. From a dynamics point of view, CoFeB is more favorable because it supports faster spin-wave propagation compared to Py. However, higher external fields are necessary to turn the magnetization into the out-of-plane direction for MSFVW-based devices. Here, materials exhibiting PMA come into play as they exhibit an

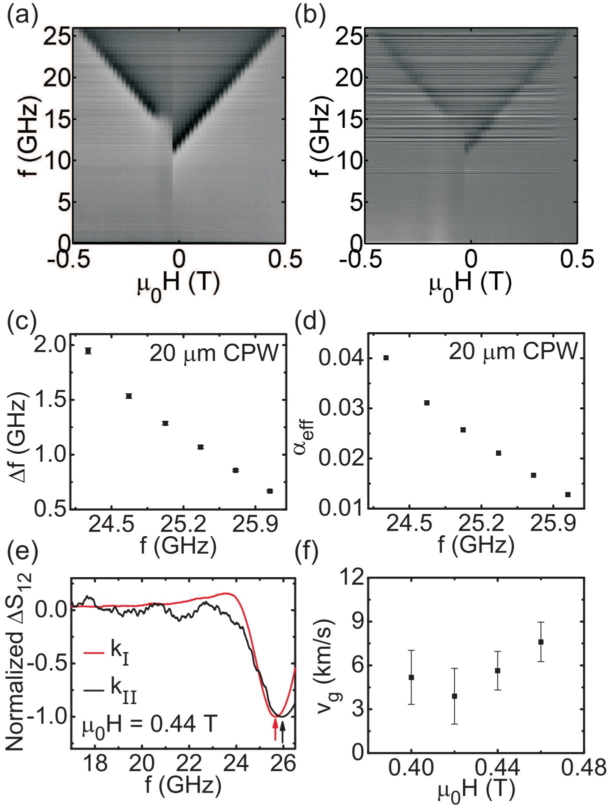

Figure 5.3.: Gray scale plots of one and the same CoNi multilayers placed on top of two different CPWs, i.e. one having an inner conductor width of 20 μm (a) and one being 4 μm wide (b). Extracted linewidth Δf and effective damping parameters α_{eff} as determined from the measurments using the 20 μm CPW. The shift in resonance frequency at a fixed field (e) is used to determine the group velocity v_{g} (f).

	t [nm]	M_{eff} [kA/m]	v_{g} [km/s]	α	L_{att} [μm]	$K_1 \times 10^5$ [J/m^3]
Py	20	820	1.0	α_{intr} = 0.008	2.7 (7.5 GHz)	0
CoFeB	20	1083	1.56	α_{intr} = 0.008	3.6 (8.6 GHz)	3.12
Co/Ni ML	19.1	326	5.6	$\alpha_{\text{eff}} \approx 0.025$	2.0 (25.7 GHz)	5.23

Table 5.1.: Summary of extracted parameters for three different thin films. For the CoNi multilayer we could not obtain the intrinsic damping parameter as explained in the text and therefore give the effective damping parameter α_{eff}.

out-of-plane magnetization even at zero magnetic field, which makes these materials very interesting especially for magnonic crystal devices. Our study shows that the Co/Ni multilayers show 4-5 times faster group velocities for approximately the same thickness if compared to Py and CoFeB. At the same time CoNi multilayers show an increase in effective damping, which then leads to a short propagation length. The reported decrease of the linewidth with increasing external field suggests different contributions to the linewidth if compared to the other two materials. The broadening of the ferromagnetic linewidth towards lower external fields could suggest a distribution of magnetization angles around the out-of-plane direction. This effect has been qualitatively discussed in Ref. [Bea09].

MSFVW-devices of this thesis have been fabricated using CoFeB and Py, as these were deposited in our own cleanroom. CoNi multilayers were not available for nanostructured devices.

6. 2-Dimensional Magnonic Crystals

In this chapter we study 2D antidot lattices (ADLs), i.e. periodic holes in a ferromagnetic thin film. We use Py and CoFeB and prepare holes in a regular square lattice using FIB (c.f. Chapter Preparation). The hole diameter is held constant at d = 120±10 nm and d = 190±10 nm for Py and CoFeB, respectively. The period p is changed depending on the specific experiment. We are presenting measurements using AESWS as well as micromagnetic simulations using the software tool MicroMagus. We will refer to different simulation parameter sets, which can be found in Appendix A.3. The first part of this chapter is dedicated to the creation of complete band gaps, i.e. forbidden frequency gaps, only by geometrical parameters. Here, complete means that the forbidden gaps open for the two different in-plane directions and overlap. The second part covers devices that exploit forbidden frequency gaps, i.e. the unique characteristics of the newly created dispersion relations.

After showing that complete band gaps exist in 2D MCs formed by square ADLs, we address the question how we can use these band structures for new MC devices. As mentioned in Ref. [Len11] one of the building blocks of future devices based on MCs is the guiding of spin waves. This is not at all trivial for spin waves because of their anisotropic dispersion relation and has been the subject of research for quite some time [Bai01, Cho07, Dem08, Bao08, Vog12]. In section 6.3 we follow a new approach in that we introduce line defects (LD) in our 2D MCs with perpendicular magnetization, i.e. we leave out one row of ADs, to study how this can be used as a magnonic crystal waveguide (MCWG). In section 6.3.1 and section 6.3.2, we propose further devices using this approach of artificially introduced defects such as a bended waveguide and a spin-wave splitter respectively.

Sections 6.1 and 6.3 have been published in Ref. [Sch12b] and Ref. [Sch13], respectively.

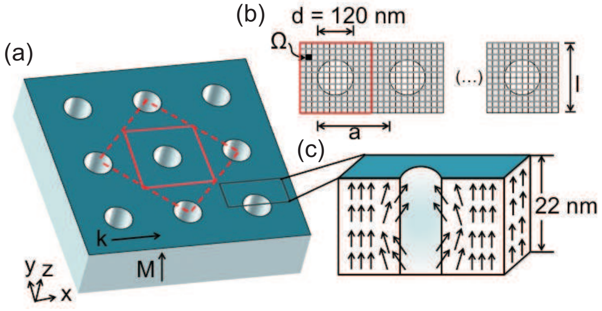

Figure 6.1.: Simulation geometry as used for micromagnetic simulations of regular antidot lattices (a). The unit cell is indicated by a continuous red line for normal configuration and for the 45° configuration with a red dashed line (b). The unit cell is subdivided in regular pixels of size Ω and repeated N times into the x-direction. 2D periodic boundary conditions are applied. (c) Spin-configuration at the hole and in the continuous film as determined by simulations at 1.2 T. The film thickness has been subdivided into four layers for the simulations.

6.1. Complete Band Gaps in Antidot Lattices

It is intuitive to start with micromagnetic simulations on ADLs to establish the necessary geometrical parameters to create tailored spin-wave properties in out-of-plane fields. In Fig. 6.1 (a) and (b) we show the simulated geometry. For the simulations at $\mu_0 H$ = 1.2 T we use Py and simulation parameter set A. In (c) we show the magnetization configuration extracted from simulations considering four layers in the z-direction. At 1.2 T the magnetization is canted at the holes edges as indicated by the black arrows. For higher fields, the magnetization becomes more and more uniform throughout the whole sample.

For comparison, we repeat the dispersion relation $f(k)$ for a Py plain film in Fig. 6.2 (a) (taken from chapter 2.6.1). The faintly bright regions around k = 0 are attributed to numerical artefacts coming from the discretization in real space due to the finite-sized simulation cells. Next, we simulate square ADLs with constant hole diameters d = 120 nm, whereas the period p is varied (800 nm $\geq p \geq$ 180 nm). In Fig. 6.2 (b) we show the simulated dispersion relation of an ADL with p = 800 nm. Here, additional branches appear. Analyzing their absolute values we find that they represent backfolded branches of the thin film dispersion. We display the dispersion relation in the so-called extended zone scheme where k extends beyond the first Brillouin zone (BZ) boundary located at $k_{\mathrm{BZ}} = \pi/p$ (vertical broken line). We do not observe a forbidden frequency gap within our simulation accuracy of 100 MHz. As we reduce the period of the ADL to p = 240 nm the BZ boundary moves to higher values. Importantly we observe a clear frequency gap of Δf = 1.2 GHz between 8.9 GHz and 10.1 GHz at the first BZ (Fig. 6.2 (c)). In addition the frequency at the Γ-point, i.e. k = 0, increased to $f(k = 0)$ = 8 GHz in comparison to $f(k = 0)$ = 6.1 GHz for the plain film. In the simulations of the ADLs the artefacts at around k = 0 are even more pronounced if compared to the plain film. This is attributed to the discretization of the ADs edge. To support this we repeated the simulation of the ADL with $p = 240$ nm using a different amount of pixel, thus, changing the discretization of the ADs edge. In Fig. 6.2 (e) and (f) we show the simulated spectra at k = 0 using 128 pixel (red line) and 56 pixel (black line) for discretizing the unit cell. First, we observe no shift of the main resonance at 7.4 GHz within the simulation accuracy of 100 MHz. Looking closely at the lower frequency side (Fig. 6.2 (f)) we see that the strength as well as the peak positions of the artefacts change drastically with the discretization of the unit cell. Nevertheless, for the discussion, we will focus on regimes of the wave vector k where artefacts do not play a role.

In order to study whether a complete band gap is formed, we perform a simulation with k being along the diagonal of the ADL, i.e. under 45° to the x and y direction. To make use of 2D-boundary conditions we now construct a conventional unit cell having an effective periodicity of $p_{\mathrm{eff}} = p \cdot \sqrt{2}$ along the considered stripe. In the as-simulated dispersion relation we find a frequency gap near 9.8 GHz with Δf = 0.6 GHz (Fig. 6.2 (d)). This band gap overlaps in frequency with the band gap obtained from the simulation where k is along a primitive vector. We observe additional branches at $k = \pi/\sqrt{2p}$, which do not create an avoided crossing at $k = \frac{1}{2}\sqrt{2}\pi/p = \pi/\sqrt{2}p$. This is due to the fact that we have used a conventional unit cell with 2D-boundary conditions, instead of a primitive unit cell. This leads to additional lattice points in reciprocal space and consequently additional branches in our simulation [Hun12].

We now extend this study in that we consider different periods of the ADL between 180 nm and 800 nm. The extracted frequencies reflecting the band gaps are summarized in Fig. 6.3. Two main features can be ex-

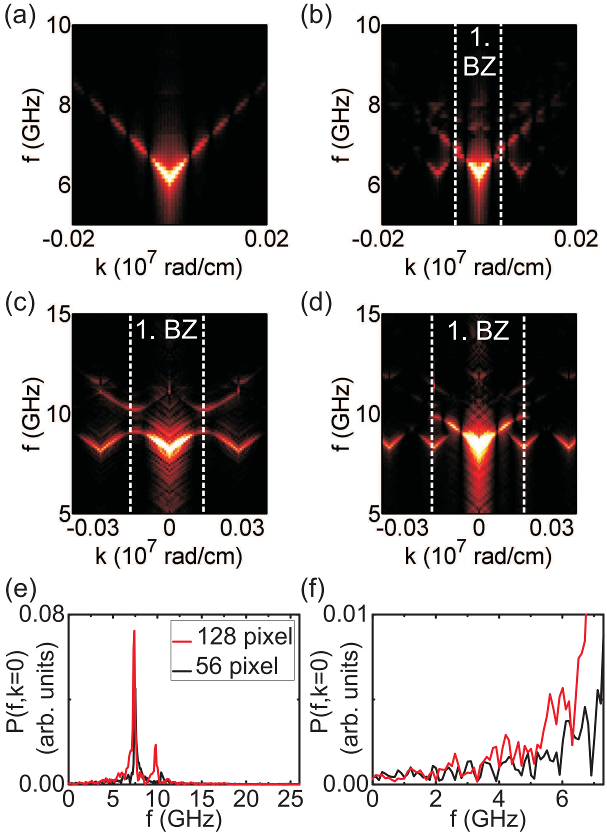

Figure 6.2.: Color coded spin-wave dispersion for (a) plain film, (b) ADL with $p =$ 800 nm and (c) ADL with $p = 240$ nm when k is pointing along a primitive vector, and (d) 45 deg-rotated k pointing along the diagonal of an ADL with $p = 240$ nm. Here dark color means no spin-wave excitation and bright means high spin-wave excitation. In (b), (c) and (d) the first BZ is indicated by the white dashed line. Note that due to the discretization of the holes edges being periodic from unit cell to unit additional spin waves are faintly excited. In a real device we do not expect to observe such features as the edge roughness over the MC would be irregular. To support this we show line plots taken from simulated ADL with $p = 240$ nm at $k = 0$ in (e) and (f), where we changed the discretization of the unit cell using 128 pixel (red line) and 56 pixel (black line).

tracted from this. As the lattice period is reduced, the eigenfrequencies increase and in addition, the size of the band gap increases. From this we conclude that in particular, nanopatterning on the 100 nm length scale is key to obtaining significant forbidden frequency gaps in ADLs.

We followed a phenomenological approach to model the dependency of the band gaps as a function of the period we assume an exponential fitting function, which reads:

$$f(p) = A \cdot \exp(-p/\tau) + f_0. \tag{6.1}$$

This is assumed following recent results obtained on one-dimensional MCs suggesting the coherence length or dipolar coupling length of spin waves to be decisive for modeling backfolded branches in 1D quantitatively [Top10]. It is possible that dipolar coupling between spin excitations modifies frequency gaps originating from Bragg reflection in a periodic potential. Our simulations generically consider all mechanisms involved. An exact analytical function for describing the data in Fig. 6.3 is not available. In the inset of Fig. 6.3, we show frequency gaps for two different ADLs for the ΓK direction.

6.2. AESWS on Antidot Lattices in Perpendicular Fields

We now experimentally study ADLs in out-of-plane fields using AESWS. As the group velocity for Py is rather low for a 20 nm thick film (c.f. chapter 5), for the following experiments we prepared ADLs in CoFeB films and additionally increased the thickness of the samples to 41 nm. Using Eq. 2.42 with the material parameters of CoFeB we obtain a group velocity for a 41 nm thick film of v_g = 3.2 km/s. For the experiments we use a transmission CPW with a prominent excitation at k_1 = 0.6×10^4 rad/cm. Note that the hole diameter in CoFeB is 190 nm, i.e. about 70 nm larger than the hole diameter for Py. We start by comparing resonance frequencies of a plain film with those of ADLs with different lattice periods (Fig. 6.3 (b)). We see a clear upshift in frequency as the lattice period is reduced, which is consistent with the simulation data. We explain this trend by a change in the out-of-plane demagnetization factor.

Next we extract the group velocity from the oscillations in ΔS_{21} (c.f. chapter 3.4). For a lattice period of 800 nm the group velocity is found to be slightly below the group velocity of the reference plain film. Decreas-

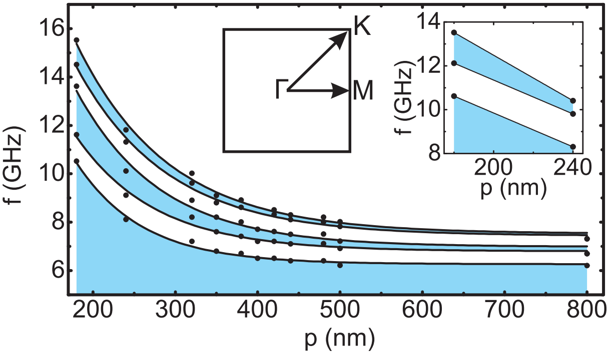

Figure 6.3.: Symbols denote eigenfrequencies extracted at BZ boundaries for ADLs with different period p and k pointing along ΓM direction (see inset). The colored regions indicate the forbidden frequency regions evaluated from the simulations. The white areas denote the widths of the allowed minibands. The straight lines are guides to the eyes obtained by fitting exponential functions. In the inset we show eigenfrequencies at BZ boundaries (symbols) for ADLs with different period p and k pointing along ΓK direction, i.e., under $45°$. Again the colored regions indicate the forbidden frequency regions evaluated from the simulations. Straight lines are guides to the eyes.

ing the lattice period to 600 nm results in much lower group velocity of 2.7±0.2 km/s.

6.3. Artificially Introduced Line Defects as Waveguides

The samples for these experiments have a period of 600 nm and are of CoFeB having the same thickness (41 nm) as the samples of the ADLs discussed in section 6.2. Now we leave out every 20th row of ADs in order to create line defects (LDs) along the y-direction, i.e. perpendicular to the CPW. SEM pictures of the device are shown in Fig. 6.5 (a). Transmission CPWs are prepared on this device to measure propagating spin-waves along the LDs. A sketch of a typical band diagram of such a magnonic crystal is shown in Fig. 6.5 (b) and will be discussed later.

In the measured spectra we identify four resonance modes, which we extract from the line plot of the imaginary part of ΔS_{11} [Fig. 6.6 (a)]. We indicate those resonances by black arrows in the line plot at an exter-

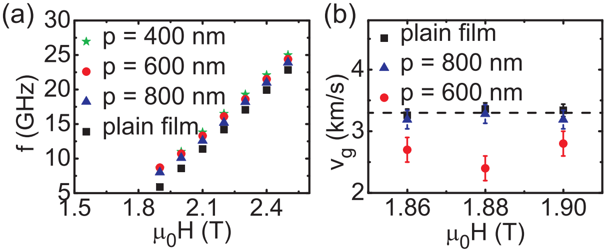

Figure 6.4.: (a) Field dependency of the eigenfrequencies for different ADLs with different period p extracted from measurements. (b) Group velocities for different lattice periods p compared to the group velocity of the plain film.

nal field of 1.82 T. Considering the different demagnetization factors of ADL and LDs we assume that the lowest frequency mode is the mode at k_1 localized in the LD and the next higher mode belongs to the ADL. The third and fourth mode belong to the respective excitations at $k_2 = 2.5 \times 10^4$ rad/cm. In the following we will restrict our analysis to the lowest two modes. In Fig. 6.6 (b) we plot the lowest two modes over the external field. The inset shows all four resonances over a smaller field regime. We now turn our attention to the propagation signal ΔS_{12} shown in Fig. 6.6 (c) for an external field of 1.88 T. The oscillating signal near 6.8 GHz in ΔS_{21} reflects propagation in mode (1) of the MCWGs. The extracted velocity amounts to $v_\mathrm{g} = 3.0 \pm 0.2$ km/s, which is close to the plain film value of $v_\mathrm{g} = 3.3$ km/s. The next higher lying resonance frequency in Fig. 6.6 (c) is attributed to the ADL excited at k_1 [mode (2)].

In order to confirm the origin of the two different modes we performed micromagnetic simulations at $k = 0$ at a fixed field of 2.5 T (simulation parameter set B in the addendum). The spectrum of the simulation is shown in Fig. 6.6 (d), where we indicate the position of the measured frequencies of the first two modes by stars. The simulations predict well the frequency separation between modes (1) and (2). Considering the different wave vectors for the simulation ($k = 0$) and the experiment ($k = k1$), the one-to-one correspondence of simulated and measured eigenfrequencies f points towards a systematic but small error in the simulation. In Fig. 6.6 (e) we show the spatial spin-wave profiles of the two modes extracted from the simulation. Here white is a high spin-wave amplitude and black is a low spin-wave amplitude. The frequencies of those two modes coincide with the frequencies of mode 1 and mode 2 from the experiment. As we are not simulating with the excitation spectra of the CPW, the simulation does not predict the two additional modes for k_2 = 2.5×10^4 rad/cm. The fact that the waveguide mode lies below the first band is similar to the so-called index guided modes in photonic crystal waveguides [Joa08, Jam03]). But there is one distinctive difference between the photonic crystal waveguide and the MCWG. If we follow the first band of the MC down to k = 0 (c.f. Fig. 6.5 (b)) we find that the frequency f_0 at k = 0 is higher than the frequency of the MCWG at k_1. In photonic crystals, the frequency at k = 0 is always lower than that of index guided modes.

In addition to the simulations at k = 0, we perform simulations with a localized excitation in order to get time dependent data (simulation parameter set C with a thickness of 41 nm). Note that here we use open boundary conditions in order to reduce simulation time. To assure that the boundaries of the simulation cell do not affect the outcome of the simulation, we have constructed a simulation cell with 15 periods of ADs (p = 600 nm) to both sides of the LD. This is consistent with simulations of 1D magnonic crystals [Kim09], where twelve periods are suggested for simulations. We use a continuous wave excitation with a frequency of f = 24.1 GHz as extracted from the experiment at μ_0H = 2.5 T [1]. From the simulation we obtain time dependent spin-wave amplitudes. In Fig. 6.6 (d) we show the spin-wave amplitudes at different times, where one can see the propagation within the LD. Please note that we show just the center part of the simulation cell (original simulation plots can be found in Appendix A.4)[2].

It is now instructive to compare the measured group velocity of about 3 km/s with values v_g of an individual CoFeB stripe acting as a magnonic wave guide. Taking the geometrical width of the MCWG (= 1020 nm), which is the edge-to-edge separation of holes (see white dashed lines in Fig. 6.5 (c)). For this we perform micromagnetic simulations on a device shown in Fig. 6.7. Here simulation parameter set D is used and 2D periodic boundary conditions are applied. The magnetic material takes

---

[1] At the excitation frequency of 24.1 GHz we find only the line defect mode to be excited. Changing the excitation frequency to f = 25 GHz excites again the line defect mode (with different wavelength) but also the ADL. Going to lower excitation frequency (f = 15 GHz) we observe no excitation of either mode.

[2] We show snapshots of the time dependent spin-wave amplitudes only after a settling time of $t \geq 2$ ns because of transient response of the system.

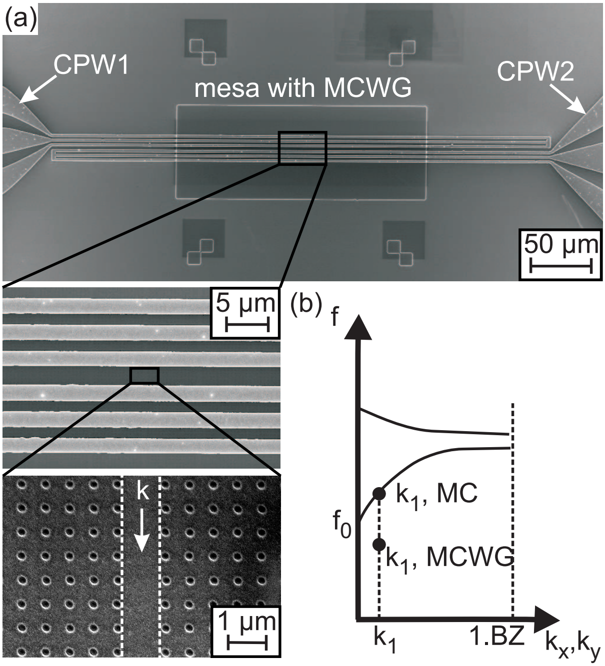

Figure 6.5.: (a) Scanning electron microscopy images of a magnonic crystal wave guide device. The hole diameter (period) is 190 nm (600 nm). The white dashed line indicates the geometrical width of the MCWG of 1020 nm. (b) Sketch of the band structure for MSFVWs in a square-lattice magnonic crystal. We indicate the frequency of a MCWG.

up half of the simulation width (w_2), illustrated by the dark gray color. From the simulated dispersion relation we extract the group velocity in the limit of small wave vectors using a linear fit. For $w_2 = 1020$ nm and $\mu_0 H = 1.9$ T, we obtain $v_\mathrm{g} = 1.9 \pm 0.2$ km/s. The stripe thus supports substantially slower spin waves compared to the MCWG (slower by about 30 %). To check the outcome of the simulation, we also considered $w_2 = w_1$, i.e., we modelled the plain film. Here, we extracted a group velocity of $v_\mathrm{g} = 3.3 \pm 0.2$ km/s. This value was in good agreement with the calculated group velocity of $v_\mathrm{g} = 3.3$ km/s, substantiating the reliability of the micromagnetic approach.

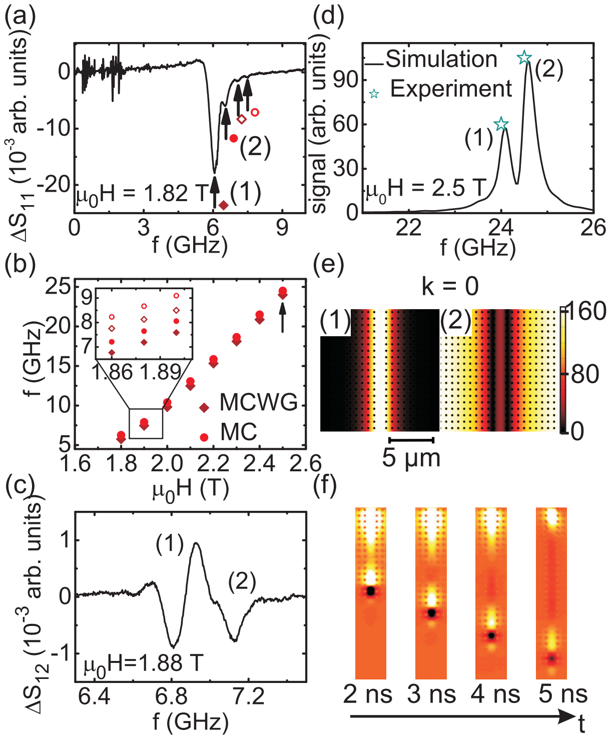

Figure 6.6.: (a) Multiple resonances (arrows) of an ADL with MCGWs at 1.82 T. (b) Field dependencies of the two most pronounced modes [mode (1) and mode (2)] and all four resonances at small H (inset). Filled and open symbols defined in (a) stand for excitations at k_1 and k_2, respectively. (c) Transmission signal measured for mode (1) and (2) of the ADL with MCWGs at 1.88 T. (d) Simulated spectrum of the ADL with MCWGs at 2.5 T compared to the measured eigenfrequencies (open stars). (e) Spin-precessional amplitudes as simulated for mode (1) mode (2) seen in the spectrum of (a). The color code for amplitudes is shown on the right. (f) Snapshots of the time dependent spin-precessional amplitudes in a MCWG using a continuous wave excitation with a frequency of f = 24.1 GHz at 2.5 T.

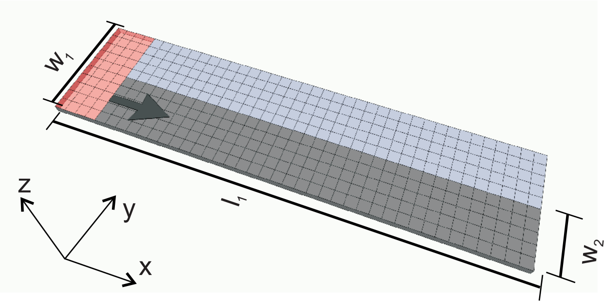

Figure 6.7.: Simulation geometry of a ferromagnetic stripe for $w_2 \neq w_1$ and a plain film for $w_2 = w_1$. The group velocity is then obatined from the slope of the dispersion relation.

If we now take a closer look at the spin-wave profiles in Fig. 6.6 (c) we can see that the spin-wave excitation is not only localized within the LD. It extends into the ADL. This suggests that we have to consider an effective width for the MCWG. The concept of an effective width for stripes was introduced by Guslienko et al. [Gus02]. In order to explain the quantized modes found in stripes they introduced an effective ”pinning” parameter d:

$$d(a) = \frac{2\pi}{a[1 + 2ln(1/a)]} \tag{6.2}$$

with a being the aspect ratio of the stripe (p = thickness/width). This can also be written as an effective width w_{eff}:

$$w_{\text{eff}} = w[d/(d-2)]. \tag{6.3}$$

Calculating the effective width of a stripe with d = 1.02 μm we get w_{eff} = 1.13 μm. Repeating the simulation of the stripe using this effective width we obtain a group velocity of v_g = 2±0.2 km/s, still lower than the measured group velocity of the MCWG. Now we approximate the effective width by taking the width of the spin-wave profile from Fig. 6.6 (c), which is roughly w_{eff} = 1.8 μm. The group velocity extracted from a simulation using this effective width gives us v_g = 2.6±0.2 km/s, which comes close to the measured group velocity of the MCWG. We summarize all group

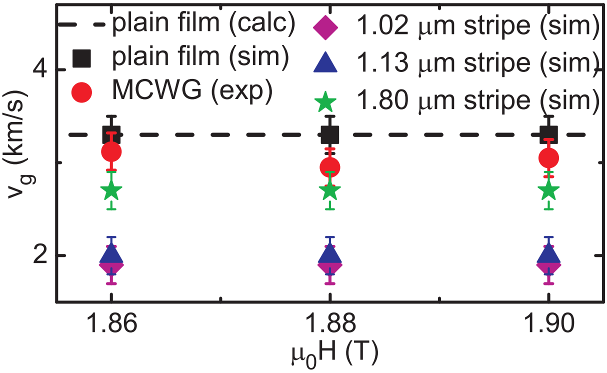

Figure 6.8.: Simulated and measured v_g of a plain film (squares), MCWG (circle), and three stripes of different widths, i.e. 1.02 μm (diamond), 1.13 μm (triangle), and 1.80 μm (star). The dashed line is the reference group velocity calculated from the dispersion relation of the unpatterned film.

velocities in Fig. 6.8 (b). Our analysis suggests a MCWG as prepared here supports a group velocity v_g, which would be present in a conventional stripe-like wave guide of much larger geometrical width.

6.3.1. Guiding Spin Waves around a Corner

In the previous section we showed that spin waves are guided efficiently using a straight MCWG. In the following we address the challenge to guide spin waves in arbitrary in-plane directions. This challenge has been the subject of recent studies [Cla11, Vog12], all of which used ferromagnets subject to an in-plane magnetic field, where the dispersion relation is anisotropic. In the framework of this thesis we make use of MSFVW, for which the dispersion is isotropic. Still it is unexplored how MSFVWs are guided around a corner. This, however, is essential if one thinks of integrated and interconnected magnonic devices.

We have fabricated an ADL device from 41 nm thick CoFeB in the same manner as before with integrated CPWs for transmission measurements [Fig. 6.9 (a)]. The period has been set to 500 nm and every 15th row has been modified as shown in Fig. 6.9 (a). The missing row and therefore the path for the spin-wave is indicated by the white dashed line. We will call this device a wave guide bend (WGB) in the following. In Fig. 6.9 (b) we show a spectrum ΔS_{11} at $\mu_0 H$=1.82 T. We observe two main resonances indicated by the black arrows. Following our earlier analysis, we identify the lowest mode as the mode localized within the WGB and the next higher mode as the one stemming from the surrounding ADL.

It is now intruiging to analyze the group velocity of spin waves following the WGB. In Fig. 6.9 (c) we have plotted the group velocities at different external fields as extracted from ΔS_{12}. Note that spin waves which follow the WGB have to travel a longer path in order to reach the detecting CPW (path length through wave guide = 13.6 μm). For calculating the group velocity we have considered the additional path of 1.6 μm. We find that the group velocity is smaller than the group velocity of a plain film of CoFeB of the same thickness. Finally, we perform micromagnetic simulations. We use material parameters of CoFeB and simulation parameter set C. The simulation cell is constructed of an ADL with p = 500 nm and a thickness of 41 nm. We apply continuous wave excitation with a frequency of f = 22.7 GHz, which is the resonance frequency of the first mode at 2.5 T taken from the experiment. In Fig. 6.9 (d) we display snapshots after different time periods of 2 ns, 4 ns, and 6 ns after the initial excitation. One clearly sees a spin-wave ”packet” following the WGB. This result supports and illustrates our experimental findings.

Apart from the group velocity, we can use the whole set of S-parameters and with Eq. 3.25, compare the attenuation length L_{att} of a plain film, a straight wave guide, and a WGB device. In Fig. 6.10 we plot L_{att} for the plain film, a regular ADL, and the other two devices at different fields (symbols) together with the respective mean values (dashed lines). The attenuation length of the plain film is L_{att} = 16.9 μm, whereas for the ADL, the line defect, and the WGB we extract L_{att} = 5.3 μm, L_{att} = 5.2 μm, and L_{att} = 6.3 μm respectively. The comparison reveals that introducing ADs reduces the attenuation length by a factor of 3 if compared to the attenuation length of a plain film. Note that the group velocity only changes by a factor of 1.2 comparing a plain film with an ADL. Introducing straight or bended line defects does not affect the attenuation length of the spin waves propagating through such wave guides compared to the ones propagating through an ADL.

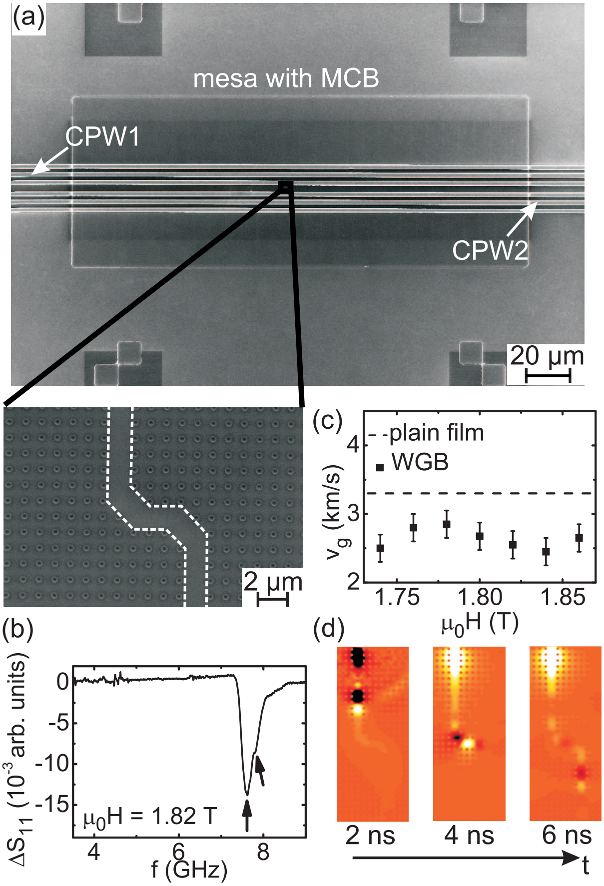

Figure 6.9.: (a) Scanning electron microscopy images of a wave guide bend device. The white dashed line indicates the path where we left out holes. (b) Measured spectrum at 1.82 T indicating two prominent resonances by arrows. (c) Group velocity of the WGB mode (squares) evaluated for different external field values and compared to the group velocity of a plain film (dashed line). (d) Snapshots of the time dependent spin-precessional amplitudes in a WGB using a continuous wave excitation with a frequency of f = 22.7 GHz at 2.5 T.

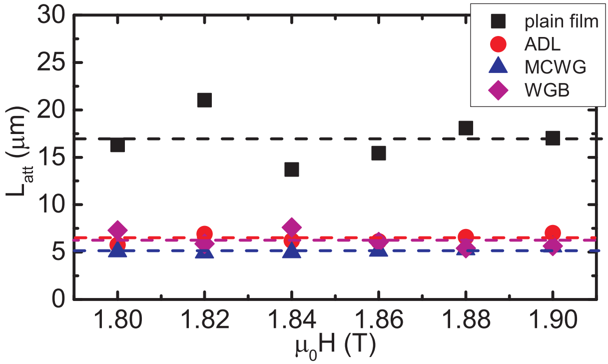

Figure 6.10.: Comparison of the attenuation length L_{att} at different fields (symbols) and the mean values (dashed lines) for a plain film (squares), a ADL (circles), a MCWG (rectangles), and a WGB (diamonds).

6.3.2. Splitting of Spin Waves in a Two-Path Device

We have designed a MC splitter (MCS), which splits a spin-wave into two paths before uniting it again after a short distance. SEM images of our sample are shown in Fig. 6.11 (a). The sample is made from 53 nm thick CoFeB with a period of the ADL of 500 nm. The path of the artificially introduced defect state is marked by the white dashed line. The structure is repeated after every 15th row of ADs. In Fig. 6.11 (b), we plot the field dependency of the first two modes observed in our measurements. Like in the other structures, we identify the lowest mode as the mode which is localized within the regions where we left out holes.

An evaluation of the group velocity for the lowest mode gives us a similar result as for all the devices based on missing rows of ADs, i.e. the group velocity of the MCS is slightly below the group velocity of the plain film (Fig. 6.11 (c)). We employ micromagnetic simulations with material parameters of CoFeB and simulation parameters C. The simulation cell is constructed of an ADL with p = 500 nm and a thickness of 53 nm. We use a continuous wave excitation with a frequency of f = 22.8 GHz, which was evaluated to correspond to the resonance frequency of the first mode at 2.5 T from the experiment. In Fig. 6.11 (d) we show snapshots after different time periods. We see how the spin wave is split into two paths (t

= 2.5 ns), travels within the two arms (t = 4.5 ns), and finally is combined at the end of the device (t = 6 ns). Apart from the splitting of spin waves we have additionally shown that one can also combine spin waves again.

6.4. Summary and Discussion

In this chapter we discussed magnonic crystals that exhibit complete band gaps by considering periodic antidot lattices in perpendicular fields. The existance of band gaps has been observed using micromagnetic simulations. In addition, simulations predict an increase in resonance frequency for decreasing lattice periods. This has been confirmed by AESWS experiments. Furthermore, a reduction of the group velocity by going to smaller periods has been obeserved in our measurements. The reason for this behaviour can be found in the modified dispersion relation, when introducing a regular ADL. In simulations of such ADLs, we observe the existance of forbidden frequency gaps accompanied with a gradual change of slope of the dispersion relation, i.e. at the 1. BZ boundary the slope is zero. As we observe a decreasing group velocity for decreasing ADL periods we conclude that the slope of the dispersion changes at k_1 of the CPW in such a manner that the measured group velocity decreases for smaller lattice periods.

Making use of the forbidden frequency regions created by the ADL, we have explored wave guides by removing rows of AD's. We showed that spin waves are located within this line defect and are guided through the ADL. Even more intruiging, we showed that the group velocity in such a device is very close to the group velocity of the plain film and higher when compared to a simple magnetic stripe of the same geometrical width. We assume that this is due to a relatively large effective width of the wave guide caused by leaking of the spin wave into the ADL. We also showed the difference of a MCWG compared to its photonic crystal counterpart in that the excitation frequency lies below the frequency at $k = 0$ of the lowest band. This implies that the MCWG mode cannot scatter into another branch of the dispersion relation.

Furthermore, we have shown that artificially introduced line defects can be used in guiding spin waves around corners in complex structures such as a spin-wave splitter. Here, we showed that spin waves can be divided into two different paths and even be united again. The devices based on ar-

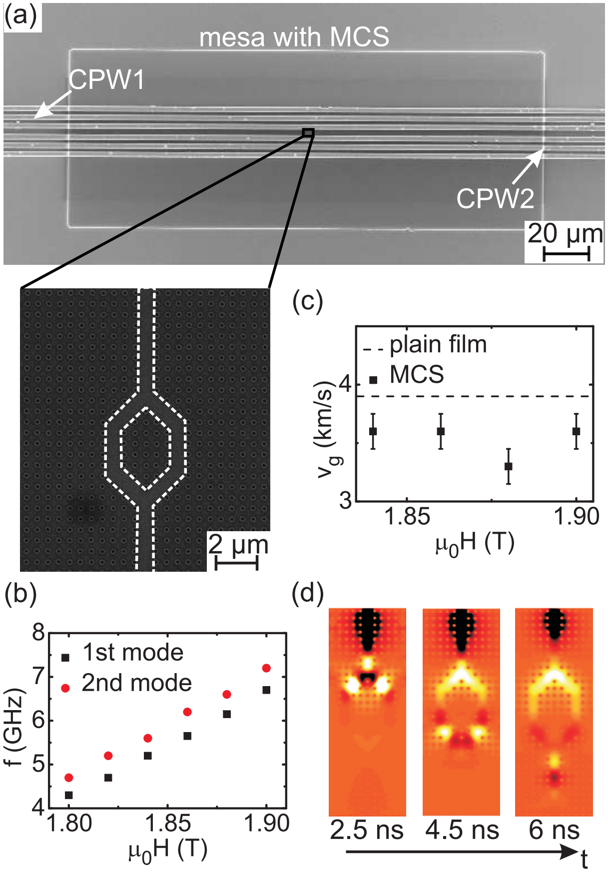

Figure 6.11.: (a) Scanning electron microscopy images of a magnonic crystal splitter device. The white dashed line indicates regions where we left out holes. (b) Field dependency of the first two modes extracted from the measurement. (c) Group velocities at different field values evaluated for the MCS mode (squares) and compared to the group velocity of the plain film (dashed line). (d) Snapshots of the time dependent spin-precessional amplitudes in a MCS using a continuous wave excitation with a frequency of f = 22.8 GHz at 2.5 T.

tificially introduced imperfections in generall support fast spin wave propagation almost as high as in a plain film. The attenuation length in such devices is found to be comparable to the attenuation length of a regular ADL. We will give a more visionary discussion on how to utilize such a spin-wave device in the final outlook section of this thesis.

7. Protein Based 3-Dimensional Magnonic Crystals

After the discussion of 2D MCs in the previous chapter we now present our results on 3D MCs. 1D and 2D MCs have been the subject of intense research over the last years. Still, there is lack of experimental work on 3D MCs as periodic nanopatterning of ferromagnets in three spatial directions is a great challenge. Only very recently, Kostylev et al. have presented first FMR measurements on 3D magnetic inverse opal structures [Kos12] forming a possible candidate for a 3D MC. Recent advancements in the field of bioengineering make it possible to create large arrays of magnetic nanoparticles (NPs), called magnetoferritin, ordered in three dimensions. Diluted magnetoferritin NPs have been studied in the past using cavity ferromagnetic resonance technique at a fixed frequency of 9.43 GHz (X-band) and temperatures ranging from room temperature down to 4.2 K [Gus07]. Using electron magnetic resonance (EMR) at 9.2 GHz (X-band) at liquid helium temperature Li et al. studied anisotropies in such diluted systems of nanoparticles [Li09]. Furthermore, theoretical calculations using the plane wave method showed large tailored spin wave band structures with allowed and forbidden frequency gaps by filling the air gaps between ordered arrays of magnetoferritin with a second ferromagnetic material [Kra08a, Kra08b, Mam12]. Here we study the dynamic properties of ordered magnetoferritin NPs in view of 3D MC properties experimentally.

The crystals studied here have been prepared by the group of Prof. W. Schwarzacher at the University of Bristol. The NPs consist either of γ-Fe_3O_4 (maghemite) or Fe_3O_4 (magnetite). These magnetic NPs are enclosed by a protein cavity called apoferritin, hence the name magnetoferritin (Fig. 7.1 (a)). Under appropriate conditions, the proteins crystalize in a regular fcc-lattice (Fig. 7.1 (b)). For details of the fabrication process we refer the interested reader to Ref. [Kas08] and references within.

The first part of this chapter is dedicated to develop an understanding of the dynamic properties, i.e. resonance frequencies and damping of the NP arrays. We distinguish the properties above and below the blocking tem-

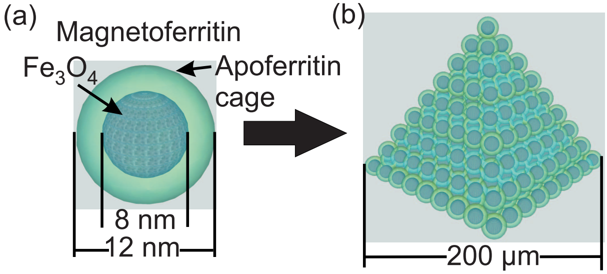

Figure 7.1.: Sketch of a single apoferritin cage with magnetite (Fe_3O_4) nanoparticle enclosed in its cavity (a). The whole is then called magnetoferritin. Under appropriate conditions these Proteins can form a regular array in a fcc lattice via self organization (b).

perature T_B of the NPs, i.e., in the superparamagnetic and ferromagnetic state, respectively. In the second part we study collective behaviour, i.e. the interaction of the NPs. In the last part we study the possibility of doping magnetoferritin crystals with cobalt in order to increase the blocking temperature of the NPs.

7.1. Dynamic Properties of Magnetoferritin Nanoparticles between 5 and 290 K

In Fig. 7.2 (a), we show a sketch of the experimental setup for broadband spectroscopy. In order to study the dynamic response of magnetoferritin crystals we place them on top of a CPW fixed with dried $CdSO_4$ solution. The field direction is in the out-of-plane direction, i.e. pointing perpendicular to the plane of the CPW. We study four different samples, A to D in this chapter. Sample A consists of 50 crystals of maghemite placed on top of a CPW (Fig. 7.2 (b)). Sample B and C contains four crystals of magnetite and just one crystal of magnetite, respectively (Fig. 7.2 (c-d)). For sample D, we employed the FIB technique to cut out a cubic NP array from a regular crystal of magnetite [Oku13] and placed it on top of a CPW (Fig. 7.3).

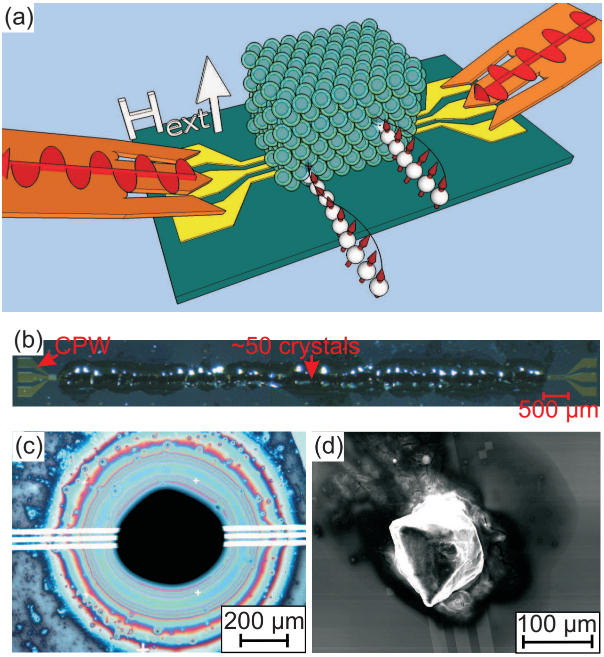

Figure 7.2.: (a) Sketch of the experimental setup for AESWS measurements. The specimen is placed on top of the CPW and fixed with dried $CdSO_4$ solution. The applied magnetic field is oriented in the out-of-plane direction as indicated by the white arrow. (b) Optical microscope image of sample A. In (c) and (d) an optical and scanning electron microscopy image, respectively, of sample C is shown.

7.1.1. Resonance Frequencies

First, we compare resonance frequencies detected on the four different samples. In Fig. 7.4 we show typical line plots of the measured signal ΔS_{12} at 290 K and at 5 K at an external magnetic field of 0.5 T. Here the resonance frequencies match between all samples. The signal strength decreases as the amount of magnetic material is reduced. Comparing the signals at 290 K and 5 K, we obeserve a shift to higher frequencies as well as a line broadening for all four samples.

The extracted resonance frequencies at 290 K for different field values

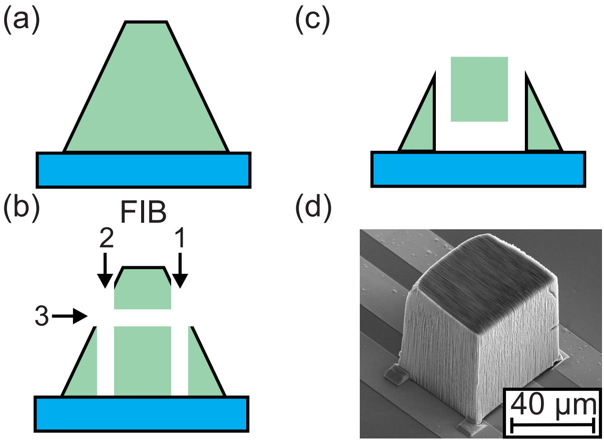

Figure 7.3.: Sketch of the FIB process to prepare a cubic sample of magentoferritin (a-c). The sample is cut by FIB in different directions before lifted up and placed on top of a CPW. (d) SEM image of sample D placed on top of the CPW.

are summerized in Fig. 7.5 (a). At 290 K we resolve a resonance for magnetic fields larger than 200 mT. The frequencies agree well for all samples and from the slope we extract $\gamma/2\pi$ = 28.6 GHz/T. This value corresponds to a Landé factor of 2.04. In Fig. 7.5 (b) we show the field dependent resonance frequencies measured at 5 K. Here, we observe a resonance at zero field. At low fields, i.e. below 0.4 T, the resonance frequencies are found to vary slightly from sample to sample, whereas at higher fields, the resonance frequencies are very close and follow the same linear dependency as for 290 K. The different field dependencies observed for 290 and 5 K are taken above and below the blocking temperature T_B = 18 K extracted from magnetization curves [Oku12]. The NP arrays are therefore in the superparagmagnetic and ferromagnetic states, respectively. In the superparamagnetic state, we need a minimum field of 200 mT to align the moments and restore a resonance. In the ferromagnetic state, the spontaneous magnetic order allows us to observe a resonance also at $\mu_0 H$ = 0 T. The resonance near $\mu_0 H$ = 0 T will be investigated further in the following.

We use Eq. 2.48 derived from chapter 2.4 to model the experimental results. The black line in Fig. 7.5 (b) is a best fit to the measurements

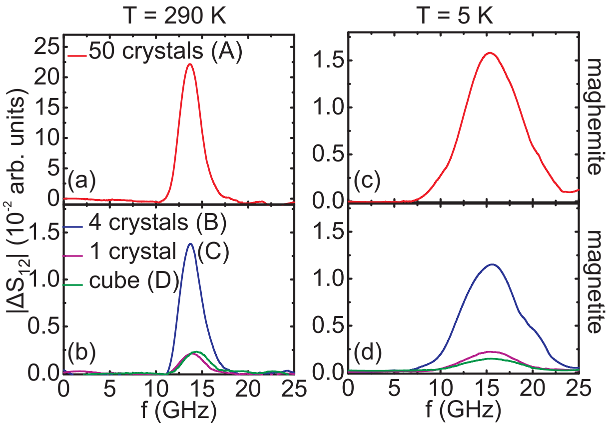

Figure 7.4.: Typical data of ΔS_{12} as detected by the VNA (a-d). Room temperature data are shown in (a) and (b) for maghemite and magnetite samples respectively. Spectra at T = 5 K are shown in (c) and (d) for maghemite and magnetite respectively.

obtained by Eq. 2.48. To obtain this curve, the following parameters have been used. The magnetic moment of a single NP in the crystal was estimated to be $6000\mu_\mathrm{B}$ (μ_B is the Bohr magneton). The NP radius is set to $R = 4$ nm [Kas08]. Thus, the saturation magnetization of the NP is calculated to be $M_\mathrm{S} = 6000\mu_\mathrm{B}/V = 0.208 \times 10^6$ A/m. The effective anisotropy field $H_\text{eff,ani} = |H_\text{ani}| + |H_\text{sur}|$, i.e., the anisotropy field which includes volume and surface contributions, can be estimated from the blocking temperature T_B = 18 ± 1 K measured with SQUID [Oku12] and following Ref. [Far05]:

$$\mu_0 H_\text{eff,ani} = \frac{2K_\text{eff}}{M_\mathrm{S}} = \frac{2K_\text{eff}(25T_\mathrm{B}k_\mathrm{B})}{V}, \tag{7.1}$$

where k_B is the Boltzmann constant and K_eff is the effective magnetocrystalline anisotropy constant. From this we get a magnetic anisotropy field of 0.236 T. We assume the Landé factor to be the value of the free electron (g = 2.0), which is close to the experimental value found here and in Ref. [Bic50]. The surface anisotropy constant and the angle between hard axis direction and the direction of the external magnetic field are used as

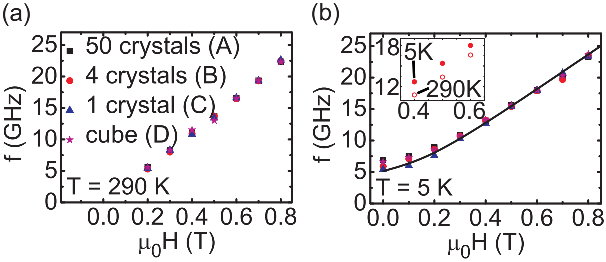

Figure 7.5.: The field dependent resonance frequencies at room temperature (a) and at T = 5 K (b). The black line is a fit to the data using the theoretical model described in the text. The inset of (b) shows the shift of the resonance frequencies when changing the temperature for sampe B.

fitting parameters. Good agreement of calculated and measured field dependency is found for $\mu_0 H_{\text{ani}} = -0.09$ T, $\mu_0 H_{\text{sur}} = 0.144$ T. The angle of the external magnetic field with respect to the anisotropy axis was set to $\theta_{\text{H}} = 23°$. We get almost perfect agreement between the calculated black line and the experimental values. Note should also be taken of the excellent agreement of the effective anisotropy field of 0.234 T (sum of the absolute values of the volume and surface anisotropy field) with the experimental value of 0.236 T.

7.1.2. Linewidth and Damping

It is now instructive to study the damping of the different samples. First we extract the linewidth Δf from the spectra by fitting a Lorentzian curve to the measured data. From this we obtain the linewidth of the magnitude, which can be translated into the linewidth of the imaginary part by taking $\Delta f/\sqrt{3}$ [Sta09]. These values are summarized in Fig.7.6 (a) for all four samples.

We see that the linewidths of samples A and B are higher compared to samples C and D. Using $\alpha_{\text{eff}} = \Delta\omega/2\omega = 2\pi\Delta f/2\omega$ at $f \approx 15.6$ GHz, we obtain an effective damping parameter α_{eff} of 0.155 for samples A and B and 0.135 for samples C and D [Fig. 7.6 (b)]. We assume that the linewidth consists of an intrinsic contribution [$\Delta\omega_{\text{intr}} = 2\alpha_{\text{intr}}\omega$] and an extrinsic contribution $\Delta\omega_{\text{ext}}$ and that these two contributions add in the same manner as in chapter 3.4. Fitting a linear curve to the data points

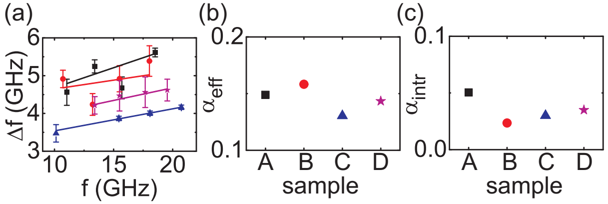

Figure 7.6.: (a) Experimental values of the frequency dependent linewidth Δf (symbols) and the respective linear fits (lines). (b) Effective damping parameter α_{eff} at $f \approx 15.6$ GHz. (c) Intrinsic damping parameter α_{intr} as determined from the slope of the frequency dependent linewidth.

in Fig. 7.6 (a), we extract the intrinsic damping term α_{intr} from the slope [Fig. 7.6 (c)]. Note that we restrict our evaluation to the saturated regime. From this we obtain values for α_{intr} of about 0.05 for sample A and 0.03 for samples B, C, and D.

7.1.3. Collective Behaviour and Propagating Spin Waves

As mentioned above, the resonance frequencies have been found to shift to higher values at low temperatures when compared to resonance frequencies at 290 K. In the inset of Fig. 7.5 (b) we have plotted the resonance frequencies for 290 K and 5 K in the saturated state. The frequency shift has been observed earlier on disordered arrays of NPs and interpreted as dynamic coupling of the individual NP via dipole-dipole interaction [Gus07]. In addition, in Ref. [Kas08] the hysteric behaviour of ordered and disordered magnetoferritin NPs has been studied. It has been concluded that interparticle interaction leads to a change in the hysteric behaviour in ordered magnetoferritin NPs.

It is therefore instructive to exploit the hysteretic behavior in the 50 crystals sample using AESWS. In Fig. 7.7 (a), we have sketched a hysteresis curve, which we divide into four segments (I-IV). For a magnetic hysteresis present in the sample, the resonance frequency is expected to depend on the field history. To test this we take difference data shown in Fig. 7.7 (b) for one field value of 60 mT. To obatin the curves in Fig. 7.7 (b) we first saturated the sample at +1.5 T and then took a spectrum at 60 mT, i.e.

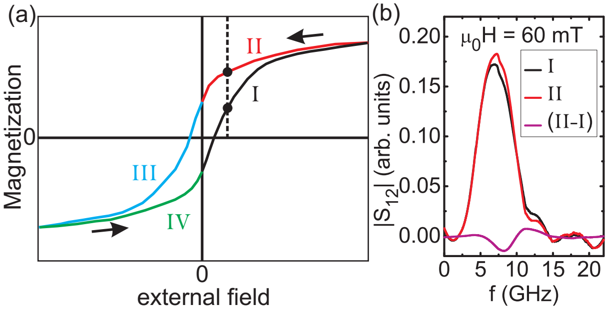

Figure 7.7.: (a) Sketch of the hysteresis curve for magnetoferritin subdivided in four segments. (b) Spectra of S_{12} at the same external field of 60 mT but on different branches of the hysteresis curve, i.e. coming from negative field (I) and coming from positive field (II), as well as the resulting difference curve ΔS_{12}(I) - ΔS_{12}(II).

being on branch II of the hysteresis curve. Then, we saturated the sample at -1.5 T and took a second spectrum at 60 mT (branch I of the hysteresis curve). Substracting both spectra, we obtain a difference signal (magenta curve in Fig. 7.7 (b)). We executed this procedure for different field values and obtained difference curves shown in Fig. 7.8 (a). We see that as we increase the field value the difference signal starts to appear at around 20 mT and as we approach 80 mT the signal starts to vanish again. In order to test if this difference signal is not caused by any drift in the measurement setup we obtain difference signals by substracting measurements at opposing fields, i.e. branch IV and branch II. The obtained difference signals show no variation (7.8 (b)). This suggests a hysteresis curve with point symmetry.

It is now intriguing to study spin wave propagation in magnetofferitin 3D MC. For this we make use of a different CPW exciting a different k-vector (k_2). By this we explore the dispersion relation and therefore the group velocity $v_{\mathrm{g}} = \mathrm{d}\omega/\mathrm{d}k \approx \Delta\omega/\Delta k = \Delta\omega/\left(k_2 - k_1\right)$. In Fig.7.9 (a) we plot the resonance frequencies of one and the same crystal (magnetite) placed on top of two different CPW's. The resonance frequencies differ between CPW1 (k_1) and CPW2 (k_2). Assuming a linear dependency of the dispersion relation in the small wavevector regime, we calculate the group velocity using Eq. 3.20 with $\Delta k = k_2 - k_1 = 0.504 \times 10^4$ rad/cm and

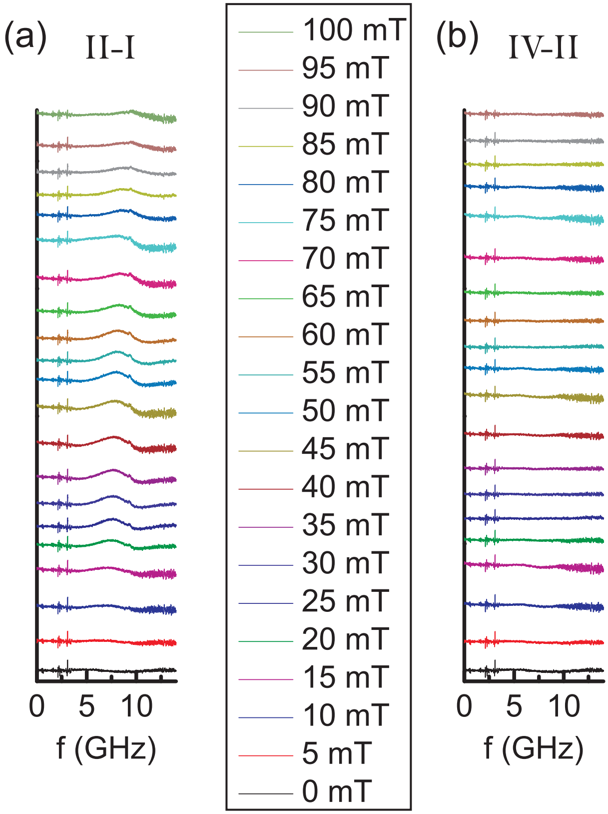

Figure 7.8.: Difference signals obtained from substracting spectra taken at different branches of the hysteresis indicated by the roman numbers. In (a) we substracted the spectra from branch I from II. A difference signal is pronounced between about 20 mT and 80 mT. In (b) we substracted the spectra from branch VI from II taken at the same field. No difference signal is resolved.

$\Delta\omega$ = $\omega(k_1)$-$\omega(k_2)$. In Fig.7.9 (b) we have plotted the group velocities at different field values. The group velocity varies between 7.5 km/s and 12.5 km/s. Using the damping parameter obtained above we obtain the attenuation length L_{att}, i.e. the length over which the precession amplitude decays as $1/e$ (c.f. chapter 3.4). Using Eq. 3.24 together with $\tau = 1/(\alpha_{\text{intr}}\omega)$ we obtain L_{att} = 2.25 μm at f = 15 GHz.

7.2. Co-doped Magnetoferritin

So far we have discussed data at temperatures as low as 5 K and thereby stayed below the blocking temperature. It would be desirable to increase the blocking temperatures of such NP arrays. In order to do so we investigated samples prepared following [Oku12] et al. For this, Co was added to increase the blocking temperature of magnetoferritin crystals. Here, we report dynamic properties of such Co-doped magnetoferritin.

In Fig.7.10 (a), we show spectra taken at 290 K on a crystal with 0$\%$ Co, a crystal with 1$\%$ Co, and a crystal with 2.5$\%$ Co[1]. We observe an increase in the linewidth as the Co content increases. Adding one percent of Co leads to a linewidth broadened by a factor of 3 compared to the linewidth of the undoped sample, i.e. a linewidth of 6 GHz. Increasing the Co content further increases the linewidth to values above 8 GHz. Note that the resonance frequencies themselves do not vary much in contrast to the linewidths. The extracted linewidths for the three samples are plotted in Fig.7.10 (b). The linewidth was found to increase even further for decreasing temperature such that we were not able to resolve a resonance below the blocking temperature.

7.3. Discussion

The fact that the resonance frequencies of all NP arrays agree well is a remarkable result. Not so much because we have studied two different materials, i.e. magnetite and maghemite, as these materials are well known to behave very similar. More fascinating is the fact that even though the geometry, i.e. the external shape, of the samples was chosen to be very

---

[1] We use the notation $x\%$ Co to refer to apoferritin containing magnetite nanoparticles synthesized with $x\%$ molar ratio of Co.

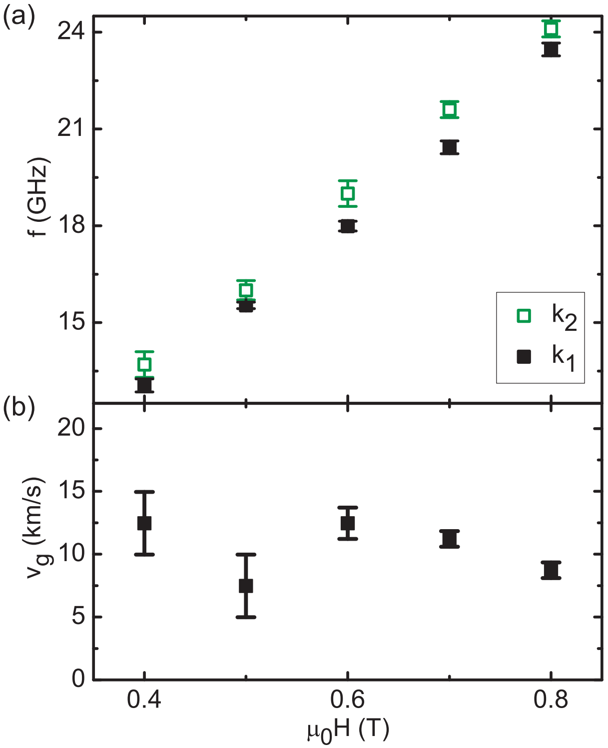

Figure 7.9.: (a) Resonance frequencies measured on one and the same sample using two different CPWs resulting in two different k-vector values. The filled squares are obtained using a CPW with a maximum excitation strength at $k_1 = 0.096 \times 10^4$ rad/cm, whereas open squares are obtained with a CPW having maximum excitation strength at $k_2 = 0.6 \times 10^4$ rad/cm. (b) Calculated group velocities as determined by the frequency difference of the two datasets.

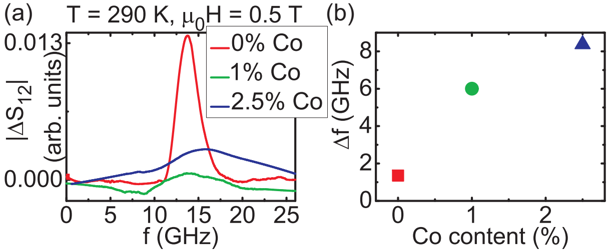

Figure 7.10.: (a) Typical lineplots of S_{12} of Co-doped magnetoferritin crystals at T = 290 K. (b) The linewidth Δf as a function of Co-content in magnetoferrtin.

different, the eigenfrequencies do not change considerably. In ferromagnetic resonance experiments shape anisotropy caused by demagnetization fields have a strong influence on the resonance frequency [Gie05, Gub07, Kos08b]. In our measurements we find the resonance frequencies to vary a bit in the low field regime, i.e. the unsaturated regime below 0.4 T, but at higher fields the frequencies of the different samples agree well. Note that any effect from demagnetization fields, i.e. shape anisotropy, would change the resonance frequencies over the whole field range. We also want to mention that the measurements are repeated several times and with different crystals (not shown) and we always find the same resonance frequencies, which is clear evidence of a very stable and repeatable preparation process.

In our calculations to model the field dependency of the resonance frequencies, we have used an effective anisotropy term K_{eff}. Since magnetic anisotropy of individual NP has been reported in many publications it can safely be assumed to be present in the magnetoferritin crystals studied here. Especially the contribution of surface anisotropy has been shown to be quite significant in spherical NPs, but depends on the size of the NPs. Here, three types of surface anisotropies have been reported, i.e. Néel type, Aharoni type, and spin-glass shell [Gar03, Gaz98, Per05, Yan09, Yan07]. We point out that we have neglected any dynamic coupling between individual NPs as the theoratical curve is obtained for isolated NPs. The dynamic coupling might however modify the magnetic parameters K_{eff} and M_{s} such as in a metamaterial [Neu11c].

Another interesting question is the alignment of the uniaxial anisotropy of individual NPs with respect to the fcc crystallographic structure. We assume that this mainly depends on the conditions during formation of the crystals and that even if there is some alignment it would be with some distribution. We point out that independenlty on the orientation of the anisotropy axis, the anisotropy field of a given NP does not influence the resonance of another particle, i.e. it is a local property of each NP. The extracted ferromagnetic linewidth (around 4.5 GHz) showed the common behavior for ferromagnetic materials, but is about an order of magnitude larger if compared to other common materials like Py and CoFeB (around 400 MHz). Considering that the extrinsic linewidth contribution of the CPW used here amounts to approximately 200 MHz we expect additional contributions to the linewidth to be present. This could be coming from slightly different resonance frequencies of different NPs, which can be caused by size variations of NPs or a spread of misalignment angles of anisotropy axes with respect to the external field direction. Nevertheless, we could argue that spin wave propagation is possible in such 3D MCs even over several micrometer, which is comparable to the propagation length of other common ferromagnetic materials.

In summary we have studied dynamic excitations in 3D arrays of NPs formed by crystalization of magnetoferritin. The excitation characteristics are repeatable even for different external geometries of the MC. By using FIB processing a crystal was shaped as a cube without modifying the dynamic response significantly. This offers the possibility to tailor crystals in any way required by experiments or applications. We have applied a theoretical model developed by M. Krawczyk in order to describe the field dependencies of such crystals using an effective anisotropy of individual NPs. Furthermore, we showed that these crystals support spin-wave propagation over a few micrometers, which is key for magnonic crystal device as it offers the possibility to transmit information. Still the attenuation length needs to be improved.

8. Skyrmion Crystals

In this chapter we report on helimagnon and skyrmion excitations in metallic, semiconducting and insulating chiral magnets. Here, we study bulk samples of MnSi, $Fe_{1-x}Co_xSi$ and Cu_2OSeO_3 across the magnetic phase diagram. In the first part of this chapter we present measurements using AESWS. We evaluate the field dependent resonance frequencies as well as the linewidth, thereby addressing the damping of the spin precessional motion. In the second part, we compare our results with theoretical predictions for the excitation frequencies elaborated by the group of Prof. A. Rosch as outlined in chapter 2.5. Taking into account the sample geometry, i.e. the appropriate demagnetization fields, we obtain very good quantitative agreement between measured frequencies and the predicted excitation frequencies for all samples studied. The single crystal samples of $Fe_{1-x}Co_xSi$ and MnSi studied here were grown by optical float zoning under UHV compatible conditions in the group of Prof. Christian Pfleiderer at TUM [Neu11a]. For our study, the samples were cut from the ingot with a wire saw. High quality single crystals of Cu_2OSeO_3 were grown by the standard chemical vapor phase method and provided by H. Berger of EPFL Lausanne in Switzerland. More details about the crystal growth can be found in Ref. [Bel10].

8.1. GHz Excitations in Chiral Helimagnets

The magnetism and excitations in the helimagnetic B20 compounds are characterized by a well understood hierarchy of energy scales. The strongest energy scale is the magnetic exchange J that aligns the spins ferromagnetically on short distances. A weak spin-orbit Dzyaloshinskii-Moriya exchange D however, twists the magnetization on longer length scales giving rise to modulated chiral magnetic textures with typical momenta $Q \sim D/J$. Finally, these textures are aligned along crystallographic high symmetry directions by cubic anisotropies that constitute the weakest energy scale as it is proportional to higher-orders of spin-orbit coupling. This hierarchy of energy scales is at the origin of the universality of magnetic properties shared by the B20 materials, and in particular, permits a common account of their spin excitations. This clear separation of scales is also reflected in the magnetic phase diagram, which we introduced in chapter 2.5 (c.f. Fig. 2.5) as observed in bulk samples of all known helimagnetic B20 compounds.

First, we study dynamic excitations of three bulk samples of MnSi, $Fe_{1-x}Co_xSi$ and Cu_2OSeO_3 in a flip-chip geometry, i.e. the samples are placed directly on top of the CPWs. The three samples and their geometry as well as the respective demagnetization factors are summarized in Table 8.1. For the width of the inner conductor of 20 μm used in our study the main excitation arises at $k_{\mathrm{CPW}} = 0.094 \cdot 10^4\,\mathrm{rad/cm}$. The corresponding wavelength ($\lambda_{\mathrm{CPW}} = 10.6\mu$m) is therefore much larger as compared to the intrinsic scales of the helimagnetic state (typically ranging from several 10 to 1000 Angstroms for different systems). In the following, we assume to operate in the long-wavelength-limit close to $k = 0$.

We start our investigation with a MnSi sample cut out (thickness of 1 mm) from a MnSi single crystal putting the flat side ($\langle 100 \rangle$ plane) on top of the CPW. In Fig. 8.1 (a) we show the magnitude of ΔS_{ij} measured on MnSi at 5 K in a gray-scale plot. The dark color means absorption of the microwave signal, i.e., magnetic resonance. For increasing H, the resonance frequency first decreases starting from slightly above 26.5 GHz at $H = 0$. At $\mu_0 H = 0.7$ T, the resonance frequency f exhibits a minimum with $f \approx 17$ GHz (white dashed line). Following the phase diagram of MnSi [Bau12] the minimum at 0.7 T is attributed to the phase transition, where the crystal changes from the conical to the ferromagnetic phase. Beyond 0.7 T, the resonance frequency increases almost linearly with H. At 27.5 K [Fig. 8.1 (b)], the branch starts at a smaller resonance frequency f of 18 GHz at $H = 0$ and exhibits a negative slope for the conical phase up to the phase transition field of now $\mu_0 H = 0.5$ T. For larger H, the frequency increases in a similar way as observed in Fig. 8.1 (a) beyond 0.7 T. The almost linear slope is again attributed to the ferromagnetic or so-called field-polarized phase. A detailed inspection of Fig. 8.1 (b) however reveals a further resonance of weak intensity at about 10 GHz and 0.2 T (marked by an arrow). At the same field, the intensity of the upper branch is reduced. The measurements performed with finer field steps between 0.1 and 0.3 T [Fig. 8.1 (c)] prove the excitation at small frequency. At 0.2 T, there is a coexistence of two excitations, but at 0.22 T and 0.24 T the formerly pronounced upper branch has vanished completely. We attribute the

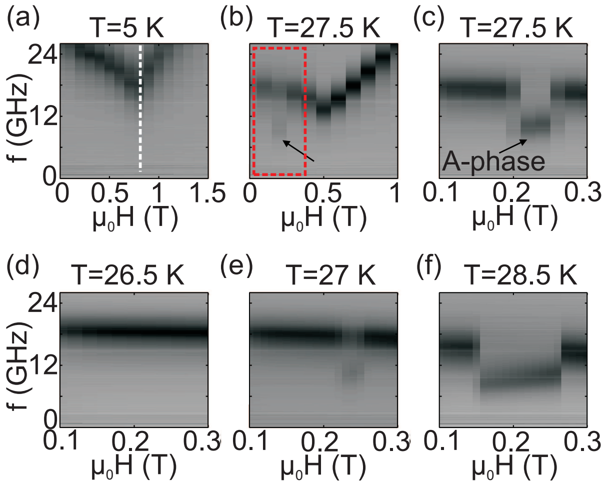

Figure 8.1.: ΔS_{21} measured on MnSi at (a) 5 and (b) 27.5 K with a field step size of 0.1 T. Dark color indicates resonant absorption, i.e. spin excitation. In (a) the white dashed line marks the field position of the phase transition from conical to ferromagnetic phase. In (b) the arrow highlights an additional low frequency excitation at about 10 GHz observed for $T = 27.5$ K. The step-like variation of f at $\mu_0 H \geq 0.5$ T is due to the discrete field steps. (c) ΔS_{12} taken at 27.5 K with a field-step size of 0.02 T, i.e., a detailed investigation of the field regime indicated by the broken lines in (b). The low frequency excitation is attributed to the skyrmion phase following the phase diagram of MnSi. (d) Spectra ΔS_{12} taken at (d) 26.5, (e) 27.0 and (f) 28.5 K illustrating the temperature and field dependencies of the A-phase as observed with GHz spectroscopy.

low frequency excitation to the skyrmion phase (A-phase) formed in this field regime. The field dependency of this skyrmion excitation is opposite to that of the conical phase as the frequency is found to increase with field. At 0.26 T, two branches co-exist again. For larger H, the upper branch of the conical phase is present, still exhibiting the negative slope as a function of increasing H.

Excitations in the skyrmion phase are depicted for further temperatures T in Fig. 8.1 (d) to (f). The experiments show that at only above 26.5 K, the intermediate skyrmion phase appears [Fig. 8.1 (e) to (f)] in a specific field regime. The width of the regime depends on T. At 28.5 K, it extends

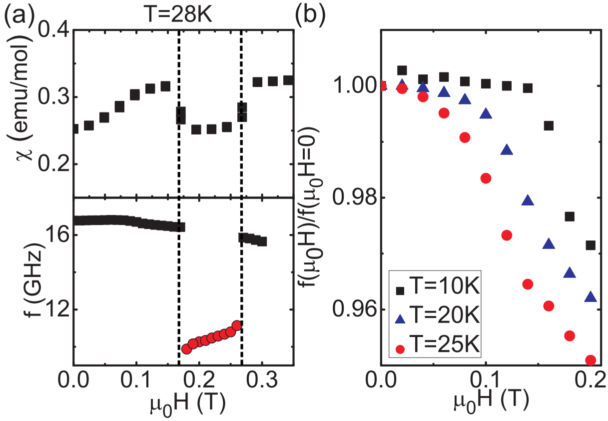

Figure 8.2.: (a) Field-dependence of the magnetic susceptibility χ of MnSi (top) compared to eigenfrequencies of prominent modes (bottom) extracted from spectra at 28 K. Excitations measured in the skyrmion phase are shown as red circles. (c) Field dependency of eigenfrequencies at small $\mu_0 H$ for three different T that demonstrate the helical-conical phase transition.

already over more than 0.1 T. The temperature dependent behavior is consistent with the field and temperature regimes covered by the A-phase in the phase diagram. As an example, we show susceptibility measurements for MnSi for the respective field and temperature regime in Fig. 8.2 (a), where we compare the field dependence of the magnetic susceptibility χ measured in a separate experiment with the variation of the excitation frequency f between 0 and 0.35 T at 28 K. Discontinuities appearing in χ and f take place at the same field positions, i.e., at 0.185 and 0.26 T. The data $\chi\,(T, H)$ was taken by A. Bauer at TUM.

In Fig. 8.2 (b), we show resonance frequencies $f(H)$ measured at small H and normalized to $f(0)$ at different temperatures $T=$ 10, 20, and 25 K. We observe that $f(H)/f(0)$ stays nearly constant at small H and then decreases with increasing field. For $T=10$ K, the nearly constant behavior is found over a broad field regime ranging from zero to about 0.15 T. We attribute the characteristic change in slope of $f(H)/f(0)$ to the phase transition from the helical to the conical phase.

Now we extend our investigation to $Fe_{1-x}Co_xSi$ and Cu_2OSeO_3. The samples are placed on top of the same CPW. In Fig. 8.3 (a-l) we show typical frequency dependencies of ΔS_{21} in MnSi, Fe$_{1-x}$Co$_x$Si and Cu$_2$OSeO$_3$ at a fixed temperature for each magnetic phase. Data were recorded for the field along the hard magnetic axis to minimize the influence of anisotropies on the excitation spectra, where field values stated in each panel refer to the applied magnetic field. The colored lines serve as a guide to the eye (the raw data including noise is shown in gray). For all materials, the data ΔS_{21} recorded within the magnetically ordered phases is dominated by a broad minimum as marked by an arrow. A close inspection of the MnSi spectra at 0.18 T and 0.19 T shows that slightly above the transition field of 0.185 T, in fact, two resonances exist (Fig. 8.3 (b)). The prominent low-frequency mode at 9.8 GHz that was prominent in the gray-scale plots of Fig. 8.1 contains a pronounced shoulder on the high-frequency side. This shoulder indicates a further resonance at about 19 GHz. Note that this resonance frequency is at a slightly larger frequency compared to f, which would be expected for the conical phase if it was to exist at 0.19 T. The increased frequency suggests that beyond 0.185 T the high-frequency mode (shoulder) is of a different microscopic origin compared to the already discussed excitations. This second excitation is visible throughout the field regime where skyrmion excitations take place and stay more or less constant as a function of field. For MnSi in the skyrmion phase, two separate modes have already been predicted and observed by Mochizuki et al. [Moc12] and Onose et al. [Ono12], so that we can safely assume to observe this second mode as well.

Summarized in Fig. 8.3 (m), (n) and (o) are the excitation frequencies as a function of applied magnetic field for MnSi, Fe$_{1-x}$Co$_x$Si and Cu$_2$OSeO$_3$, respectively. For each material field-sweep data is shown for at least two temperatures, one well below the respective T_c and the other close to T_c crossing the skyrmion lattice phase. Perhaps most remarkable is the wide frequency range over which the excitations are observed when comparing the different materials, extending over nearly an order of magnitude. Nevertheless, for all three materials, the field dependencies of the excitation frequencies are qualitatively similar despite the vastly different quantitative values. Distinct changes of frequency coincide with the phase boundaries as determined for the same samples in measurements of the AC susceptibility.

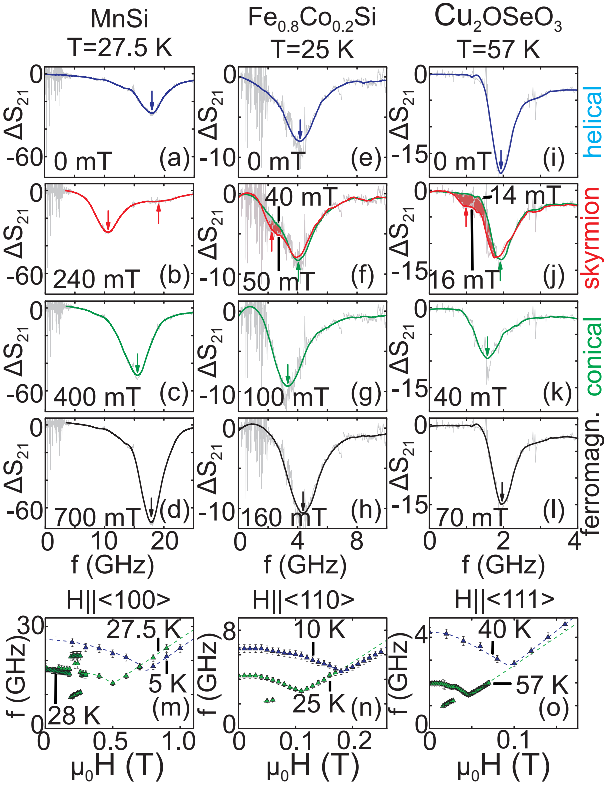

Figure 8.3.: (a-l) Spectra of ΔS_{21} of MnSi, $Fe_{1-x}Co_xSi$ and Cu_2OSeO_3 at various magnetic fields. An averaged curve has been added as a guide to the eye. The plots are subdivided into the different magnetic phases found in chiral helimagnets, i.e. helical, conical, skyrmion, and ferromagnetic phase. At fields where the respective phase transition is better observed by plotting consecutive measurements we show two lineplots. Characteristic resonance frequencies are marked by an arrow. (m-o) Summary of excitations for all three materials at different temperatures. Note the differences in the frequency scale.

8.2. Linewidth and Damping

Next, we evaluate the linewidth. As in the previous chapter, we extract the linewidth from the magnitude of ΔS_{12} and calculate from this the linewidth of the imaginary part. We will focus here on the metallic MnSi sample and the isolating Cu_2OSeO_3 sample. First, we study the linewidth in the field-polarized phase, as we are able to compare these values with values found in common ferromagnetic materials.

We start by plotting the linewidth of MnSi and Cu_2OSeO_3 over the frequency for different temperatures(Fig. 8.4 (a-b)), where we observe an increase in linewidth with increasing frequency. This is consistent with the behaviour observed in common ferromagnets, as demonstrated in other chapters of this work (c.f. chapter 3.4, 5.1, and 7.1). The temperature dependency of the linewidth for MnSi and Cu_2OSeO_3 is shown in Fig. 8.4 (c-d). For MnSi, the linewidth decreases for increasing temperature before leveling off at around 25 K. For Cu_2OSeO_3, the linewidth stays nearly constant at low temperatures and starts to decrease from approximately 30 K. In Fig. 8.4 (c-d) (right y-axis) we also show $\alpha_{\text{eff}} = \Delta\omega/(2\omega)$, which basically follows the same dependency as the linewidth. It is worth noting that the linewidth of MnSi is about four times larger when compared to Cu_2OSeO_3, whereas α_{eff} is comparable for both materials at around 0.06 to 0.1. In Fig. 8.4 (e-f) we show the values of α_{intr} versus temperature as extracted from the slope of the linewidth versus frequency. For Cu_2OSeO_3 we find $\alpha_{\text{intr}} \approx 0.011$ and for MnSi we find α_{intr} to vary between 0.082 and 0.032.

Next, we evaluate the linewidth for the other phases found in MnSi and Cu_2OSeO_3. The signal strength and the signal-to-noise ratio allows us to explore all phases in MnSi, whereas we are not able to evaluate the skyrmion phase in Cu_2OSeO_3. Starting with MnSi, we show the field dependency of the resonance frequency in the helical-, the conical-, and the skyrmion phase in Fig. 8.5 (a) for all temperatures evaluated hereafter. The field dependent linewidth Δf and effective damping α_{eff} are plotted in Fig. 8.5 (b) and (c) respectively. At low fields, the linewidth stays nearly constant before at around 100 mT, where it starts to either increase (20 - 28 K) or decrease (15 K) slightly. For 28 K we observe an abrupt increase in linewidth at an external field of 190 mT. From 190 mT to 260 mT, the linewidth decreases before reaching the same level as for small fields. The field regime from 190 mT to 260 mT coincides with the skyrmion phase. It

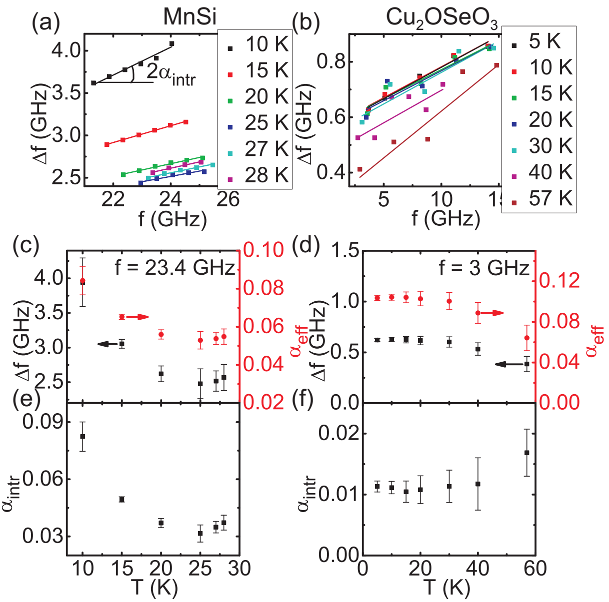

Figure 8.4.: Field-polarized phase: frequency dependent linewidth Δf obtained from (a) MnSi and (b) Cu_2OSeO_3. Temperature dependencies of Δf and the effective damping parameter α_{eff} for (c) MnSi and (d) Cu_2OSeO_3. The intrinsic damping parameter α_{intr} as evaluated from the slope in (a) and (b) are shown for (e) MnSi and (f) Cu_2OSeO_3.

is interesting to inspect the temperature dependency at a constant field (inset of Fig. 8.5 (b)). From 15 K to 20 K, the linewidth decreases before the linewidth increases for 27 and 28 K. This can also be seen in the frequency dependent linewidth plot in the helical/conical phase in Fig. 8.5 (d). Note that at T = 27 and 28 K, the skyrmion phase is present. Furthermore, in the inset of Fig. 8.5 (d) we show the dependency at T = 20 K. Here, initially the linewidth stays nearly around the same value of 2.05 GHz. Then as the frequency slowly starts to decrease, the linewidth also decreases until the linewidth starts to increase. This beahvior is obeserved for all temperatures except for T = 15 K, where the linewidth does not show a very clear increase towards lower frequencies. The strong frequency and linewidth change can be assigned to the conical phase. In Fig. 8.5 (e) we also show the frequency dependency of α_{eff}. The frequency dependency of Δf and α_{eff} in the skyrmion phase is shown in Fig. 8.5 (d) and (e) on the left side of the graphs. Besides the increase in absolute values, the linewidth as well as the damping parameter strongly decrease for increasing frequencies. Note that the field dependency of the resonance frequency is opposite in the skyrmion phase and the helical/conical phase.

For Cu_2OSeO_3, we start by evaluating the linewidth Δf and the effective damping α_{eff} at different temperatures and fields. In Fig. 8.6 (a), we first show the field dependent resonance frequencies for seven temperatures ranging from 5 K to 57 K. In Fig. 8.6 (b) and (c), we show the field dependencies of the linewidth in the helical/conical phase. Looking at Δf at zero field (see also inset of Fig. 8.6 (b)) we observe a decrease in linewidth for increasing temperature. Only at T = 57 K the linewidth increases and even exceeds the value at the lowest temperature of 15 K. Note that T = 57 K is the temperature where the skyrmion phase is present.

Further, we observe that the linewidth increases with increasing field for all temperatures. Note that the values for α_{eff} shown in Fig. 8.6 (c) are just slightly below the values found for MnSi. The frequency dependency of Δf and α_{eff} is shown in Fig. 8.6 (d) and (e), respectively. For all temperatures we observe a decrease in linewidth for increasing frequency.

We want to mention that for both materials we are not able to extract α_{intr} in the helical-, the conical-, and the skyrmion phase because the frequency dependent linewidth is opposite to the one in the field-polarized phase.

8.3. Universal Theory of Collective Spin Excitations in Chiral Helimagnets

All three studied materials differ in the critical temperature T_c and the pitch Q, see Table 8.1. Nevertheless, the common character of the magnetism together with the underlying hierarchy of energy scales intrinsic to each material allows to describe their microwave excitations in a universal manner. For the quantitative interpretation of our data, it is important to go beyond previous work [Kat87, Moc12] and to include dipolar interactions and the demagnetization factors N_i with $i = x, y, z$. As introduced in chapter 2.5 in the field-polarized phase $H > H_{c2}$, one obtains the standard ferromagnetic resonance condition as described by the Kittel formula.

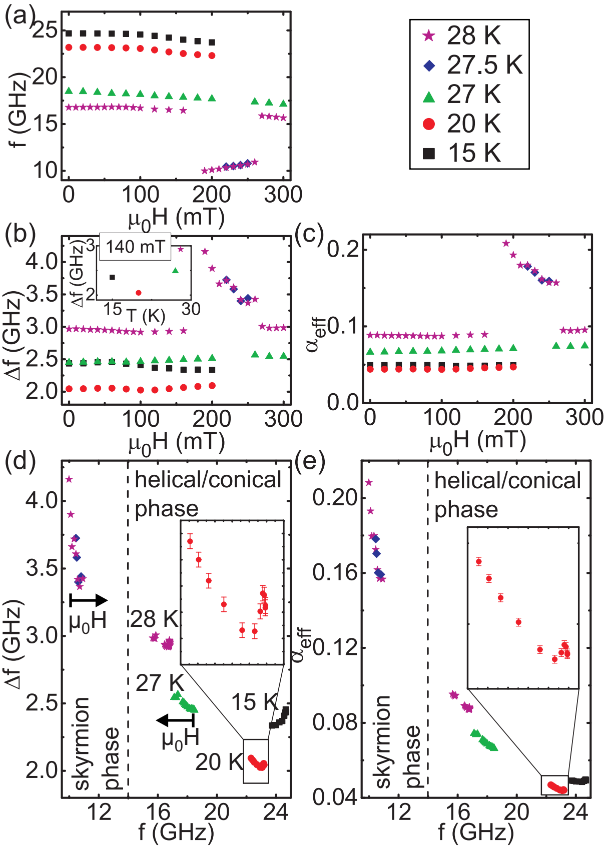

Figure 8.5.: Helical-, conical-, and skyrmion phase: field dependency of the measured resonance frequencies (a). Field dependent linewidth Δf (b) and effective damping parameter α_{eff} (c) for MnSi. The inset in (b) shows the temperature dependent linewidth at a constant field of $\mu_0 H$ = 140 mT. Δf (d) and α_{eff} (e) as a function of frequency. Black arrows indicate the field direction for constant temperature.

At intermediate field $H_{c1} < H < H_{c2}$ where cubic anisotropies are negligible, we find that the magnitude of the excitation frequencies is determined by the temperature dependent critical field $H_{c2}(T)$. The precise

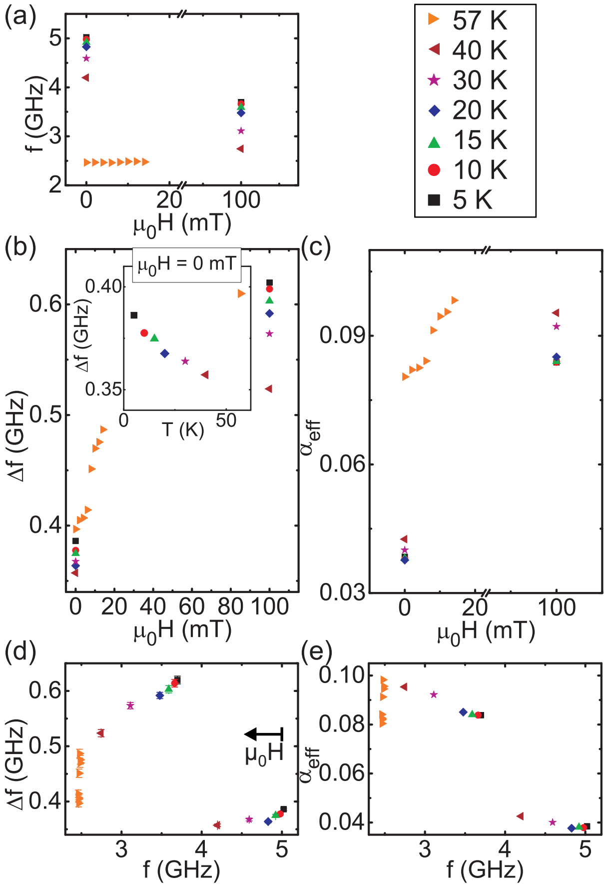

Figure 8.6.: Helical- and conical phase: field dependency of the resonance frequencies (a). Field dependent linewidth Δf (a) and effective damping parameter α_{eff} (b) for Cu_2OSeO_3 at various temperatures. The inset in (b) shows the temperature dependency of the linewidth at zero field. Δf (d) and α_{eff} (e) as a function of frequency in the helical and conical phase. Black arrow indicates the field direction for constant temperature.

magnetic field-dependence and the frequency splitting of the two modes however depends on the demagnetization factors of the samples as well as

Material	T_c	H_{c2}^{int}	$2\pi/Q$	$\chi_{\mathrm{con}}^{\mathrm{int}}$ (T=0)	N_x	N_y	N_z
MnSi	29 K	0.6 T	180 Å	0.34	0.18	0.18	0.64
$\mathrm{Fe}_{1-x}\mathrm{Co}_x\mathrm{Si}$	58 K	0.13 T	340 Å	0.65	0.08	0.46	0.46
$\mathrm{Cu_2OSeO_3}$	27 K	0.1 T	600 Å	1.76	0.39	0.27	0.34

Table 8.1.: Parameters of the chiral magnets investigated: critical temperature at zero field T_c, critical internal field in the low-temperature limit, the pitch Q and the internal magnetic susceptibility within the conical phase $\chi_{\mathrm{con}}^{\mathrm{int}} = \partial M/\partial H_{\mathrm{int}}$ where H_{int} is the internal field, and the g-factor. The demagnetization factors of the specific shapes of the samples are given in the last three columns. The static field H was always applied along the principal z-axis so that $\chi_{\mathrm{con}}^{-1} = (\chi_{\mathrm{con}}^{\mathrm{int}})^{-1} + N_z$ holds with $\chi_{\mathrm{con}} = \partial M/\partial H$.

on a single material parameter, i.e., the constant magnetic susceptibility $\chi_{\mathrm{con}} = \partial M/\partial H$ within the conical phase. An analytical expression for the excitation frequencies within the conical phase is given in chapter 2.5.

For the benefit of the reader, we replot the results found in chapter 2.5 for a sphere in Fig. 8.7 (a). For the quantitative comparison we renormalized the observed frequencies, shown as triangles in Fig. 8.7 (b)-(d), by the respective T-dependent critical field energy $g\mu_0\mu_{\mathrm{B}}H_{\mathrm{c2}}(T)$ where g is the g-factor of the materials. Following this normalization procedure, the eigenfrequencies taken at different temperatures and in different phases follow the universal behavior as a function of H/H_{c2} that is predicted by the theory. The theoretical expected position and weight of modes are shown as circles for which the demagnetization factors and the material parameter $\chi_{\mathrm{con}}^{\mathrm{int}}$ of the materials were taken into account, see Table 8.1. The static magnetic field was aligned along the principal z-axis and the AC field pointed along the principal x-axis of the sample. The sample shapes correspond to an approximate disc, bar and cuboid for MnSi, $\mathrm{Fe}_{1-x}\mathrm{Co}_x\mathrm{Si}$ and $\mathrm{Cu_2OSeO_3}$, respectively. Within the conical phase we were not able to detect two distinct modes with our measurement setup, whereas in the skyrmion phase of MnSi, both gyration modes are resolved in $\mathrm{Fe}_{1-x}\mathrm{Co}_x\mathrm{Si}$ and $\mathrm{Cu_2OSeO_3}$ only the one with the larger weight is detected.

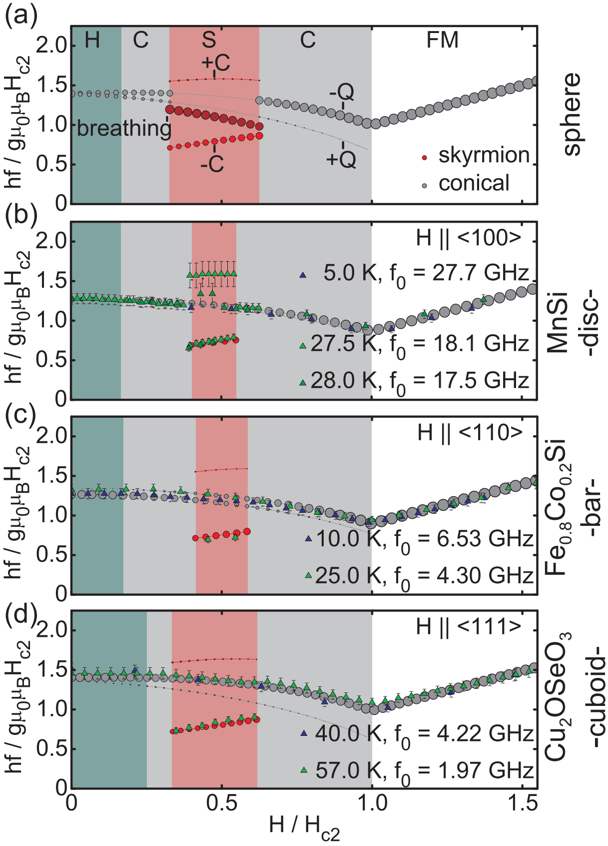

Figure 8.7.: (a) Excitations predicted by the theoretical model of a spherical specimen. The color shaded regions illustrate the field regime, where the respective phases are expected. (b-d) Comparison between experimental (triangles) and theoretical (circles) data for (b) MnSi, (c) $Fe_{1-x}Co_xSi$, and (d) Cu_2OSeO_3 for various temperatures after normalization and considering the geometrical shape of the samples with the respective theoretical predictions.

8.4. Discussion

We have studied excitation frequencies in three helimagnets, i.e. metallic MnSi, semiconducting $\mathrm{Fe}_{1-x}\mathrm{Co}_x\mathrm{Si}$, and insulating $\mathrm{Cu_2OSeO_3}$, through their whole phase diagrams. We find different absolute values for the excitation frequencies in the three systems ranging from 3 GHz up to 26 GHz. Intruigingly, if normalized to their specific T-dependent critical fields and accounting for the geometry of the sample, the data fall onto universal curves. We find excellent quantitative agreement between experiment and theory. Apart from the demagnetization factors of the sample shapes, the excitation frequencies and their weights are determined by a single material parameter, the susceptibility $\chi_{\mathrm{con}}^{\mathrm{int}}$ within the conical phase. It quantifies the strength of the dipolar interaction in each material, and it is determined by the ratio of magnetic and Dzyaloshinski-Moriya energy, $\chi_{\mathrm{con}}^{\mathrm{int}} = \mu_0\mu^2/(JQ^2)$, where μ_0 is the magnetic constant and μ is the magnetization density. Due to the hierarchy of energy scales, further corrections attributed to the cubic anisotropies are negligible for $H > H_{c1}$. Such corrections become only important for a detailed quantitative description of the resonances within the helical phase at smaller fields $0 \leq H < H_{c1}$. With this we could proof the universal character of the theory outlined in chapter 2.5.

Furthermore, we have studied the linewidth, i.e. the damping, in MnSi and $\mathrm{Cu_2OSeO_3}$. In the field polarized phase, we find the same frequency dependency of the linewidth for both MnSi and $\mathrm{Cu_2OSeO_3}$ as in ferromagnetic materials. Therefore, we are able to extract the intrinsic damping parameter α_{intr}. We find α_{intr} to be larger in MnSi if compared to $\mathrm{Cu_2OSeO_3}$. Although the absolute values of the linewidth were found to differ by a factor of 3, the values of the effective damping term α_{eff}, which scales with frequency, is of the same order for both materials. The temperature dependency of the linewidths are found to be different for MnSi and $\mathrm{Cu_2OSeO_3}$. For the metallic MnSi sample, we find that the temperature dependency of the damping compares to the situation in metallic Ni, Fe, and Co systems, where the competition between interband and intraband contributions lead to the following dependency [Gil10]: At low temperatures, the intraband contribution is dominant leading to an increase in damping towards lower temperatures. At higher temperatures, the interband contribution takes over leading to an increase in damping towards higher temperatures. For the insulating $\mathrm{Cu_2OSeO_3}$, the observed temperature dependency of the linewidth is comparable to the temperature dependency of insulating YIG (Yttrium-Iron-Garnet), where the FMR linewidth ΔH[1] scales with $1/M_\mathrm{s}$ [Vit85]. This relationship leads to only small variations of the linewidth at low temperatures.

For the helical-, the conical-, and the skyrmion phase, we evaluated the linewidth dependencies for both materials. In general, their linewidth dependencies on the field and on the frequency were comparable. We found that in both materials, the linewidth decreases with increasing temperature when the skyrmion phase is not present. When the skyrmion phase is allowed to form at a specific temperature the linewidth of the helical/conical phase exhibits a significantly increased value.

---

[1] $\Delta H \propto \Delta f$[Kal06]

9. Summary and Outlook

In this thesis we have studied 2D and 3D magnonic crystals and GHz excitations in chiral helimagnets using all-electrical spin-wave spectroscopy and micromagnetic simulations. In the following, we give a summary of the key results obtained within the framework of this work. In the end, we share our thoughts on how to carry on with the results obtained within this thesis.

Summary

In chapter 5 we examined different materials for their advantages and disadvantages for MSFVW experiments. We compared Py to CoFeB and found CoFeB to exhibit a faster spin wave group velocity, which is desirable for propagation measurements. On the other hand side, CoFeB needs higher out-of-plane fields in order to turn the magnetization in the out-of-plane direction. Besides Py and CoFeB, we presented first measurements of perpendicular magnetic anisotropy samples (PMA), i.e. thin multilayers of Co and Ni, which showed very good dynamic properties. As PMA materials exhibit an out-of-plane magnetization even at zero magnetic field, these materials could be interesting for real MC device applications in zero or small external fields. The group velocity of PMA was found to be 3 times as high as in CoFeB and 6 times higher than in Py. On the contrary, PMA showed an increased damping if compared to the other two materials.

In 2D systems of regular ADLs in chapter 6 we demonstrated the possibility to create complete band gaps, i.e. forbidden frequency gaps, in the dispersion relation of spin waves. We have introduced line defects in a magnonic crystal to create wave guide devices. We could show that this is a very efficient way of transmitting spin waves through a MC with higher group velocities than a simple magnetic stripe of the same width. We demonstrated that it is possible to guide spin waves around corners. Our approach does not need additional currents and the propagation length is not altered by introducing a corner if compared to a regular ADL. With the studies on guiding of spin waves through line defects in such MCs we are one step closer towards an all magnonic device, where efficient guiding in arbitary directions is a necessity. Furthermore, we studied a spin-wave splitter device, that has the potential to be used as an interferometer. All 2D devices have been prepared by optical- and focused ion beam lithography within the framework of this thesis. The experimental results using AESWS are compared to and confirmed by micromagnetic simulations.

In chapter 7 we explored 3D magnonic crystals formed by a bio-engineered method of self assembled magnetoferritin nanoparticles. We modeled the field dependent resonance frequencies by taking the surface and bulk anisotropy of the single nanoparticles into account. Intruigingly we showed that spin wave propagation throughout the crystal is possible as the nanoparticles are coupling dynamically. This is key for any magnonic crystal device as it offers the possibility to transmit information. In addition to the as-prepared magnetoferritin crystals, we studied the possibility to cut out a cubic sample using focused ion beam. We found that the additional process step does not alter the dynamic properties of the NPs. Moreover, we studied the possibility of introducing Co to the magnetite solution, resulting in a higher blocking temperature, but found an increased damping. The reason for this cannot be determined by our measurements, but might be due to size variations of the NPs or the anisotropy axis distribution among the different NPs.

In the last part of this thesis (chapter 8), we studied GHz excitations in chiral helimagnets for three different materials, i.e. metalic MnSi, semiconducting $\mathrm{Fe}_{1-x}\mathrm{Co}_x\mathrm{Si}$, and insulating $\mathrm{Cu_2OSeO_3}$. Although the absolute values of the resonance frequencies differ by almost an order of magnitude between different systems, we found a general dependency. This was explained by a universal theory for chiral helimagnetic materials. In addition, we studied linewidth and damping of MnSi and $\mathrm{Cu_2OSeO_3}$. In the field polarized phase we found the frequency dependency of the linewidth to compare to ferromagnetic materials. This allowed us to extract the intrinsic damping parameter α_{intr} for both materials. The temperature dependency of the linewidth in the field polarized phase in metallic MnSi and insulating $\mathrm{Cu_2OSeO_3}$ is found to reproduce the temperature dependency of ferromagnetic metals and that of insulating YIG respectively. In the nontrivial phases, i.e. the helical-, the conical-, and the skyrmion phase, we found the dependencies of the linewidth and the damping parameter to be different for each phase. Comparing both materials we found the linewidth of MnSi to be 3 times larger compared to Cu_2OSeO_3 in all phases. Considering the different absolute values of the excitation frequencies in both materials we found the effective damping parameter α_{eff} to be comparable among the two materials.

Outlook

Next, we want to give an outlook for the four experimental sections of this thesis. Starting with PMA materials, we believe that the good dynamic properties found in this work are in general promising for future magnonic devices especially where out-of-plane magnetization is desired. As the linewidth and the group velocity are known to be influenced by film quality and thickness in ferromagnetic materials a complete study of different multilayer thickness is necessary to find the best dynamic paramters. After optimization, nanostructuring of such multilayer is going to show how the additional preparational steps influence the dynamic properties of the material.

As mentioned above, we believe that the studied spin wave splitter has the potential to be used as an interferometer device. For this, one has to find a way to influence the phase of the spin wave within one of the two arms of the device in order to get constructive or destructive interference at the output. One way of realizing such a scenario is to use a current carrying wire on top of one of the arms of our device to create a local field and therefore changing the phase of the spin wave as demonstrated by Demidov et al. [Dem09]. Here the additional in-plane field is in the order of 10 mT, which is small compared to the fields applied in out-of-plane measurements. Nevertheless, working close to the anisotropy field of the device could lead to a drastic change in resonance frequency even for such small in-plane fields. For a Py plain film of 22 nm thickness at an out-of-plane field of 1 T[1] an additional in-plane field of 10 mT leads to a change in resonance frequency of about 400 MHz, which is in the same order of magnitude as in Ref. [Dem09]. Another possibility is the integration of a f-MRFM (ferromagnetic resonance force microscope) setup with a magnetic tip [Pig12], which can also create an additional local field in the order of 15 mT. For the same arguments as before, one has to work close to the anisotropy field of the device in order to create a significant

---

[1] The anisotropy field is around 0.93 T.

frequency shift and therefore a phase shift.
Furthermore, in the future, one might also make use not only of the forbidden frequency gaps created by the MC, but also the specific shape of the dispersion relation. Here, photonic crystals have been shown to exhibit remarkable effects on interfaces, like negative refraction, based on the newly created dispersion relation [Joa08].

The combination of bio-assisted methods to create 3D structures on the length scale of the magnetic exchange interaction opens completely new possibilities for the field of magnonics. For future devices it is necessary to increase the blocking temperature of magnetoferritin crystals. Future experiments on magnetoferritin crystals might also include transmission measurements with two CPWs to detect the transmitted signal.

For the chiral helimagnetic systems it would be desirable to compare the linewidth dependencies to theoretical predictions on the damping mechanisms present in such systems. According to our knowledge a comprehensive theory has not been presented up to now. As our measurements have been obtained using a CPW with an excitation around $k \approx 0$, it would be intruiging to address excitations at different k, i.e. using another CPW. With this, one is able to probe the dispersion relation.

Recent results on MnSi thin films show that the skyrmion phase can be stable up to room temperature as observed by Lorentz transmission electron microscopy [Kar11, Kar12]. To study dynamic excitations in such thin films could pave the way for skyrmion devices at room temperature. Here, one could make use of our integrated CPW design to efficiently couple electromagnetic waves to the spin system and study propagating spin waves through the skyrmion lattice. One might also think of manipulating the spin system by a very low spin polarized current as demonstrated in Ref. [Jon10] and study the dynamic response. Future experiments might also include in-plane fields in order to address other modes.

A. Appendix

A.1. List of Abbreviations

Abbreviation	Explicit
AESWS	All-electrical spin-wave spectroscopy
VNA	Vector Network Analyzer
PMA	Perpendicular Magnetic Anisotropy
Py	Permalloy (Ni_80Fe_20)
CPW	Coplanar waveguide
AD	Antidot
ADL	Antidot lattice
MSFVW	Magnetostatic forward volume wave
MC	Magnonic crystal
BZ	Brillouin zone
SEM	Scanning electron microscopy
LD	Line defect
MCWG	Magnonic crystal waveguide
MCB	Magnonic crystal bend
MCS	Magnonic crystal split
FMR	Ferromagnetic resonance
FIB	Focuse ion beam
SW	Spin wave
1D	one dimensional
2D	two dimensional
3D	three dimensional
rf	radio frequency
S-Parameter	Scattering parameter
f-MRFM	ferromagnetic resonance force microscopy

A.2. Electromagnetic Simulation Parameter

A great number of parameters enters the electromagnetic field parameter simulation. Not all of these parameters are known. Parameters are defined with respect to the software Microwave Studio.

Material and geometry parameters:

- Isolator thickness t_{iso} = 10 nm
- Isolator permittivity is set to ϵ_{iso} = 8
- The Py permeability is modeled according to a rf susceptibility with parameters M_s = 800 kA/m, f_r = 6 GHz, saturated along x axis.
- Py thickness t_s = 25 nm and CPW thickness 200 nm
- Boundary conditions: beneath substrate: no transversal electric field. Otherwise: no transversal magnetic field.

Simulation parameters:

- Frequency domain solver, -40 dB accuracy
- Hexahedral mesh, with 28-33 meshcells.
- Ports are modeled as 50 Ω discrete ports

A.3. Micromagnetic Simulation Parameter

Throughout this thesis, results of micromagnetic simulation are presented. The detailed simulation parameters are listed hereafter. When not stated explicitly below, the excitation of SWs is stated in the text.

Parameters which do not change are:

- Damping α = 0.005
- Saved simulation timestep $\Delta\tau$ = 6 ps
- No crystal anisotropies

Simulation Parameter Set A

Spatio-temporal resolved simulation for a plain film (here the simulation cell was set to be p/N = 12.5 nm) and ADLs (p = 180-800 nm). Hole diameters have been always keps constant at d = 120 nm.

- Saturation magnetization M_s = 780 kA/m
- Exchange constant: A = 1.3 × 10^9 J/m
- Film thickness t_s = 22 nm
- Simulation cells N = 64 × 4096 × 1
- Simulation cell size = p/N × p/N × 22 nm^3.
- Simulation duration: T = 10 ns.

Spin waves are excited by a short and spatially localized field pulse.

Simulation Parameter Set B

Temporal resolved simulation. This set of simulation parameters is used to simulate an MCWG structure with uniform excitation.

- Saturation magnetization M_s = 1330 kA/m (M_s has been adjusted with an additional surface anisotropy)
- Exchange constant: A = 2.75 × 10^9 J/m
- Film thickness t_s = 41 nm
- Simulation cells N = 1000 × 1000 × 1
- Simulation cell size = 12 × 12 × 41 nm^3
- Simulation duration: T = 8 ns.

Spin waves are excited by a spatially uniform, short field pulse.

Simulation Parameter Set C

Spatio-temporal resolved simulation for MCWG, MCB, and MCS with open boundary conditions. The size of the simulation cell is 15 μm × 15 μm × thickness (given in the respective chapter).

- Saturation magnetization M_s = 1330 kA/m
- Exchange constant: A = 2.75 $\times$ 10^9 J/m
- Film thickness t_s = 41 nm
- Simulation cells N = 768 × 768 × 1
- Simulation cell size = 19.5 × 19.5 × 41 nm^3.
- Simulation duration: T = 10 ns.

Spin waves are excited by a spatially localized sinusoidal driving field of given frequency.

Simulation Parameter Set D

Spatio-temporal resolved simulation for a stripe simulations.

- Saturation magnetization M_s = 1330 kA/m
- Exchange constant: A = 2.75 $\times$ 10^9 J/m
- Film thickness t_s = 41 nm
- Simulation cells N = 128 × 4096 × 1
- Simulation cell size = 2040 nm × 65.28 μm × 41 nm^3.
- Simulation duration: T = 10 ns.

Spin waves are excited by a short and spatially localized field pulse.

A.4. Micromagnetic Simulation Plots

Here we show the complete simulation cells for the time dependent simulations used in chapter 6.

Simulation Plots for MCWG

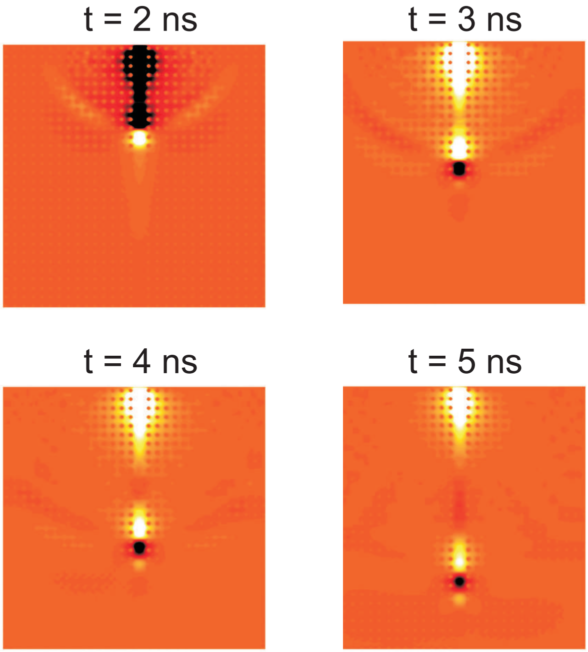

Figure A.1.: MCWG time dependent simulations.

Simulation Plots for MCB

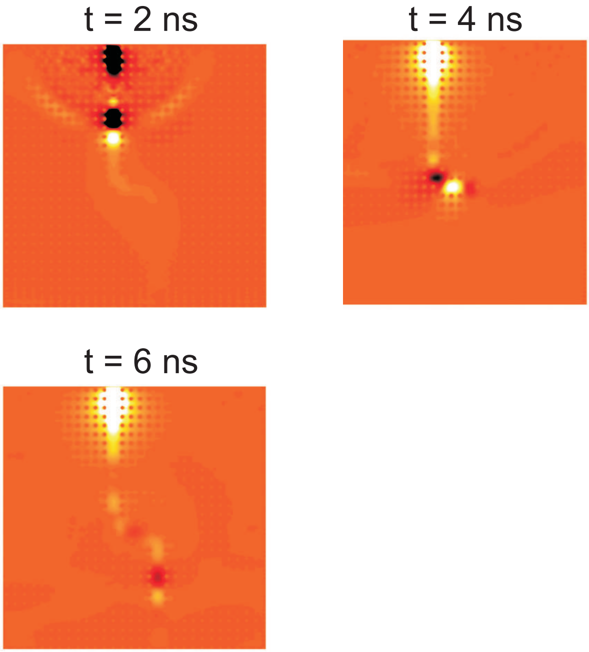

t = 2 ns

t = 4 ns

t = 6 ns

Figure A.2.: MCB time dependent simulations.

Simulation Plots for MCS

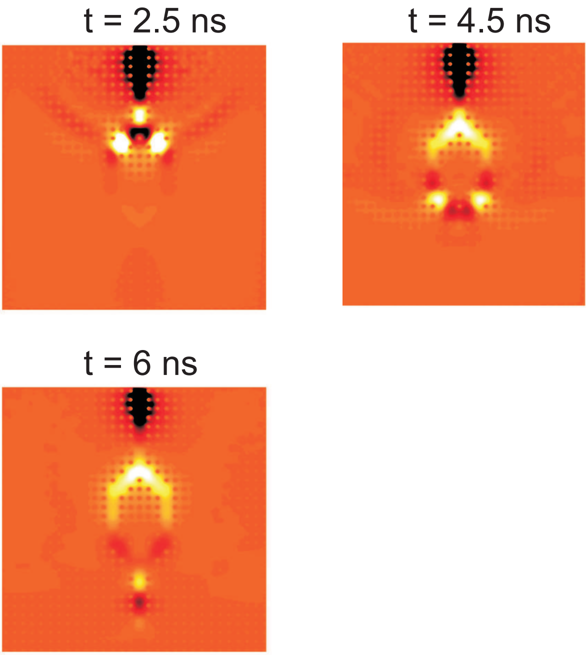

Figure A.3.: MCS time dependent simulations.

List of Figures

Bibliography

[Aha91] A. Aharoni: *Exchange resonance modes in a ferromagnetic sphere*, J. Appl. Phys. **69**, 7762 (1991).

[Aha97] A. Aharoni: *Effect of surface anisotropy on the exchange resonance modes*, J. Appl. Phys. **81**, 830 (1997).

[Aha06] A. Aharoni: *Introduction to the Theory of Ferromagnetism*, Oxford University Press, New York, 2006.

[Ari99] R. Arias und D. L. Mills: *Extrinsic contributions to the ferromagnetic resonance response of ultrathin films*, Phys. Rev. B **60**, 7395 (1999).

[Ari05] R. Arias, P. Chu und D. L. Mills: *Dipole exchange spin waves and microwave response of ferromagnetic spheres*, Phys. Rev. B **71**, 224410 (2005).

[Art57] J. O. Artman: *Microwave Resonance Relations in Anisotropic Single-Crystal Ferrites*, Phys. Rev. **105**, 62 (1957).

[Bai88] M. N. Baibich, J. M. Broto, A. Fert, F. Nguyen van Dau, F. Petroff, P. Eitenne, G. Creuzet, A. Friederich und J. Chazelas: *Giant Magnetoresistance of (001)Fe/(001)Cr Magnetic Superlattices*, Phys. Rev. Lett. **61**, 2472 (1988).

[Bai01] M. Bailleul, D. Olligs, C. Fermon und S. O. Demokritov: *Spin waves propagation and confinement in conducting films at the micrometer scale*, Europhys. Lett. **56**, 741 (2001).

[Bai03] M. Bailleul, D. Olligs und C. Fermon: *Micromagnetic Phase Transitions and Spin Wave Excitations in a Ferromagnetic Stripe*, Phys. Rev. Lett. **91**, 137204 (2003).

[Bak80] P. Bak und M. H. Jensen: *Theory of helical magnetic structures and phase transitions in MnSi and FeGe*, J. Phys. C: Solid State Phys. **13**, 881 (1980).

[Bao08] M. Bao, K. Wong, A. Khitun, J. Lee, Z. Hao, K. L. Wang, D. W. Lee und S. X. Wang: *Determining wave vector and material property from the phase-shift of spin-wave propagation*, EPL **84**, 27009 (2008).

[Bar77] V. G. Baryakhtar und B. A. Ivanov: *Phase diagram of a ferromagnetic plate in an external magnetic field*, Sov. Phys. JETP **45**, 789 (1977).

[Bau12] a. Bauer und C. Pfleiderer: *Magnetic phase diagram of MnSi inferred from magnetization and ac susceptibility*, Phys. Rev. B **85**, 214418 (2012).

[Bea09] J.-M. Beaujour, D. Ravelosona, I. Tudosa, E. E. Fullerton und a. D. Kent: *Ferromagnetic resonance linewidth in ultrathin films with perpendicular magnetic anisotropy*, Phys. Rev. B **80**, 180415 (2009).

[Bel10] M. Belesi, I. Rousochatzakis, H. C. Wu, H. Berger, I. V. Shvets, F. Mila und J. P. Ansermet: *Ferrimagnetism of the magnetoelectric compound Cu_2OSeO_3 probed by ^{77}Se NMR*, Phys. Rev. B **82**, 094422 (2010).

[Ber96] L. Berger: *Emission of spin waves by a magnetic multilayer traveresed by a current*, Phys. Rev. B **54**, 9353 (1996).

[Ber08] D. V. Berkov und N. L. Gorn: *Micromagus - software for micromagnetic simulations*, http://www.micromagus.de (2008).

[Bia03] E. de Biasi, C. Ramos und R. Zysler: *Size and anisotropy determination by ferromagnetic resonance in dispersed magnetic nanoparticle systems*, J. Magn. and Magn. Mater. **262**, 235 (2003).

[Bic50] L. R. Bickford: *Ferromagnetic Resonance Absorption in Magnetite Single Crystals*, Phys. Rev. **78**, 449 (1950).

[Bil07] C. Bilzer: *Microwave susceptibility of thin ferromagnetic films: metrology and insight into magnetization dynamics*, Dissertation, Faculte des sciences d'Orsay (2007).

[Bla00] C. T. Black: *Spin-Dependent Tunneling in Self-Assembled Cobalt-Nanocrystal Superlattices*, Science **290**, 1131 (2000).

[Blo30] F. Bloch: *Zur Theorie des Ferromagnetismus*, Zeitschrift für Physik **61** (1930).

[Blo92] P. J. H. Bloemen, W. J. M. deJonge und F. J. a. denBroeder: *Magnetic anisotropies in Co/Ni(111) multilayers*, J. Appl. Phys. **72**, 4840 (1992).

[Blu01] S. Blundell: *Magnetism in Condensed Matter*, Oxford University Press, Oxford, 2001.

[Bro63] W. F. Brown: *Micromagnetics*, Interscience Publishers, London, 1963.

[Cam98] C. Campbell: *Surface Acoustic Wave Devices for Mobile and Wireless Communications*, Academic, New York, 1998.

[Cha11] M. Charilaou, M. Winklhofer und A. U. Gehring: *Simulation of ferromagnetic resonance spectra of linear chains of magnetite nanocrystals*, J. Appl. Phys. **109**, 093903 (2011).

[Chi97] S. Chikazumi: *Physics of ferromagnetism*, Oxford University Press, Oxford, 1997.

[Cho06] S. Choi, K.-S. Lee und S.-K. Kim: *Spin-wave interference*, Appl. Phys. Lett. **89**, 062501 (2006).

[Cho07] S. Choi, K.-S. Lee, K. Y. Guslienko und S.-K. Kim: *Strong Radiation of Spin Waves by Core Reversal of a Magnetic Vortex and Their Wave Behaviors in Magnetic Nanowire Waveguides*, Phys. Rev. Lett. **98**, 087205 (2007).

[Cla11] P. Clausen, K. Vogt, H. Schultheiss, S. SchaÌĹfer, B. Obry, G. Wolf, P. Pirro, B. Leven und B. Hillebrands: *Mode conversion by symmetry breaking of propagating spin waves*, Appl. Phys. Lett. **99**, 162505 (2011).

[Cou04] G. Counil: *Spin wave contributions to the high-frequency magnetic response of thin films obtained with inductive methods*, J. Appl. Phys. **95**, 5646 (2004).

[Cov02] M. Covington, T. Crawford und G. Parker: *Time-Resolved Measurement of Propagating Spin Waves in Ferromagnetic Thin Films*, Phys. Rev. Lett. **89**, 237202 (2002).

[Daa92] G. H. O. Daalderop, P. J. Kelly und F. J. A. den Broeder: *Prediction and confirmation of perpendicular magnetic anisotropy in Co/Ni Multilayers,* Phys. Rev. Lett. **68**, 682 (1992).

[Dam61] R. W. Damon und J. R. Eshbach: *Magnetostatic modes of a ferromagnetic slab,* J. Appl. Phys. **19**, 308 (1961).

[Dem08] V. E. Demidov, S. O. Demokritov, K. Rott, P. Krzysteczko und G. Reiss: *Nano-optics with spin waves at microwave frequencies*, Appl. Phys. Lett. **92**, 232503 (2008).

[Dem09] V. E. Demidov, S. Urazhdin und S. O. Demokritov: *Control of spin-wave phase and wavelength by electric current on the microscopic scale*, App. Phys. Lett. **95**, 262509 (2009).

[Dem10] V. E. Demidov, S. Urazhdin und S. O. Demokritov: *Direct observation and mapping of spin waves emitted by spin-torque nano-oscillators,* Nature Mater. **9**, 984 (2010).

[Due12] G. Duerr: *Spin Waves in Nanochannels, Created by Individual and Periodic Bi-Component Ferromagnetic Devices,* Dissertation, Technische Universität München (2012).

[Far05] D. Farrell, Y. Cheng, R. W. McCallum, M. Sachan und S. A. Majetich: *Magnetic Interactions of Iron Nanoparticles in Arrays and Dilute Dispersions,* J. Phys. Chem. B **109**, 13409 (2005).

[Fio05] D. Fiorani (Hg.): *Surface effects in magnetic nanoparticles,* Springer, 2005.

[Gao10] H. Gao, W. Zhou und T. W. Odom: *Plasmonic Crystals: A Platform to Catalog Resonances from Ultraviolet to Near-Infrared Wavelengths in a Plasmonic Library,* Adv. Funct. Mater. **20**, 529 (2010).

[Gar03] D. Garanin und H. Kachkachi: *Surface Contribution to the Anisotropy of Magnetic Nanoparticles,* Phys. Rev. Lett. **90**, 065504 (2003).

[Gar13] M. Garst, J. Waizner und A. Rosch: private communication (2013).

[Gaz98] F. Gazeau, J. C. Bacri, F. Gendron, R. Perzynski, Y. L. Raikher, V. I. Stepanov und E. Dubois: *Magnetic resonance of ferrite nanoparticles : evidence of surface effects,* J. Magn. Magn. Mat. **186**, 175 (1998).

[Gie05] F. Giesen: *Magnetization dynamics of nanostructured ferromagnetic rings and rectangular elements,* Dissertation, Universität Hamburg, Fachberbeich Physik (2005).

[Gil55] T. Gilbert: *A lagrangian formulation of the gyromagnetic equation of the magnetization field*, Phys. Rev. **100** (1955).

[Gil10] K. Gilmore und M. D. Stiles: *Anisotropic damping of the magnetization dynamics in Ni, Co, and Fe,* Phys. Rev. B **81**, 1 (2010).

[Gri46] J. H. E. Griffiths: *Anomalous high-frequency resistance of ferromagnetic metals,* Nature **158**, 670 (1946).

[Gub07] G. Gubbiotti, M. Madami, S. Tacchi, G. Carlotti, a.O. Adeyeye, S. Goolaup, N. Singh und a.N. Slavin: *Spin wave eigenmodes of square permalloy dots studied by Brillouin light scattering,* J. Magn. Magn. Mater. **316**, 338 (2007).

[Gub12] G. Gubbiotti, G. Carlotti, S. Tacchi, M. Madami, T. Ono, T. Koyama, D. Chiba, F. Casoli und M. G. Pini: *Spin waves in perpendicularly magnetized Co/Ni(111) multilayers in the presence*, Phys. Rev. B **86**, 014401 (2012).

[Gue00] I. Guedes, N. J. Zaluzec, M. Grimsditch, V. Metlushko, P. Vavassori, B. Ilic, P. Neuzil und R. Kumar: *Magnetization of negative magnetic arrays: Elliptical holes on a square lattice*, Phys. Rev. B **62**, 11719 (2000).

[Gul03] Y. V. Gulyaev, S. A. Nikitov, L. V. Zhivotovskii, A. A. Klimov, P. Tailhades, L. Presmanes, C. Bonningue, C. Tsai, S. L. Vyotskii und Y. A. Filimonov: *Ferromagnetic Films with Magnon Bandgap Periodic Structures: Magnon Crystals*, JETP Lett. **77**, 567 (2003).

[Gur96] A. Gurevich und G. Melkov: *Magnetization oscillations and waves*, CRC Press, Boca Raton, 1996.

[Gus02] K. Guslienko, S. Demokritov, B. Hillebrands und a. Slavin: *Effective dipolar boundary conditions for dynamic magnetization in thin magnetic stripes*, Phys. Rev. B **66**, 132402 (2002).

[Gus07] N. Guskos: *FMR study of magnetic nanoparticles embedded in nonmagnetic matrix*, J. AMME **24**, 26 (2007).

[Hae13] M. Haertinger, C. H. Back, S.-H. Yang, S. S. P. Parkin und G. Woltersdorf: *Properties of Ni/Co multilayers as a function of the number of multilayer repetitions*, J. Phys. D: Appl. Phys. **46**, 175001 (2013).

[Hil02] B. Hillebrands und K. Ounadjela: *Spin Dynamics in Confined Magnetic Structures*, Springer, Berlin, 2002.

[Hu11] C.-L. Hu, R. Magaraggia, H.-Y. Yuan, C. S. Chang, M. Kostylev, D. Tripathy, A. O. Adeyeye und R. L. Stamps: *Field tunable localization of spin waves in antidot arrays*, Appl. Phys. Lett. **98**, 262508 (2011).

[Hub13] R. Huber, M. Krawczyk, T. Schwarze, H. Yu, G. Duerr, S. Albert und D. Grundler: *Reciprocal Damon-Eshbach-type spin wave excitation in a magnonic crystal due to tunable magnetic symmetry*, Appl. Phys. Lett. **102**, 012403 (2013).

[Hun12] S. Hunklinger: *Festkoerperphysik*, Oldenbourg, 2012.

[ITR09] ITRS: *International Technology Roadmap for Semiconductors*, 2009.

[Jam03] C. Jamois, R. Wehrspohn, L. Andreani, C. Hermann, O. Hess und U. Gösele: *Silicon-based two-dimensional photonic crystal waveguides*, Phot. Nano. Fund. Appl. **1**, 1 (2003).

[Joa08] J. D. Joannopoulos, S. G. Johnson, J. N. Winn und R. D. Meade: *Photonic Crystals, Molding the Flow of Light*, Princeton University Press, 2008.

[Jon10] F. Jonietz, S. Mühlbauer, C. Pfleiderer, A. Neubauer, W. Münzer, A. Bauer, T. Adams, R. Georgii, P. Böni, R. A. Duine, K. Everschor, M. Garst und A. Rosch: *Spin transfer torques in MnSi at ultralow current densities*, Science **330**, 1648 (2010).

[Kac06] H. Kachkachi und E. Bonet: *Surface-induced cubic anisotropy in nanomagnets*, Phys. Rev. B **73**, 224402 (2006).

[Kal86] B. A. Kalinikos und A. N. Slavin: *Theory of dipole-exchange spin wave spectrum for ferromagnetic films with mixed exchange boundary conditions*, J. Phys. C: Solid State Phys. **19**, 7013 (1986).

[Kal06] S. S. Kalarickal, P. Krivosik, M. Wu, C. E. Patton, M. L. Schneider, P. Kabos, T. J. Silva und J. P. Nibarger: *Ferromagnetic resonance linewidth in metallic thin films: Comparison of measurement methods*, J. Appl. Phys. **99**, 093909 (2006).

[Kar11] E. a. Karhu, S. Kahwaji, M. D. Robertson, H. Fritzsche, B. J. Kirby, C. F. Majkrzak und T. L. Monchesky: *Helical magnetic order in MnSi thin films*, Phys. Rev. B **84**, 060404 (2011).

[Kar12] E. a. Karhu, U. K. Röß ler, a. N. Bogdanov, S. Kahwaji, B. J. Kirby, H. Fritzsche, M. D. Robertson, C. F. Majkrzak und T. L. Monchesky: *Chiral modulations and reorientation effects in MnSi thin films*, Phys. Rev. B **85**, 094429 (2012).

[Kas08] O. Kasyutich, a. Sarua und W. Schwarzacher: *Bioengineered magnetic crystals*, J. Phys. D: Appl. Phys. **41**, 134022 (2008).

[Kat87] M. Kataoka: *Spin Waves in Systems with Long Period Helical Spin Density Waves Due to the Antisymmetric and Symmetric Exchange Interactions*, J. Phys. Soc. Jpn. **56**, 3635 (1987).

[Ken07] K. J. Kennewell, M. Kostylev und R. L. Stamps: *Calculation of spin wave mode response induced by a coplanar microwave line*, J. Appl. Phys. **101**, 09D107 (2007).

[Khi02] A. G. Khitun, R. Ostroumov und K. L. Wang: *Feasibility study of the spin wave quantum network*, Proc. SPIE **5023**, 449 (2002).

[Khi07] A. Khitun, D. E. Nikonov, M. Bao, K. Galatsis und K. L. Wang: *Feasibility study of logic circuits with a spin wave bus*, Nanotechnology **18**, 465202 (2007).

[Khi08a] a. Khitun, M. Bao, J.-Y. Lee, K. L. Wang, D. W. Lee, S. X. Wang und I. V. Roshchin: *Inductively Coupled Circuits with Spin Wave Bus for Information Processing*, J. Nanoelectron. Optoelectron. **3**, 24 (2008).

[Khi08b] A. Khitun, M. Bao, Y. Wu, J.-Y. Kim, A. Hong, A. Jacob, K. Galatsis und K. L. Wang: *Spin Wave Logic Circuit on Silicon Platform*, Information Technology: New Generations, Fifth International Conference , 1107 (2008).

[Khi10] A. Khitun, M. Bao und K. L. Wang: *Magnonic logic circuits*, J. Phys. D: Appl. Phys. **43**, 264005 (2010).

[Kim09] S.-K. Kim, K.-S. Lee und D.-S. Han: *A gigahertz-range spin-wave filter composed of width-modulated nanostrip magnonic-crystal waveguides*, Appl. Phys. Lett. **95**, 082507 (2009).

[Kis03] S. I. Kiselev, J. C. Sankey, I. N. Krivorotov, N. C. Emley, R. J. Schoelkopf, R. a. Buhrman und D. C. Ralph: *Microwave oscillations of a nanomagnet driven by a spin-polarized current*, Nature **425**, 380 (2003).

[Kit48] C. Kittel: *On the Theory of Ferromagnetic Resonance Absorption*, Phys. Rev. **73**, 155 (1948).

[Kit66] C. Kittel: *Introduction to Solid State Physics*, Wiley, New York, 1966.

[Kos08a] M. Kostylev, G. Gubbiotti, G. Carlotti, G. Socino, S. Tacchi, C. Wang, N. Singh, A. O. Adeyeye und R. L. Stamps: *Propagating volume and localized spin wave modes on a lattice of circular magnetic antidots*, J. Appl. Phys. **103**, 07C507 (2008).

[Kos08b] M. Kostylev, P. Schrader, R. L. Stamps, G. Gubbiotti, G. Carlotti, a. O. Adeyeye, S. Goolaup und N. Singh: *Partial frequency band gap in one-dimensional magnonic crystals*, Appl. Phys. Lett. **92**, 132504 (2008).

[Kos12] M. Kostylev, a. a. Stashkevich, Y. Roussigné, N. a. Grigoryeva, a. a. Mistonov, D. Menzel, N. a. Sapoletova, K. S. Napolskii, a. a. Eliseev, a. V. Lukashin, S. V. Grigoriev und S. N. Samarin: *Microwave properties of Ni-based ferromagnetic inverse opals*, Phys. Rev. B **86**, 184431 (2012).

[Kra08a] M. Krawczyk und H. Puszkarski: *Plane-wave theory of three-dimensional magnonic crystals*, Phys. Rev. B **77**, 1 (2008).

[Kra08b] M. Krawczyk, H. Puszkarski und S. P. Division: *Theory of spin-wave frequency gaps in 3d magnonic crystals. application to manganites*, arXiv:cond-mat , 1 (2008).

[Kru06] V. Kruglyak und R. Hicken: *Magnonics: Experiment to prove the concept*, J. Magn. Magn. Mater. **306**, 191 (2006).

[Kru10] V. V. Kruglyak, S. O. Demokritov und D. Grundler: *Magnonics*, J. Phys. D: Appl. Phys. **43**, 264001 (2010).

[Lan35] D. L. Landau und E. Lifshitz: *On the theory of the dispersion of magnetic permeability in ferromagnetic bodies*, Phys. Z. Sowjetunion **8** (1935).

[Lee08] K.-S. Lee und S.-K. Kim: *Conceptual design of spin wave logic gates based on a Mach Zehnder type spin wave interferometer for universal logic functions*, J. Appl. Phys. **104**, 053909 (2008).

[Len11] B. Lenk, H. Ulrichs, F. Garbs und M. Münzenberg: *The building blocks of magnonics*, Phys. Rep. **507**, 107 (2011).

[Li09] H. Li, M. Klem, K. Sebby, D. Singel, M. Young, T. Douglas und Y. Idzerda: *Determination of anisotropy constants of protein encapsulated iron oxide nanoparticles by electron magnetic resonance*, J. Mag. Mag. Mater. **321**, 175 (2009).

[Liu07] Y. Liu, S. Gliga, R. Hertel und C. M. Schneider: *Current-induced magnetic vortex core switching in a Permalloy nanodisk*, Appl. Phys. Lett. **91**, 112501 (2007).

[M0̈9] S. Mühlbauer, B. Binz, F. Jonietz, C. Pfleiderer, A. Rosch, A. Neubauer, R. Georgii und P. Böni: *Skyrmion lattice in a chiral magnet*, Science **323**, 915 (2009).

[Mac12] F. Macià, P. Warnicke, D. Bedau, M.-Y. Im, P. Fischer, D. Arena und a.D. Kent: *Perpendicular magnetic anisotropy in ultrathin multilayer films studied with ferromagnetic resonance and magnetic x-ray microspectroscopy*, J. Magn. and Magn. Mater. **324**, 3629 (2012).

[Mad11] M. Madami, S. Bonetti, G. Consolo, S. Tacchi, G. Carlotti, G. Gubbiotti, F. B. Mancoff, M. a. Yar und J. Akerman: *Direct observation of a propagating spin wave induced by spin-transfer torque.*, Nat. Nanotechnol. **6**, 635 (2011).

[Mal03] J. C. Mallinson: *On damped gyromagnetic precession*, IEEE Trans. Magn. **23**, 2003 (2003).

[Mam12] S. Mamica, M. Krawczyk, M. L. Sokolovskyy und J. Romero-Vivas: *Large magnonic band gaps and spectra evolution in three-dimensional magnonic crystals based on magnetoferritin nanoparticles*, Phys. Rev. B **86**, 144402 (2012).

[Mar07] O. N. Martyanov, V. F. Yudanov, R. N. Lee, S. A. Nepijko, H. J. Elmers, R. Hertel, C. M. Schneider und G. Schönhense: *Ferromagnetic resonance study of thin film antidot arrays: Experiment and micromagnetic simulations*, Phys. Rev. B **75**, 174429 (2007).

[Mar10] D. Marko, K. Lenz, T. Strache, R. Kaltofen und J. Fassbender: *Measuring the Saturation Magnetization in Samples With Unknown Magnetic Volume*, IEEE Trans. Magn. **46**, 1711 (2010).

[McP05] S. McPhail, C. M. Gürtler, J. M. Shilton, N. J. Curson und J. A. C. Bland: *Coupling of spin-wave modes in extended ferromagnetic thin film antidot arrays*, Phys. Rev. B **72**, 094414 (2005).

[Mel01] G. Melkov, Y. Kobljanskyj, a. Serga, V. Tiberkevich und a. Slavin: *Reversal of Momentum Relaxation*, Phys. Rev. Lett. **86**, 4918 (2001).

[Mer00] D. Mercier, J.-C. S. Lévy, G. Viau, F. Fiévet-Vincent, F. Fiévet, P. Toneguzzo und O. Acher: *Magnetic resonance in spherical Co-Ni and Fe-Co-Ni particles*, Phys. Rev. B **62**, 532 (2000).

[Miz11] S. Mizukami, X. Zhang, T. Kubota, H. Naganuma, M. Oogane, Y. Ando und T. Miyazaki: *Gilbert Damping in Ni/Co Multilayer Films Exhibiting Large Perpendicular Anisotropy*, Appl. Phys. Express **4**, 013005 (2011).

[Moc12] M. Mochizuki: *Spin-Wave Modes and Their Intense Excitation Effects in Skyrmion Crystals*, Phys. Rev. Lett. **108**, 1 (2012).

[Moh12] M. S. Mohseni: *Spin Valves and Spin-Torque Oscillators with Perpendicular Magnetic Anisotropy*, Dissertation, KTH Royal Institute of Technology (2012).

[Mux00] A. Muxworthy und E. McClelland: *Review of the low-temperature magnetic properties of magnetite from a rock magnetic perspective*, Geophys. J. Inc. **140**, 101 (2000).

[Nak80] O. Nakanishi, A. Yanase, A. Hasegawa und M. Kataoka: *The origin of the helical spin density wave in MnSi*, Solid State Commun. **35**, 995 (1980).

[Nal13] V. Naletov, G. Loubens, S. Borlenghi und O. Klein: *Nano-Contact Spin-Torque Oscillators as Magnonic Building Blocks*, Bd. 125 von *Topics in Applied Physics*, Springer Berlin Heidelberg, 2013.

[Neu06] I. Neudecker, M. Kläui, K. Perzlmaier, D. Backes, L. Heyderman, C. Vaz, J. Bland, U. Rüdiger und C. Back: *Spatially Resolved Dynamic Eigenmode Spectrum of Co Rings*, Phys. Rev. Lett. **96**, 057207 (2006).

[Neu08] S. Neusser, B. Botters, M. Becherer, D. Schmitt-Landsiedel und D. Grundler: *Spin-wave localization between nearest and next-nearest neighboring holes in an antidot lattice*, Appl. Phys. Lett. **93**, 122501 (2008).

[Neu09a] A. Neubauer, C. Pfleiderer, B. Binz, A. Rosch, R. Ritz, P. Niklowitz und P. Böni: *Topological Hall Effect in the A Phase of MnSi*, Phys. Rev. Lett. **102**, 1 (2009).

[Neu09b] S. Neusser und D. Grundler: *Magnonics: Spin Waves on the Nanoscale*, Adv. Mater. **21**, 2927 (2009).

[Neu10] S. Neusser, G. Duerr, H. Bauer, S. Tacchi, M. Madami, G. Woltersdorf, G. Gubbiotti, C. Back und D. Grundler: *Anisotropic Propagation and Damping of Spin Waves in a Nanopatterned Antidot Lattice*, Phys. Rev. Lett. **105**, 1 (2010).

[Neu11a] a. Neubauer, J. Boeuf, A. Bauer, B. Russ, H. V. Löhneysen und C. Pfleiderer: *Ultra-high vacuum compatible image furnace*, Rev. Sci. Instrum. **82**, 013902 (2011).

[Neu11b] S. Neusser: *Spin Waves in Antidot Lattices : From Quantization to Magnonic Crystals*, Dissertation, Technische Universität München (2011).

[Neu11c] S. Neusser, H. Bauer, G. Duerr, R. Huber, S. Mamica, G. Woltersdorf, M. Krawczyk, C. Back und D. Grundler: *Tunable metamaterial response of a* $Ni_{80}Fe_{20}$ *antidot lattice for spin waves*, Phys. Rev. B **84**, 1 (2011).

[Neu11d] S. Neusser, G. Duerr, S. Tacchi, M. Madami, M. Sokolovskyy, G. Gubbiotti, M. Krawczyk und D. Grundler: *Magnonic minibands in antidot lattices with large spin-wave propagation velocities*, Phys. Rev. B **84**, 1 (2011).

[Oku12] M. Okuda, J.-C. Eloi, A. Sarua, S. E. Ward Jones und W. Schwarzacher: *Energy barrier distribution for dispersed mixed oxide magnetic nanoparticles*, J. Appl. Phys. **111**, 07B519 (2012).

[Oku13] M. Okuda, J. C. Eloi, S. E. Ward Jones, P. J. Heard, A. Sarua, V. V. Kruglyak und W. Schwarzacher: *Micromachined freestanding nanoparticle arrays from protein crystals using chemical fixation*, Small **submitted** (2013).

[Ono12] Y. Onose, Y. Okamura, S. Seki, S. Ishiwata und Y. Tokura: *Observation of Magnetic Excitations of Skyrmion Crystal in a Helimagnetic Insulator Cu2OSeO3*, Phys. Rev. Lett. **109**, 1 (2012).

[Pec05] M. J. Pechan, C. Yu, R. L. Compton, J. P. Park und P. A. Crowell: *Direct measurement of spatially localized ferromagnetic-resonance modes in an antidot lattice (invited)*, J. Appl. Phys. **97**, 10J903 (2005).

[Per05] R. Perzynski und Y. L. Raikher: *Effect of surface anisotropy on the magnetic resonance properties of nanosize ferroparticles*, Springer US, 2005.

[Pig12] B. Pigeau, C. Hahn, G. de Loubens, V. V. Naletov, O. Klein, K. Mitsuzuka, D. Lacour, M. Hehn, S. Andrieu und F. Montaigne: *Measurement of the Dynamical Dipolar Coupling in a Pair of Magnetic Nanodisks Using a Ferromagnetic Resonance Force Microscope*, Phys. Rev. Lett. **109**, 247602 (2012).

[Pil06] M. P. Pileni: *Self-organization of inorganic nanocrystals*, J. Phys.: Condens. Matter **18**, S67 (2006).

[Sar43] R. I. Sarbacher und W. A. Edson: *Hyper and Ultrahigh Frequency Engineering*, Wiley, New York, 1943.

[Sch12a] T. Schulz, R. Ritz, A. Bauer, M. Halder, M. Wagner, C. Franz, C. Pfleiderer, K. Everschor, M. Garst und A. Rosch: *Emergent electrodynamics of skyrmions in a chiral magnet*, Nature Phys. **8**, 301 (2012).

[Sch12b] T. Schwarze, R. Huber, G. Duerr und D. Grundler: *Complete band gaps for magnetostatic forward volume waves in a two-dimensional magnonic crystal*, Phys. Rev. B **85**, 134448 (2012).

[Sch13] T. Schwarze und D. Grundler: *Magnonic crystal wave guide with large spin-wave propagation velocity in CoFeB*, Appl. Phys. Lett. **102**, 222412 (2013).

[Shi99a] V. P. Shilov, J.-C. Bacri, F. Gazeau, F. Gendron, R. Perzynski und Y. L. Raikher: *Ferromagnetic resonance in ferrite nanoparticles with uniaxial surface anisotropy*, J. Appl. Phys. **85**, 6642 (1999).

[Shi99b] V. P. Shilov, Y. L. Raikher, J.-C. Bacri, F. Gazeau und R. Perzynski: *Effect of unidirectional anisotropy on the ferromagnetic resonance in ferrite nanoparticles*, Phys. Rev. B **60**, 11902 (1999).

[Sil99] T. J. Silva, C. S. Lee, T. M. Crawford und C. T. Rogers: *Inductive measurement of ultrafast magnetization dynamics in thin-film Permalloy*, J. Appl. Phys. **85**, 7849 (1999).

[Sko08] R. Skomski: *Simple models of magnetism*, Oxford University Press, Oxford, 2008.

[Spa03] N. Spalding: *Magnetic Materials; Fundamentals and device applications*, Cambridge University Press, Cambridge, 2003.

[Sta09] D. D. Stancil und A. Prabhakar: *Spin Waves: Theory and Applications*, Springer, 2009.

[Sto06] J. Stoehr und H. C. Siegmann: *Magnetism - From Fundamentals to Nanoscale Dynamics*, Springer, Berlin, 2006.

[Sur92] C. Surig und K. A. Hempel: *Microwave absorption in single-domain particles involving first- and second-order uniaxial magnetic anisotropy constant*, J. Magn. Magn. Mater. **117**, 441 (1992).

[Tac10a] S. Tacchi, M. Madami, G. Gubbiotti, G. Carlotti, A. Adeyeye, S. Neusser, B. Botters und D. Grundler: *Magnetic Normal Modes in Squared Antidot Array With Circular Holes: A Combined Brillouin Light Scattering and Broadband Ferromagnetic Resonance Study*, IEEE Trans. Mag. **46**, 172 (2010).

[Tac10b] S. Tacchi, M. Madami, G. Gubbiotti, G. Carlotti, A. O. Adeyeye, S. Neusser, B. Botters und D. Grundler: *Angular Dependence of Magnetic Normal Modes in NiFe Antidot Lattices With Different Lattice Symmetry*, IEEE Trans. Mag. **46**, 1440 (2010).

[Top10] J. Topp, D. Heitmann, M. P. Kostylev und D. Grundler: *Making a Reconfigurable Artificial Crystal by Ordering Bistable Magnetic Nanowires*, Phys. Rev. Lett. **104**, 0 (2010).

[Tse09] D. H. Y. Tse, S. J. Steinmuller, T. Trypiniotis, D. Anderson, G. A. C. Jones, J. A. C. Bland und C. H. W. Barnes: *Static and dynamic magnetic properties of $Ni_{80}Fe_{20}$ square antidot arrays*, Phys. Rev. B **79**, 054426 (2009).

[Tso00] M. Tsoi, A. G. M. Jansen, J. Bass, W. Chiang, V. Tsoi und P. Wyder: *Generation and detection of phase-coherent current-driven magnons in magnetic multilayers*, Nature **406**, 4 (2000).

[Ulr10] H. Ulrichs, B. Lenk und M. Munzenberg: *Magnonic spin-wave modes in CoFeB antidot lattices*, Appl. Phys. Lett. **97**, 092506 (2010).

[Vit85] C. Vittoria, P. Lubitz, P. Hansen und W. Tolksdorf: *FMR linewidth measurements in bismuth-substituted YIG*, J. Appl. Phys. **57**, 3699 (1985).

[Vla08] V. Vlaminck und M. Bailleul: *Current-Induced Spin-Wave Doppler Shift*, Science **322**, 410 (2008).

[Vla10] V. Vlaminck und M. Bailleul: *Spin-wave transduction at the submicrometer scale: Experiment and modeling*, Phys. Rev. B **81**, 1 (2010).

[Vog12] K. Vogt, H. Schultheiss, S. Jain, J. E. Pearson, A. Hoffmann, S. D. Bader und B. Hillebrands: *Spin waves turning a corner*, Appl. Phys. Lett. **101**, 042410 (2012).

[Wai13] J. Waizner: *Dynamics in Chiral Magnets: Magnetic and Electric Excitations of Helices and Skyrmions*, Diplomarbeit, University of Cologne (2013).

[Wal57] L. Walker: *Magnetostatic Modes in Ferromagnetic Resonance*, Phys. Rev. **105**, 390 (1957).

[Wei08] T. Weiland, M. Timm und I. Munteanu: *A practical guide to 3D simulation*, IEEE Microwave Mag. **9**, 62 (2008).

[Yan07] R. Yanes, O. Chubykalo-Fesenko, H. Kachkachi, D. A. Garanin, R. Evans und R. W. Chantrell: *Effective anisotropies and energy barriers of magnetic nanoparticles with Néel surface anisotropy*, Phys. Rev. B **76**, 064416 (2007).

[Yan09] R. Yanes und O. Chubykalo-Fesenko: *Modelling of the influence of the Neel surface anisotropy on the enhancement of the magnetic anisotropy in Co nanoparticle*, J. Phys. D: Appl. Phys. **42**, 055013 (2009).

[Yu03] C. Yu, M. J. Pechan und G. J. Mankey: *Dipolar induced, spatially localized resonance in magnetic antidot arrays*, Appl. Phys. Lett. **83**, 3948 (2003).

[Yu04] C. Yu, M. J. Pechan, W. A. Burgei und G. J. Mankey: *Lateral standing spin waves in permalloy antidot arrays*, J. Appl. Phys. **95**, 6648 (2004).

[Yu07] M. Yu, L. Malkinski, L. Spinu, W. Zhou und S. Whittenburg: *Size dependence of static and dynamic magnetic properties in nanoscale square Permalloy antidot arrays*, J. Appl. Phys. **101**, 09F501 (2007).

[Yu10] J.-K. Yu, S. Mitrovic, D. Tham, J. Varghese und J. R. Heath: *Reduction of thermal conductivity in phononic nanomesh structures*, Nat. Nanotechnol. **5**, 718 (2010).

[Yu11] X. Z. Yu, N. Kanazawa, Y. Onose, K. Kimoto, W. Z. Zhang, S. Ishiwata, Y. Matsui und Y. Tokura: *Near room-temperature formation of a skyrmion crystal in thin-films of the helimagnet FeGe*, Nature Mater. **10**, 1 (2011).

[Yu12] H. Yu, R. Huber, T. Schwarze, F. Brandl, T. Rapp, P. Berberich, G. Duerr und D. Grundler: *High propagating velocity of spin waves and temperature dependent damping in a CoFeB thin film*, Appl. Phys. Lett. **100**, 262412 (2012).

[Ziv12] R. Zivieri, S. Tacchi, F. Montoncello, L. Giovannini, F. Nizzoli, M. Madami, G. Gubbiotti, G. Carlotti, S. Neusser, G. Duerr und D. Grundler: *Bragg diffraction of spin waves from a two-dimensional antidot lattice*, Phys. Rev. B **85**, 012403 (2012).

Publications

- R. Huber, T. Schwarze, and D. Grundler: Nanostripe of subwavelength width as a switchable semitransparent mirror for spin waves in a magnonic crystal, Phys. Rev. B (Rapid Commun.), **88**, 100405(R) (2013)
- T. Schwarze and D. Grundler: Magnonic crystal wave guide with large spin-wave propagation velocity in CoFeB, Appl. Phys. Lett. **102**, 222412 (2013)
- H. Yu, G. Duerr, R. Huber, M. Bahr, T. Schwarze, F. Brandl, and D. Grundler: Omnidirectional all-electrical emission of spin waves with giantly enhanced amplitude using nanostructured magnonic grating couplers, submitted (2013)
- R. Huber, M. Krawczyk, T. Schwarze, H. Yu, G. Duerr, S. Albert, and D. Grundler: Reciprocal Damon-Eshbach-type spin wave excitation in a magnonic crystal due to tunable magnetic symmetry, Appl. Phys. Lett. **102**, 012403 (2013)
- H. Yu, R. Huber, T. Schwarze, F. Brandl, T. Rapp, P. Berberich, G. Duerr, and D. Grundler: High propagating velocity of spin waves and temperature dependent damping in a CoFeB thin film, Appl. Phys. Lett. **100**, 262412 (2012)
- T. Schwarze, R. Huber, G. Duerr, and D. Grundler: Complete band gaps for magnetostatic forward volume waves in a two-dimensional magnonic crystal, Phys. Rev. B **85**, 134448 (2012)
- V. V. Kruglyak, M. Dvornik, R. V. Mikhaylovskiy, O. Dmytriiev, G. Gubbiotti, S. Tacchi, M. Madami, G. Carlotti, F. Montoncello, L. Giovannini, R. Zivieri, J. W. Klos, M. L. Sokolovskyy, S. Mamica, M. Krawczyk, M. Okuda, J.-C. Eloi, S. Ward Jones, W. Schwarzacher, T. Schwarze, F. Brandl, D. Grundler, D. V. Berkov, E. Semenova, and N. Gorn: Magnonic metamaterials, in book Metamaterial, InTech, ISBN 978-953-51-0591-6 (2012)
- T. Schwarze, R. Huber, G. Duerr, F. Brandl, S. Neusser, K. Thurner, and D. Grundler: Microwave Antennas for Broadband Spectroscopy on Magnonic Metamaterials, Metamaterials ’2011: The Fifth International Congress on Advanced Electromagnetic Materials in Microwaves and Optics, Metamorphose-VI, ISBN 978-952-67611-0-7, p. 576 (2011)
- T. Schwarze, M. Okuda, R. Huber, J.-C. Eloi, F. Brandl, L. Dreher, M.S. Brandt, D. Grundler, and W. Schwarzacher: Fabrication and characterization of crystallized magnetoferritin as an artificial magnetic metamaterial,

Metamaterials ’2011: The Fifth International Congress on Advanced Electromagnetic Materials in Microwaves and Optics, Metamorphose-VI, ISBN 978-952-67611-0-7, p. 125 (2011)

- R. Huber, T. Schwarze, P. Berberich, T. Rapp, and D. Grundler: Atomic layer deposition for the fabrication of magnonic metamaterials, Metamaterials ’2011: The Fifth International Congress on Advanced Electromagnetic Materials in Microwaves and Optics, Metamorphose-VI, ISBN 978-952-67611-0-7, p. 588 (2011)
- T. Schwarze: Magnetic imaging with transmission x-ray microscopy: sample preparation technique for epitaxially grown magnetic materials, VDM Verlag, ISBN: 3639362519 (2011)

Acknowledgements

I would like to express my deepest gratitude to all the people who contributed to this work. In particular:

- Prof. Dr. Martin Zacharias for supervision of the PhD examination, Prof. Dr. Dirk Grundler for being the first examiner and Prof. Christian Pfleiderer for being the second examiner.
- Prof. Dr. Dirk Grundler for giving me the chance to work at E10, for many fruitful discussions about all aspects of my work and for giving me great opportunities to evolve into a good scientist.
- Ioannis Stasinopoulos for experimental support and for PMA measurements.
- Rupert Huber, Georg Duerr, Sebastian Neusser, Florian Brandl, Florian Heimbach, and Dr. Haiming Yu for fruitful collaboration at E10.
- Prof. Christian Pfleiderer and Andreas Bauer at E21 for fabrication and supply of chiral helimagnetic materials as well as fruitful discussions and help on interpretation of the experimental results.
- Prof. Dr. Achim Rosch, Dr. Markus Garst and Johannes Waizner from the University of Cologne for collaboration on chiral helimagnets and for theoratical support on the matter.
- Prof. Dr. Walther Schwarzacher and Dr. Mitsuhiro Okuda from the University of Bristol for fabrication and supply of magnetoferritin crystals and fruitful discussions.
- Dr. Maciej Krawczyk from AMU Poznan for calculations and numerous interesting discussions on the interpretation of excitations in magnetoferritin crystals.
- Prof. Johan Åkerman at the University of Gothenburg for providing perpendicular magnetic anisotropy samples and discussions on measurement results.
- Thomas Rapp, Thomas Neukel, and Paul Berberich for frequent and immediate technical support.
- Claudine Voelcker for organizational support.

- All coworkers at E10 for collaboration and great atmosphere: Stephan Albert, Matthias Brasse, Stefanos Chalkidis, Ayman Ibrahim, Susanne Goercke, Tobias Stueckler, Amadeus Mlynarski, Benedikt Rupprecht, Stephan Lichtenauer, Johannes Seitz, and Dr. Marc Wilde.
- Last but not least, I would like to thank my friends, family, and my wife Louise, for their support and encouragement.

The research leading to these results has received funding from the European Community's Seventh Framework Programme (FP7/2007-2013) under Grant No. 228673 (MAGNONICS), Grant No. 247556 (NoWaPhen), and the German Excellence Cluster Nanosystems Initiative Munich (NIM), and by the DFG via SFB/TRR 80 ”From electronic correlations to functionality', and CST Corporation in Darmstadt, Germany for the software package $MicrowaveStudio$. The support is gratefully acknowledged.